# Seismic characterization of geothermal reservoirs by application of the common-reflection-surface method and attribute analysis


Pussak Marcin

Institute of Earth and Environmental Science

Potsdam University

A thesis submitted for the degree of

*PhilosophiæDoctor (PhD)*

Potsdam, Juli 2014

Published online at the
Institutional Repository of the University of Potsdam:
URN urn:nbn:de:kobv:517-opus4-77565
http://nbn-resolving.de/urn:nbn:de:kobv:517-opus4-77565

# Abstract

An important contribution of geosciences to the renewable energy production portfolio is the exploration and utilization of geothermal resources. For the development of a geothermal project at great depths a detailed geological and geophysical exploration program is required in the first phase. With the help of active seismic methods high-resolution images of the geothermal reservoir can be delivered. This allows potential transport routes for fluids to be identified as well as regions with high potential of heat extraction to be mapped, which indicates favorable conditions for geothermal exploitation.

The presented work investigates the extent to which an improved characterization of geothermal reservoirs can be achieved with the new methods of seismic data processing. The summations of traces (stacking) is a crucial step in the processing of seismic reflection data. The common-reflection-surface (CRS) stacking method can be applied as an alternative for the conventional normal moveout (NMO) or the dip moveout (DMO) stack. The advantages of the CRS stack beside an automatic determination of stacking operator parameters include an adequate imaging of arbitrarily curved geological boundaries, and a significant increase in signal-to-noise (S/N) ratio by stacking far more traces than used in a conventional stack.

A major innovation I have shown in this work is that the quality of signal attributes that characterize the seismic images can be significantly improved by this modified type of stacking in particular. Imporoved attribute analysis facilitates the interpretation of seismic images and plays a significant role in the characterization of reservoirs. Variations of lithological and petrophysical properties are reflected by fluctuations of specific signal attributes (eg. frequency or amplitude characteristics). Its further interpretation can provide quality assessment of the geothermal reservoir with respect to the capacity of fluids within a hydrological system that can be extracted and utilized.

The proposed methodological approach is demonstrated on the basis on two case studies. In the first example, I analyzed a series of 2D seismic profile sections through the Alberta sedimentary basin on the eastern edge of the Canadian Rocky Mountains. In the second application, a 3D seismic volume is characterized in the surroundings of a geothermal borehole, located in the central part of the Polish basin. Both sites were investigated with the modified and improved stacking attribute analyses. The results provide recommendations for the planning of future geothermal plants in both study areas.

# Contents

# List of Figures

## LIST OF FIGURES

# List of Tables

# 1

# Introduction

The main message of this thesis concentrates on the methods that can significantly improve imaging of seismic reflection data acquired from sedimentary environments that may host hydrocarbon or geothermal resources. Since many years, reflection seismics is the most valuable technique for revealing the geological information contained in the subsurface. With the use of non-destructive surface measurements it provides the details of the Earths interior allowing geologists to make comprehensive and rational choices concerning exploration and exploitation.

The geothermal applications which make use of earths heat, can be applied almost anywhere. However, under certain circumstances related to physical properties, even less productive reservoirs can be accessed with economic use. The most important parameters describing the geothermal reservoir are based on rock physical properties that host geothermal resources. Thus, the conceptual model of a geothermal system and its characteristics can be determined by different geophysical methods whose application strongly depends on the local geological conditions. It is worth to note that the drilling operations are the most expensive part of geothermal projects, therefore special attention is necessary to minimize the risk by providing the most reliable model of the subsurface.

The conceptual model of a geothermal reservoir can be acquired by the integration of geophysical methods that have capabilities to determine reservoir parameters influencing further exploitation. Such a model is most valuable when fully described by geostructural elements with stress information and characterized by porosity and permeability of the rocks formations. So far, the most successful geothermal projects were preceded by the application of electrical, seismic and potential field methods or

their combination. Although electrical methods, and magnetotellurics especially, were mostly used in conventional exploration programs, since about a dozen years the seismic imaging method has taken the leading role in geothermal projects.

In order to ensure the effectiveness of geothermal productivity a complete geostructural identification of the prospective horizons and nearby structures is required. Such information is provided by seismic investigations and is usually based on reprocessing of old data and new 2D or more often 3D surveys, depending on the budget. In contrast to 2D lines, 3D volumes allow for the identification and mapping of structural features such as fault zones and seismic compartments within target horizons. The latter can be used in combination with other data from geology and borehole analysis to constrain numerical simulations of geothermal production. Additionally, they may help to discover new possible targets for geothermal exploration i.e fractured zones of high permeability or sinkholes.

In simply terms, seismic measurements are focused to record the signal generated by the source, that propagates in the form of elastic waves. Differences in elastic properties of the adjacent geological formations cause that the wave will be partially transmitted and reflected. The reflected events are then recorded in the form of seismograms by receivers arranged in special layouts at the surface.

In the next step, the acquired data are processed in sophisticated processing routine flows in order to increase the signal to noise ratio (S/N) and thus transform the recorded events into high quality images of the subsurface. The recorded signals travel from the source to the receivers illuminating structures encountered along the way and significantly increasing the amount of recorded data. This so-called redundant information is later used in the summation process the result of which is a stacked section. Summation of traces that illuminate the same reflection point enhance the amplitude of the recorded signal while the unwanted information is attenuated. This procedure allows to obtain a section where location of both source and receivers match each-other producing a zero-offset (ZO) section.

In general, a successful stacking operation demands an accurate velocity model. The common midpoint (CMP) stacking method was originally developed for horizontally layered media (Mayne, 1962). Thus, providing an accurate solution also for dipping reflectors makes the stacking procedure challenging due to reflectionpoint dispersal. Later on Yilmaz & Clearbout (1980) proposed a method called dip moveout (DMO) to overcome this effect. Utilizing this solution, traces that are spread around a common

reflection point (CRP) create a more accurate ZO section than the conventional CMP stack.

The significant increase of computing power in the last decades has allowed for development and application to a real dataset of modern methods that overcome the problem of dipping reflector. Two methods appeared almost at the same time, namely the Common Reflection Surface (CRS) stack (Jäger *et al.*, 2001; Mann, 2002; Mann *et al.*, 1999) and Multifocusing (Berkovitch *et al.*, 2008; Landa *et al.*, 1999, 2010). Both methods have raised the quality of the stacked section to a much higher level. The methods aim at defining the reflector by an accurate determination of its position, dip and curvature by the selection of parameters in two measurement planes (offset and CMP). An additional contribution of a large amount of traces improves the stacking results and drastically increases the S/N ratio, and thus the approximation of travel–times is more accurate than the NMO/DMO stack. It is worth to note that the CRS method has been developed for both 2D and 3D media as a fully automatic process and only requires a limited user assistance. Moreover the stack can be obtained without explicit knowledge of the velocity model (Müller, 1999).

As can be expected, dynamic development of the CRS method has created exceptional accompanying work. For example, the kinematic attributes obtained during traveltime approximation were used to determine laterally inhomogeneous 2D/3D velocity models Duveneck (2004). The velocity models obtained from Normal Incidence Point – NIP-wave tomography can be applied for further processing, i.e. depth imaging (conversion of the data from time to depth domain) as has been shown by Dümmong *et al.* (2007). he partial CRS stacking method, proposed by Baykulov *et al.* (2009) allows to obtain a regular and uniform stacked seismic section/volume and additionally can be used to fill in the gaps between traces within a sparse dataset. Besides the data infill and overall S/N improvement, the partial CRS stack assumes amplitude preservation that allows the method to be widely applied (Baykulov & Gajewski, 2009).

A method to derive the migration velocities based on the CRS kinematic attributes was proposed by Mann (2002). It is based on the assumption that the diffraction response can be obtained by the CRS operator, thus mapping the diffraction apex. Recent developments of the CRS technique focused on structural imaging associated with fractured or pinch-out structures with thickness of less than half a wavelength. Dell (2012) made use of the CRS method to separate diffraction from primary reflection events in the time domain by using the CRS attributes to attenuate the reflection events

in the poststack domain while making a simultaneously summing the diffraction events in the way of partial CRS stacking.

Seismic attributes analysis is another important step in reservoir engineering as well as in the development of a geothermal project and can be used for quantitative and qualitative interpretation. Information extracted from seismic data allows to highlight the particularly useful features at different scales and resolution. In thesis, I applied the seismic attributes to reflection data obtained from the CRS stack method in order to perform a lithological interpretation, as the attributes can be qualitatively correlated to borehole data.

In order to check whether the combination of the CRS stack method with seismic attributes can be used as an extended tool in geothermal exploration, I compiled the structure of the thesis as follows:

In chapter 1, I describe the thesis content and the general overview of its structure. The basic ideas of a geothermal experiment and definitions with respect to the exploration techniques are provided.

A brief description of the geophysical methods that are particularly useful in geothermal exploration is given in chapter 2. However, depending on the target and the specific geothermal project, the application of a single or multiple method approach may be required. Three main groups of geophysical methods, namely electrical, seismic and potential field provide considerable information that is essential for the construction of a hydrogeological model of a geothermal reservoir.

Chapter 3, summarizes the state of the art in the seismic data processing emphasizing the roles of conventional and newly developed methods. It describes CMP and CRS stack methods used in time imaging. In particular, it provides the information concerning the CRS stack method that is required to significantly improve the S/N ratio of the prestack dataset obtained from a reflection seismic experiment.

In chapter 4, I show the results of reprocessing 2D reflection seismic data obtained within the frame of the Lithoprobe project (Eaton *et al.*, 1995) aimed at crustal identification in the Western Canadian Sedimentary Basin. While in the first part the conventional the CMP stack was used to derive the geological image of the subsurface, the second part shows the improvement acquired by the use of the CRS method for the

same dataset. In the last sub-section, the trace attributes were used to verify the improvements in the CRS stack and provide additional lithological information contained within the selected horizons.

Chapter 5 describes a low-fold 3D seismic reflection survey performed within the $6^{th}$ EU Framework Programme at the Skierniewice site located in the Polish basin. The conventional CMP and CRS stacks were acquired to demonstrate the significant improvements of the CRS method in structural imaging of the fault system that was essential for geothermal exploration of the investigated area. Moreover, the trace attributes performed along the target horizon on both stacks were used to indicate a prospective zone for a drilling location or direct exploitation.

Chapter 6 contains a summary of the results obtained from the two previous chapters supported by the cluster analysis that can provide more specific characteristics of the reflected horizons. It was used in large-scale identification of lithological variations along 2D cross-sections from the Alberta basin and in a 3D horizon analysis performed in the Polish basin. In addition, it gives an outlook for prospective fields of work that can be identified with the combination of the CRS stack method and the trace attribute analysis.

# 2

# Geophysical methods in geothermal exploration

The main aim of geothermal exploration is to detect and provide detailed information of highly permeable reservoirs which contain steam or hot water resources that can be used for sustainable and efficient energy production. Geophysical methods used in geothermal exploration derive great benefits from hydrocarbon exploration since many of these methods have evolved from approaches and solutions used to characterize oil and gas reservoirs. Although, the overall cost in hydrocarbon exploration are enormous in comparison to the geothermal developments, which can lead to the easy technology transfer, direct method application is often limited due to different geological characteristics of geothermal reservoirs. From the exploration and further imaging point of view the following aspects influence the exploration methods: application cost in respect to the site specifics and possibilities; the geological structure of the reservoir and identification of water-bearing/fractured zones; physical properties of geothermal media and possibilities of its extraction.

## 2.1 Geothermal environments

Geothermal energy is an energy source accumulated within the Earths interior as heat that in transferred to the surface. Scientific investigation of geothermal activity and Earths heat flow distribution is crucial to better understand interactions of plate tectonics and mantle dynamics at the global scale (Houseman & McKenzie, 1982; Jaupart & Parsons, 1985; Yuen & Fleitout, 1984). Some of these thermal processes can be ex-

plained by convection models towards deeper parts of the Earth, which is in agreement with the seismic observations and geochemical properties of mantle minerals (Turcotte & Schubert, 2002). Although the thermal processes within mantle and crust are important to estimate heat transfer and energy balance the more important are media circulation within the system thus making the operation cycle within time frame more accurate and predictable (Jaupart, 1981). Thus, the shallower systems accessible by the borehole are of special interest and may bring the geothermal energy to the surface that can be used for power and heat generation.

Geothermal systems are driven by heat transport processes that must be considered in advance of geothermal development. The knowledge about the heat transfer within the system provides an indicator for the economic of a geothermal project since the heat source can be characterized by its transition nature or permanent state (Barbier, 1997; Huenges, 2010). Transition state dominates for sedimentary aquifers which are characterized by smaller thickness that tends to cold down faster and decrease of production performance due to negative influence of cold water reinjection. The accurate estimation of geothermal energy transfer mechanism, however, is not the only parameter that has to be considered in the development of geothermal system as rock permeability may facilitate or attenuate fluid circulation within the system.

Geothermal resources can be found in different geological environments creating geothermal systems based on either the temperature or amount of thermal fluids. Huenges (2010) distinguished three main environments based on rocks type occurrence that host geothermal media where sedimentary, metamorphic and magmatic rocks influence the further utilization parameters. In most common situations, low enthalpy systems ($< 150\,^{\circ}\mathrm{C}$) dominate within sedimentary environments composing aquifers at shallower depths. On the other side, the high enthalpy reservoirs ($> 150\,^{\circ}\mathrm{C}$) are typical for metamorphic or magmatic rocks which form high pressure reservoirs suited for electricity production. Sedimentary reservoirs are composed from sandstone or carbonate rocks, while good reservoir parameters are achieved by high porosity and permeability value.

Drilling operation forms the obvious connection between underground geothermal system and surface installation where thermal energy is utilized for heating or electricity production purposes. Geothermal system characteristics differ substantially from typical hydrocarbon with respect to the drilling parameters, mostly due to high pressure and temperature. Thus detailed risk evaluation is necessary to successfully

complete the drilling operation at projected costs. Huenges (2010) indicated two main factors influencing the drilling operation: The first one corresponds to the technical aspects of the geothermal fluid extraction. The aggressive composition of geothermal fluids can cause corrosion or scaling (Corsi, 1986; Gallup, 1998), necessitating the use of other than standard materials or extraction techniques such as coatings, acidification or thicker than standard side walls, etc Criaud & Fouillac (1989); Hirowatari (1996); Sugama & Gawlik (2002). The second aspects is connected to the production quantities, as the flow rates are much higher to those known from hydrocarbon exploitation. This requires the application of of large diameters of the casing and special drilling techniques to perform large holes. In the consequence, the access to the reservoir to exploit the geothermal system makes the drilling operation the most essential and expensive part for geothermal projects. Cost reduction during this phase is therefore a main aspect that should be considered in order the make benefits from the geothermal energy usage in the most economic way.

Beside technical aspects of the drilling the most cost reductions can be acquired from the geological knowledge before drilling. The reliable imaging of the subsurface structures minimizes costs significantly since 50 % of the capital costs are accumulated within drilling operation Huenges (2010); Legarth (2008); Sanyal (2007); Sigfusson (2012). Moreover, the careful arrangement of borehole location and design of geothermal well performed in respect to existing structural features and specific of geologic conditions not only allow to minimize drilling risk but also to keep the sustainability of geothermal exploitation in terms of long-term operation.

Based on these requirements and in order to solve the target specific problems the existing surface exploration methods can be distinguish in three major categories (Barbier, 2002; Bruhn *et al.*, 2010; Buntebarth, 1984; Majer, 2003). These methods - seismic, magnetic and potential fields – have to be adopted independently to resolve the geothermal target. High imaging capabilities of geophysical methods allow to provide physical and structural parameters of the geothermal environment and its surroundings. Although, type of events as their parameters or even lack of information are individual for every geothermal system under consideration, however some specific operation can be unify in order to create geological model (Moeck *et al.*, 2010).

## 2.2 Active and passive seismic methods

Seismic methods are used to provide a detailed subsurface image of the geothermal reservoir highlighting the structural information and reflector imaging (Lees, 2004; Matsushima *et al.*, 2003; Sausse *et al.*, 2010; Unruh *et al.*, 2008), the location of fractured and tectonically changed systems with faults (Cuenot *et al.*, 2006) or extensional shear zones (Brogi *et al.*, 2003). Such an image is necessary to define the geothermal target area and in consequence to select the best borehole location, thus minimizing the drilling risk. It should be noted that the drilling costs account for half the capital investments costs(Brogi *et al.*, 2003). The corrosive effect of chemical components within the geothermal water and the larger size of the borehole ensure the effective fluid transfer puts the drilling operations at the top of an investment costs.

Seismic investigations include many sophisticated engineering processes and engaged significant computing power but generally based on three physical laws, derived in mathematically equivalent form within the last four centuries (Yilmaz, 2001). These laws – Huygens Principle, Fermat's Principle and Snell's law – are used mainly to structural identification, mapping of subsurface discontinuities or other targets of high impedance contrasts, imaging steeply dipping tectonic features and others. Different aspects of the site characteristic, its exploitation scenarios in correspondence to the limits of seismic imaging were discussed by Liberty (1998); Majer (2003); Niitsuma *et al.* (1999); Weber *et al.* (2005).

With respect to the source of seismic signals, exploration of geothermal systems can gain from both active or passive seismic techniques. In both variants the impulse response is measured in the form of an elastic wave, induced by an artificial or a natural source, respectively. Besides structural information obtained from reflected or refracted seismic waves, velocity values or their mutual relationship allows an interpretation to the physical characteristics of the reservoir rocks. With such an interpretation it is possible to derive porosity of rocks that host the geothermal reservoir by the application of the Gassmann-Domenico relationship (Berryman *et al.*, 2000; De Matteis *et al.*, 2008), moreover, when results from other methods are added it is possible to determine lithological characteristics of larger complexes (Bauer *et al.*, 2010, 2012; von Hartmann *et al.*, 2012).

General information concerns reflection seismic, its acquisition and processing I will present in chapter 3.1, while target oriented description of surveys and their data pro-

cessing are presented in chapter 4.2 and chapter 5.2.

**Active seismic**

Different seismic sources are used during acquisition processes to generate a seismic wave, however, explosive techniques and Vibroseis technology are the most often used in geothermal projects. Generated waves are recorded by geophones (or other seismic sensors) deployed in specially arranged layouts that are spread across the study site. Most surveys in the geothermal prospect used 2-D seismic reflection acquisition (Majer, 2003; Yilmaz, 2001), mainly focused on the imaging of P- wave reflections in order to create the subsurface image composed of the structural elements for exploitation horizons and faults located within sedimentary reservoirs. The application of 2-D reflection seismic is quite common and characteristics of many geothermal targets were defined that way (Batini & Nicolich, 1985; Casini *et al.*, 2010; Henrys & Hochstein, 1990; Lamarche, 1992; Moeck *et al.*, 2010; Soma & Niitsuma, 1997).

Originating from the hydrocarbon industry, the reflection seismic method is the most expensive among all geothermal exploration methods. However, with the progressive decline in prices of seismic surveys, even high resolution measurements can be adopted by the tight budget demands of geothermal projects allowing to takeover its knowledge and high-quality results. Nevertheless, the application of 3D seismic surveys in geothermal exploration is still rare and number of geothermal targets developed with the use of high resolution seismic is limited to a few places over the world (Bujakowski *et al.*, 2010; Casini *et al.*, 2010; Echols *et al.*, 2011; Lüschen *et al.*, 2011, 2014).

Seismic measurements may also provide valuable information when performed within existing boreholes. In the Kakkonda geothermal field, Japan, a reflection seismic measurement together with a technique called vertical seismic profiling (VSP) were used to provide detailed characteristics of the reservoir with special emphasis on fracture zone identification (Nakagome *et al.*, 1998). VSP is the technique of seismic measurements performed within a wellbore. While it exists in many variants, generally the source of the signal is located at the surface while the receiver or group of receivers are deployed inside wellbore. In the processing, VSP uses the reflected energy of seismic signals to correlate surface measurements to well data and additionally distinguish primary reflections (Hardage, 2000). Fractured reservoirs are common in areas affected by intensive geological processes and strong tectonic activities producing a complicated and attenuated seismic response. In such a situation, it is particularly important to

differentiate the origin of attenuated signals, therefore VSP measurements may correct primary reflection events, providing more detailed image of the subsurface geology in the borehole surroundings. Similar measurements and results were also obtained in the well-known geothermal sites - Soultz-sous-Forêts, France (Place *et al.*, 2010; Sausse *et al.*, 2010) or Mt. Amiata area, Italy (Brogi, 2004).

Similar to the VSP, results obtained from seismic surveys may also serve as the input data for integrated interpretation in conjunction with other geophysical methods. The quite common solution is to obtain the velocity structure coupled with electrical resistivity models. Such a joint interpretation based on results obtained from passive/active seismic measurements combined with MT/TEM electromagnetic surveys to indicate areas of high velocity contrast supplemented by low resistivity places, that may serve as a direct indicator of location of the main heat source within geothermal system. Many aspects of such a joint interpretation allowed to perform extensive studies and relationship between structural features, seismic manifestation and fluid content in respect to different geothermal systems, for example in volcanic (Jousset *et al.*, 2011) or sedimentary sites (Bujakowski *et al.*, 2010; Muñoz *et al.*, 2010a).

The tomography method is used to obtain the velocity structure along a measured profile (2D) or within an investigated volume (3D). An additional Vp and Vs differentiation allows to distinguish physical properties of reservoirs rocks due to their fluid content and porosity, i.e. Larderello, Italy (De Matteis *et al.*, 2008; Vanorio *et al.*, 2004) or Groß Schöeneback, Germany (Bauer *et al.*, 2006). Although the tomography algorithms are applied in order to resolve the velocity distribution, the method can deliver even a fourth dimension to the resultant model. Charléty *et al.* (2006) successfully applied the tomographic algorithm for data acquired at Soultz-sous-Forêts, France, to derive velocity model changes under constrained conditions by hydraulic stimulation spread over a long period of time. Such an analysis is particularly useful not only in differentiation of areas affected by hydraulic stimulation of the reservoir but also to determine the possible scenario of water circulation inside a target horizon.

Another technique of geothermal exploration that use seismic measurements is shear-wave splitting (SWS) that is particularly useful in the characterization of reservoirs that are already fractured (Rabbel & Lüschen, 1996; Rial *et al.*, 2005; Wuestefeld *et al.*, 2010). SWS can gain structural information based on induced or natural seismic events recorded by three component seismic sensors. It is based on the characteristic of the seismic wave that splits into two counterparts on the fractures edge. As the

consequence, the two resultant waves will differ with propagation speed, and the faster wave can be used to determine the cracks orientation due to its parallel polarization. Additionally, it is possible to estimate the fracture density as the velocity difference exhibited by the time delay of split waves. The effectiveness of the method strongly depends on the reservoir rocks where reservoirs of higher degree of homogeneity may provide results of higher accuracy (Rial *et al.*, 2005; Tang *et al.*, 2008).

**Passive seismic**

The passive seismic is well established in geothermal exploration, since micro-earthquakes (MEQ) have been observed in the close vicinity of many geothermal sites worldwide (Foulger, 1982; Ward, 1972). The mutual conjunction between seismic and geothermal activities allowed to highlight structural features like active fault zones that may indicate fluid pathways of geothermal fluids. Moreover, the constant monitoring of seismicity produced by hydraulic stimulation allows to verify the exploitation parameters of already established geothermal systems (Mayr *et al.*, 2011; Shapiro *et al.*, 2011). Development and practical consideration concerning the passive seismic and MEQ monitoring has been presented by many authors Duncan & Eisner (2010); Legaz *et al.* (2009); Wuestefeld *et al.* (2010). Its is also worth to note that such a stimulation and resultant micro-earthquake activity can enhance or even collapse the flow system of thermal fluids or even suspend the geothermal project due to civil protests (Häring *et al.*, 2008).

Although the application of passive seismic methods in geothermal exploration is addressed to visualize the distribution of micro-earthquake emission in respect to the production, it can be used in wider scale. For example, the velocity distribution acquired from earthquake monitoring in seismically active areas can provide lithological parameters by the application of the tomography method Muksin *et al.* (2013). Analysis of tomography results based velocities obtained from earthquake monitoring can be used in wider context, i.e Simmons *et al.* (2006) use the tomographic reconstruction to resolve the convective flow occurring in the mantle.

## 2.3 Electrical methods

Electrical methods can be applied due to Maxwell's equation making the rock's electromagnetic features achievable by the measurements of electrical resistivity in the subsur-

face (Simpson & Bahr., 2005). Depending on target, electrical methods can be selected based on the electrical potential methods and those that measure an electromagnetic field. Another division selects the source type which distinguish natural or induced actively. Modern methods (Barbier, 2002; Bruhn *et al.*, 2010; Pellerin *et al.*, 1996), however, aimed at deriving 3-D models based on the following classification: magnetotellurics (MT), controlled-source audio magnetotellurics (CSAMT), long-offset time-domain EM (LOTEM), and short-offset time-domain EM (TEM). CSAMT method uses the active electric field, and when used with TEM measurements can be applied for shallow targets or clay cap delineation at the maximum depth of 2000 m since reliable identification of deeper reservoir are disturbed by the transmitter effects (Pellerin *et al.*, 1996). Its long-offset equivalent is still in the development phase and the appropriate interpretation tools are expected to derive solution for geothermal exploration.

Deeper targets has profited greatly due to potential of naturally occurring electromagnetic waves. The electrical properties of these waves can be imaged by the magnetotelluric method (MT) that is based on the continuous measurement of total electromagnetic filed. Magnetotellurics has become the competitive geophysical methods since its formulation in the 50' last century by Tikhonov (Tikhonov, 1950) and (Cagniard, 1953). Generally, it based on the relationship between electric and magnetic filed components which modulates daily in magnitude and orientation. Such a ratio of electromagnetic components endorsed by their relative phases allows to determine the resistivity distribution in the earth interior. Moreover, due to a close relationship the electrical conductivity may serve as indirect temperature estimator that allows rejection of an inappropriate site locations (Spichak *et al.*, 2011).

The unique composition of both measurement fields makes benefits where magnetic field is enhanced by an electric counterpart on one side, however, the subtle anomaly due to boundary charges will be evident only for those sites providing the high-quality data obtained within optimally distributed measurements layout. It is worth to note that MT can reach targets as deep as several or hundreds of km and reveal their resistivity depending on the recorded frequency spectrum (Simpson & Bahr., 2005). MT has enjoyed a big success in the geothermal exploration due to prominent imaging of resistivity anomalies and temperature distributions associated with structural elements of geothermal sites worldwide. It has provided valuable characteristics of geothermal systems in correspondence to all geological environments, i.e. Beowawe (Garg *et al.*, 2007) or Coso (Newman *et al.*, 2008) in the USA, Kayabe area in Japan (Tan *et al.*,

2003), Hengill in Iceland (Árnason *et al.*, 2010; Gasperikova *et al.*, 2011), Mt. Amiata in Italy (Volpi *et al.*, 2003), Soultz-sous-Forêts in France (Geiermann & Schill, 2010), Taupo Volcanic Zone, New Zealand (Bertrand *et al.*, 2012), Bishkek in Kyrgyzstan (Spichak *et al.*, 2011) or Gross Schönebeck in Germany (Muñoz *et al.*, 2010b).

## 2.4 Potential methods

Potential field methods consist of gravity or geomagnetic measurements which based on the physical properties of reservoir rocks and provide data at considerably low resolution. Both methods provide usually good overall data quality in regional scale which makes the results appropriate estimation of the geothermal system borders, however, the resolution and penetration depth allows to identify only those structures of uncomplicated geometries located at shallower depth (Barbier, 2002; Bruhn *et al.*, 2010). Nevertheless both methods are attractive due complementary role and short acquisition time. Wide application spectrum emphasizes the importance of potential methods whereas their interpretation capabilities allows to better understand the connection between hydrothermal manifestation observed within sedimentary formations and adjacent geology.

Among wide spectrum of usage an interesting application of potential methods has been presented by Sugihara & Ishido (2008) and Yahara & Tokita (2010) in order to determine the fluid recharge volume with the application of a high-precision absolute/relative hybrid gravity-measurement technique. The microgravity monitoring measurements using an absolute gravimeter allowed to observe the gravity changes associated with geothermal exploitation. Within the accuracy range of a few microgals it was possible to observe the long term trends caused by fluid withdrawal in the Okuaizu and Hatchobaru geothermal power stations in Japan. Gravity data can also be used for delineating structural features in regional scale revealing a complex fault system. The interpretation the low-enthalpy geothermal system in Northern Portugal was performed by Represas *et al.* (2013) with correspondence to imaging of its structural features within the tectonically conditioned hydrothermal basin composed of fractured rocks. The 3D inversion model acquired from gravity measurements endorsed by gradient maps highlighted the presence of main fault zone and the location of gravity anomaly identified as a granite intrusion body. Many similar application of regional

scale delineation regarding to the basin environments modeling study were performed in Walker Valley, Nevada (Shoffner *et al.*, 2010) and Sydney basin (Danis *et al.*, 2011).

# 3

# CRS method

The common-reflection-surface (CRS) stack method (Jäger *et al.*, 2001; Mann *et al.*, 1999) allows to obtain simulated zero-offset (ZO) stacked section with significantly improved signal-to-noise (S/N) ratio compared to the classical common-midpoint (CMP) stack method. The CRS stack can be treated as extended form of the CMP stack technique. It is based on a second-order traveltime approximation and on extracting the traveltime information that have a form of so-called kinematic wavefield attributes.

## 3.1 Seismic reflection data stacking

In seismics, reflection data are obtained in the form of multiple recordings with varying source-receiver separation (offset) that allows for illumination of subsurface reflectors. Such a way of data gathering provides redundant information on subsurface structures and can be later used for a number of purposes. The main parameter, the S/N ratio can be improved by summing (stacking) seismic signal traces recorded with varying offsets. Additionally, the traveltime variation of reflection events defined as a function of source-receiver offset contains information on the distribution of seismic velocities in the subsurface. Beside borehole data and other geological knowledge, such dependency of offset and reflection traveltimes is the only information available for the construction of a velocity model. A good control of the velocity model is required for the transformation of measured data in time domain into a structural image of the subsurface in depth. Since the location of the signals originating from a common reflection point is initially unknown, a sophisticated data processing must be applied to find its location within the data. It is performed during a number of approximations and assumption

bringing a closer definition of subsurface structures. The standard method based on such a simplifications is called common-midpoint (CMP) stack technique and is widely used in seismic reflection data processing.

For the best performance of a comparison purpose between CMP and CRS seismic stack section it is necessary to establish the same coordinate system in which data are presented. Based on the notation proposed by Höcht *et al.* (1999) the measurement surface is defined by two vectors and spans in the midpoint and half-offset directions. The midpoint vector $\xi_m$ and half-offset $\mathbf{h}$ vector become scalars in 2D case and are as follows

$$\mathbf{h} = (\boldsymbol{\xi}_g - \boldsymbol{\xi}_s)/2 \quad and \quad \boldsymbol{\xi}_m = (\boldsymbol{\xi}_g + \boldsymbol{\xi}_s)/2\,. \tag{3.1}$$

## 3.2 CMP stack method

The multicoverage data stacking technique has been introduced by Mayne (1962) in the 60ies of the last century. In the CMP stack, seismic traces are subdivided into ensambles of the same midpoint location and different offsets. Such a collection of traces, called CMP gather, is designated to perform a summation (stacking) along specific stacking curves. The result of this process is a seismic section image of stacked CMP traces with improved S/N ratio. The method was originally designed for horizontally layered media where reflection events measured on different traces within the same CMP gather are focused in a common reflection point located directly below the CMP location. In nature, the structural image of the subsurface is more complicated and the common reflection point is shifted from the CMP point due to dipping of the reflector, as shown on Fig. 3.1.

In homogeneous media, the horizontal reflector leads to a solution where traveltimes within a single CMP gather can be expressed by the following equation:

$$t^2(h) = t_0^2 + \frac{4h^2}{v^2}, \tag{3.2}$$

where $t(h)$ is the traveltime of the reflection wave passing through the homogeneous medium with constant velocity $v$, and $t_0$ is called zero-offset time measured at the middle of the source-receiver pair. When considering a stratified medium, where the constant velocity requirement is valid only for a particular layer, the equation 3.2 has to be redefined (Taner & Koehler, 1969). It leads to a formula where traveltime $t(h)$

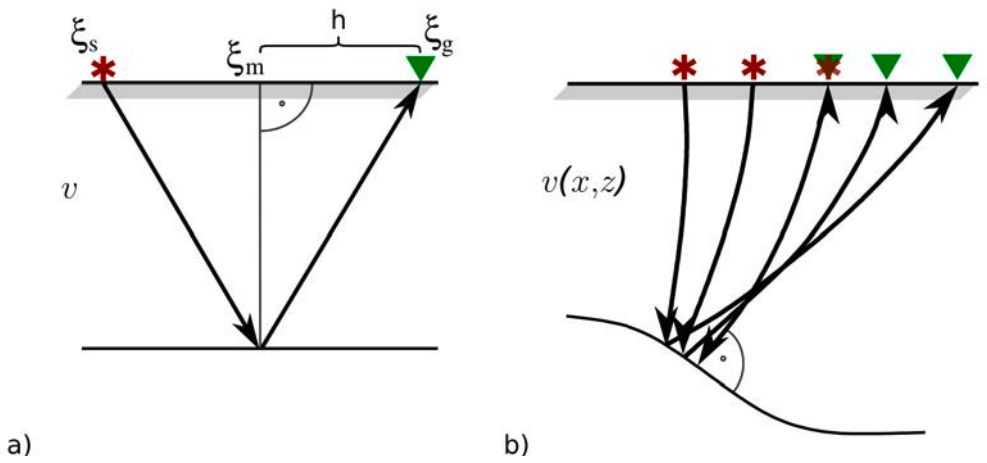


**Figure 3.1:** Theoretical reflection response from a flat reflector in homogeneous (a) and curved one in inhomogeneous (b) medium. Traveltimes recorded in the CMP gather are described by Eq. 3.2 and 3.4 respectively. Red stars indicate sources of the seismic wave while green triangles denote receivers on the measured surface.

is described by a second order approximation curve and velocity $v$ within each layer is approximated by the root-mean-square velocity $v_{RMS}$ as defined by equation 3.3

$$v_{RMS}^2 = \frac{1}{t_0} \sum_{i=1}^{N} v_i^2 \Delta t_i \quad , \tag{3.3}$$

The RMS velocity has no direct physical meaning since it is an effective velocity and not equal to the seismic velocity of the rock at depth. It is used to define the equation of reflection traveltime in a stratified medium (eq. 3.4), simplified to the form of a multilayer environment with smooth velocity changes. Thus, it can be used to determine traveltimes within a CMP gather with second order in $h$.

$$t^2(h) = t_0^2 + \frac{4h^2}{v_{NMO}^2} \quad , \tag{3.4}$$

where $v_{NMO}$, called normal-moveout velocity, determines the correction which removes the effect of longer traveltimes values with offset. This is performed during the velocity analysis which is based on appropriate velocity value determination for all reflection events within a CMP gather. Since the method development and its computer application proposed by Taner & Koehler (1969), the most commonly used method of stacking velocity analysis is the evaluation of the velocity spectrum (semblance analysis). In this method a set of traveltime curves that meets equation 3.4 is composed for each zero-offset time $t_0$ within the range of a specific velocity range.

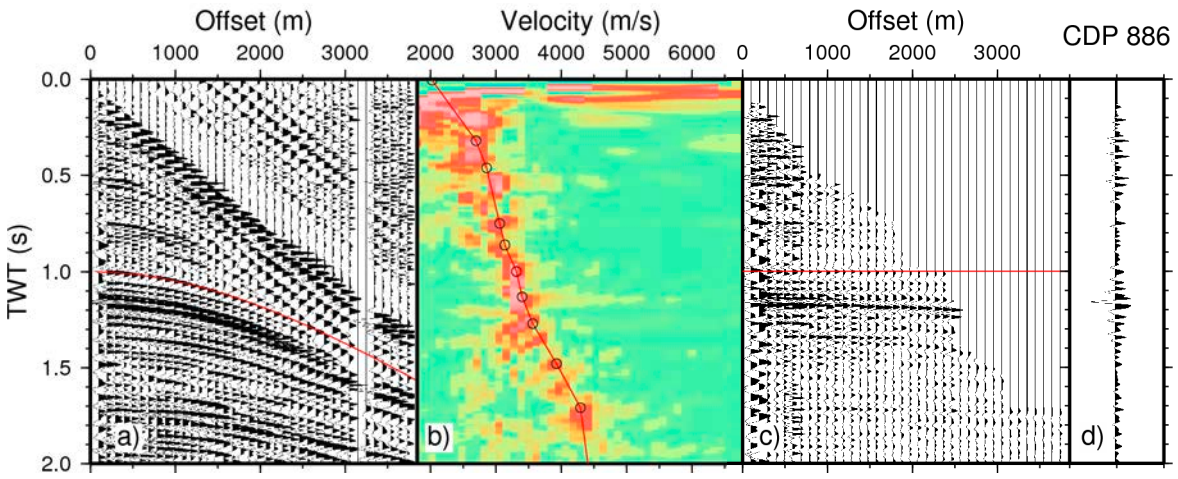


**Figure 3.2:** The concept of velocity analysis and CMP stacking performed in a CMP gather of Line 4. The supergather consisting of 7 CMPs (a) was used to increase coherency during velocity analysis performed in semblance panel (b). Picks (black circles) indicate velocity values that fit best to the reflection events due to the equation 3.4 as shown in figure (a). The velocity curve obtained in (b) is applied to the CPD gather and makes the reflection event NMO–corrected (c) that can be summed (d) in order to compose a stacked trace.

Then, the fit of the stacking operator to the data is quantified by measuring the coherency of the waveforms along the tested traveltime curves, as shown in figure 3.2. In the velocity analysis a commonly used measure of coherency is semblance (Neidell & Taner, 1971). Many others methods of the coherency analysis can be found in Castle (1994); May & Straley (1979); Taner & Koehler (1969). The highest coherency value corresponds to the traveltime curve that fits best to the reflection event. In consequence, the curve which links all picks of highest coherency value as function of time forms a stacking velocity model. The semblance coherency measure is given by:

$$C_S = \frac{1}{N} \frac{\sum \left(\sum_{i=1}^{N} f_{i,t(i)}\right)^2}{\sum_t \sum_{i=1}^{N} f_{i,t(i)}^2} \quad , \tag{3.5}$$

where $N$ is the number of traces based on the coherency calculation performed over the window time, and $f_{i,t(i)}$ describes amplitude value on the $i$th trace at a specific time $t(i)$. In practice, the summation calculation along the traveltime curve is carried out within a small window which center lies on that curve. Based on that obtained stacking velocity function, it can be incorporated into equation 3.4 as the normal-moveout velocity. Once the normal-moveout correction is applied to each trace within

a CMP gather traces can be stacked along the offset axis. The equation 3.6 describes the NMO time correction

$$\Delta t_{NMO} = t_0 \left( \sqrt{1 + \frac{4h^2}{v_{NMO}^2 t_0^2}} - 1 \right) \quad . \tag{3.6}$$

Practical consideration of the velocity analysis presented by Al-Chalabi (1973) or Hubral & Krey (1980) show the misfit between stacking velocity curve and second-order traveltime approximation. This effect, called spread-length bias, is caused by many factors but mainly due to lateral inhomogeneities recorded along the offset in the subsurface and the finite offset aperture. The offset factor plays a significant role on the resultant stacked image section as well as in tomography and inversion technique (Duveneck, 2004; Zhang & McMechan, 2011), where its maximum value must be selected with care.

Although the NMO technique fits well to all aspects of horizontally layered media, it fails for dipping layered media acquired in the CMP stack, by enhancing reflections with a particular slope and simultaneously attenuating reflections with another slope. An additional correction can be applied to minimize the effect of dipping reflector. The method called dip moveout (DMO) allows horizontal and dipping reflectors to be stacked with the same NMO velocity. Further readings concerning DMO technique can be found in Hale (1984), Deregowski (1986) or Notfors & Godfrey (1987) but the method will not be more discussed through this thesis.

## 3.3 CRS stack method

As described in secion 3.2, the CMP stack defined as a second order traveltime approximation is determined in the offset domain. With additional domain, oriented in the midpoint direction, the stacking operator becomes a stacking surface defined in the 3–dimensional time–midpoint–half–offset space. This assumption leads to the determination of a reflection response from the subsurface, spanning through several neighborhood traces in midpoint direction.

The CRS stack method (Jäger *et al.*, 2001; Mann *et al.*, 1999) is considered as the new concept of the reflection seismic method which is aimed to use a stacking operator determined as a second order traveltime approximation. It is used to perform a simulated zero-offset stacking procedure of reflection events in the neighborhood of

each zero-offset sample trace $(t_0, \xi_0)$. To include an additional domain, the trajectory of the stacking operator determined by equation 3.6 must be then redefined, and the new traveltime approximation in the vicinity of the zero-offset point $(t_0, \xi_0)$ has the following form (Schleicher *et al.*, 1993):

$$t^2(\xi_m, h) = \left(t_0 + 2p^{(\xi)}\Delta\xi\right)^2 + 2t_0\left(M_N^{(\xi)}\Delta\xi^2 + M_{NIP}^{(\xi)}h^2\right) \quad . \tag{3.7}$$

To make full usage of the CRS stacking method, the traveltime approximation from equation 3.7, which is defined in the 3–dimensional time–midpoint–half–offset space, must be described by three independent parameters. Those parameters $p^{(\xi)}$, $M_N^{(\xi)}$, and $M_{NIP}^{(\xi)}$ are responsible for creating the stacking surface and are calculated for each sample trace independently. Their detailed description is given in the next paragraph. After the three parameters are calculated, the stack is performed in the way of the coherency analysis. Thus, the CRS stack technique can be treated as an extended form of the common-midpoint stack technique as described in the previous section, and it relies on traveltime information that has the form of so-called kinematic wavefield attributes.

When considering an inhomogeneous medium with a curved reflector as shown in Figure 3.1b, it can be seen that the reflection event is not limited to a single midpoint location. Each individual location is named common-reflection point (CRP) and when linked to the surface, it creates the CRP trajectory which defines the locations of all primary reflection events. Hence, its value is initially unknown, however, it can be resolved by a second-order traveltime approximation which determines the corresponding CRS stacking operator. As proved by Höcht *et al.* (1999) the conjunction of the determined kinematic wavefield attributes $p^{(\xi)}$, $M_N^{(\xi)}$, and $M_{NIP}^{(\xi)}$ together with additional near-surface velocity information allows to calculate CRP trajectory approximation for a given zero-offset sample $(t_0, \xi_0)$. Physically, the attributes can be seen as a two hypothetical wavefronts of Normal Incidence Point (NIP) and Normal (N) waves emerging at the surface as shown on Figure 3.3.

There are big advantages when using the CRS stacking surface instead of stacking trajectories known from the CMP stacking method. The biggest improvement is due to the significantly larger number of traces contributing to the stack at each zero-offset location. In consequence, the stacked sample trace is characterized by an improved S/N ratio in comparison to the same trace obtained with conventional CMP stacking technique as described in section 3.2. Especially, in case of low fold data sets, when

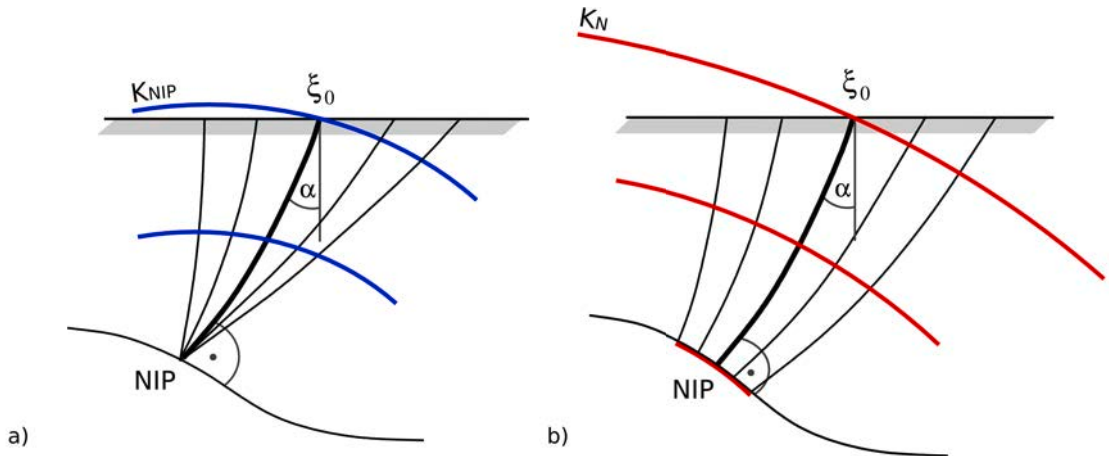


**Figure 3.3:** Sketch of theoretical aspects of NIP wave and normal wave, with hypothetical waves emerging at location $\xi_0$ on the surface due to a point source (a) and an exploding reflector (b). Quantities $K_N$ and $K_{NIP}$ describe the wavefront curvature of the normal and NIP wave, respectively. Additional thicker black lines indicate the radius of the curvature. More details and parameter description is given in the text below.

the number of traces is not sufficient to perform a reliable velocity analysis, the CRS may fulfill all stacking demands.

The application of kinematic wavefield attributes can be used in different ways and has a long history of usage in many seismic data processing techniques. The first attempt to make benefits of it was conducted by Hubral (1983) by means of a geometrical spreading correction. Another application was proposed by Mann (2002) to determine parameters of the projected Fresnel zone. Significant studies has been conducted by Duveneck (2004), who developed the idea of tomographic inversion based on the velocity data extracted from the kinematic wavefield attributes.

A similar solution of using a different stacking operator where the characterization of wavefront is determined by traveltime, radius of curvature and angle of incidence (Shah (1973), Hubral & Krey (1980)) has been proposed by (Gelchinsky, 1988) in the method called common reflecting element (CRE). Its further implementation named multifocusing homeomorphic imaging (MHI) was developed by Gelchinsky *et al.* (1999) and Landa *et al.* (1999, 2010) and Berkovitch *et al.* (2008).

#### Kinematic wavefield attributes

The three coefficients of the hyperbolic second-order traveltime approximation de-

fined by equation 3.7 characterize the hypothetical wavefronts that are emerging at the surface location $\xi_0$. Its quantities are determined as the spatial derivatives of the hypothetical wavefronts related to the NIP and normal wave experiment. As shown in Figure 3.3, the meaning of the normal radius of curvature is related to the reflector curvature, while the NIP-wave radius of curvature to its depth.

As the CMP reflection coincides with the reflection that passes through the NIP point and is equal to the second order derivative in the offset domain (Chernyak & Gritsenko, 1979; Hubral, 1983) it is allowed to assign the $M_{NIP}^{(\xi)}$ parameter to the NIP wave second spatial derivative. When considering a normal wave experiment, the quantity of $M_{NIP}^{(\xi)}$ can be explained as the second horizontal traveltime derivative of its wavefront when the source is placed at NIP point on the reflector (see Fig. 3.3a). On the other hand, the part of the reflector in the vicinity of the NIP point location, interpreted as the exploding reflector, is normal to the wavefront emerging at the $\xi_0$ location of the zero–offset ray (see Fig. 3.3b). Thus, its quantities $p^{(\xi)}$ and $M_N^{(\xi)}$ can be explained as the first and second spatial traveltime derivatives respectively.

For the considered quantities that are used to determine NIP and normal wave emerging at $\xi_0$ surface location along the seismic line, the parameters $M_{NIP}^{(\xi)}$, $p^{(\xi)}$ and $M_N^{(\xi)}$ can be written (Duveneck, 2004) in the following form (under the assumption that the near-surface velocity $v_0$ is constant locally and subsurface velocity differs only along the seismic line):

$$M_{NIP}^{(\xi)} = \frac{\cos^2 \alpha}{v_0} K_{NIP} \tag{3.8}$$

$$p^{(\xi)} = \frac{\sin \alpha}{v_0} \tag{3.9}$$

$$M_N^{(\xi)} = \frac{\cos^2 \alpha}{v_0} K_N \quad , \tag{3.10}$$

where $K_{NIP}$ describes the wavefront curvature of the emerging NIP wave at surface $\xi_0$ location, while $K_N$ refers to its normal wave counterpart. Emergence angle $\alpha$ denotes the relative angle of the normal ray at $\xi_0$ to the measurements surface. Those three parameters, defined as the traveltime derivatives related to an emerging wavefront, can be incorporated to equation 3.7 in order to obtain the 2D CRS operator:

$$t^2(\xi_m, h) = \left( t_0 + \frac{2sin\alpha}{v_0}(\xi_m - \xi_0) \right)^2 + \frac{2t_0 cos^2\alpha}{v_0} \left( \frac{(\xi_m - \xi_0)^2}{R_N} + \frac{h^2}{R_{NIP}} \right). \tag{3.11}$$

Instead of the wavefront curvature parameters $K_{NIP}$ and $K_N$, the radius of wavefront can be used to preserve conformity of equation 3.11 with the one originally proposed by Mann *et al.* (1999). Thus, the radii of wavefront have the reciprocal value of the curvature parameters $K_{NIP}$ and $K_N$ that describe NIP and normal wave, respectively. Although the true values of curvature and depth of a reflector in complex media are not equal to the measured values of $R_{NIP}$ and $R_N$, their real values can be recovered with a seismic inversion method by the use of NIP-wave tomography, as has been proposed by Duveneck (2004). Under the additional assumption, that $\Delta\xi = 0$ and by comparison to equation 3.4 the normal-moveout velocity can be expressed by the use of the kinematic wavefield attributes $R_{NIP}$ and $\alpha$ and expressed in the following form:

$$v_{NMO}^2 = \frac{2v_0 R_{NIP}}{t_0 \cos^2 \alpha} \quad . \tag{3.12}$$

Figure 3.4 shows the comparison between normal moveout velocities obtained with CMP and CRS. CMP velocities were determined with equation 3.6 during velocity analysis in a semblance panel as described in Figure 3.2, whereas CRS velocities were determined with equation 3.12 by use of the $R_{NIP}$ and $\alpha$ kinematic wavefield attributes.

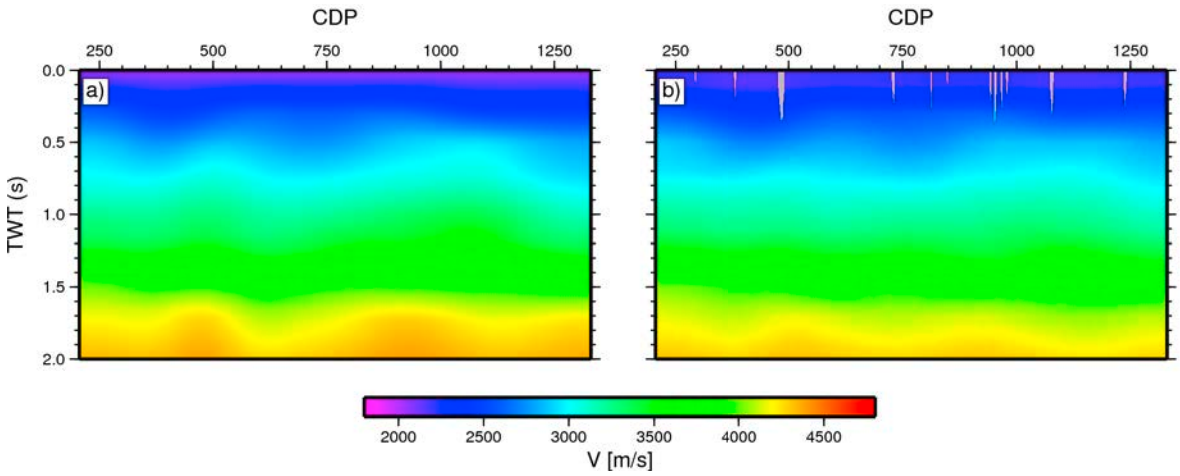


**Figure 3.4:** Comparison of normal moveout velocities obtained with the CMP (a) and CRS (b) method.

The CRS stack operator defined by equation 3.11 which is determined by the three parameters refers to the case of 2D seismic data only. As proposed by Höcht (2002), a CRS operator can also be obtained for 3D volumes but instead of three it involves the

assistance of eight parameters as shown in the equation below:

$$t^2(\boldsymbol{\xi}_0 + \Delta\boldsymbol{\xi}, \mathbf{h}) = \left(t_0 + 2\mathbf{p}^{(\xi)}\Delta\boldsymbol{\xi}\right)^2 + 2t_0\left(\Delta\boldsymbol{\xi}^T\underline{\mathbf{M}}_N^{(\xi)}\Delta\boldsymbol{\xi} + h^T\underline{\mathbf{M}}_{NIP}^{(\xi)}\mathbf{h}\right) \quad . \tag{3.13}$$

As already denoted by the equation 3.1 the coordinates of midpoint-half-offset space are determined by $\boldsymbol{\xi}_m$ and $\mathbf{h}$ vectors. The quantity of parameter $\mathbf{p}^{(\xi)}$ is defined by a two-component vector, while $\underline{\mathbf{M}}_N^{(\xi)}$ and $\underline{\mathbf{M}}_{NIP}^{(\xi)}$ are two symmetric 2×2 matrices.

By the translation from the case of 2D seismic data to a 3D seismic volume, the CRS operator parameters can be assigned with the same kinematic characteristics to the NIP and normal waves. Thus, the vector $\mathbf{p}^{(\xi)}$ is determined by the first horizontal traveltime derivatives, whereas the matrices $\underline{\mathbf{M}}_N^{(\xi)}$ and $\underline{\mathbf{M}}_{NIP}^{(\xi)}$ are second traveltime derivatives of emerging normal and NIP waves respectively.

**Processing and practical consideration**

CRS data processing makes use of kinematic wavefield attributes to determine an optimum stacking operator for each zero–offset sample trace. Since the attributes can be obtained only for existing reflection events within a multicoverage dataset they give measurable benefits by providing additional sections/volumes. Such results are the basis for a qualitative assessment of the NIP and normal wave parameters, where detected reflection events are characterized by high coherency values. Additionally, the assessment provides information concerning reliability of acquired kinematic attributes. It is worth to mention that the coherency value measured for a reflection event can be influenced by other factors i.e its overall S/N ratio, the number of traces used for processing and the shape of the second-order hyperbolic traveltime approximation defined by equation 3.7 and 3.13.

At the end of the CRS processing chain one can obtain a zero-offset stacked section and three additional sections of wavefield kinematic attributes and a coherency section obtained at each step. When applied to a 3D multicoverage dataset, the number of kinematic attributes increase up to eight instead of three obtained during 2D data processing. The results of a CRS processing example sequence for multicoverage 2D and 3D datasets are presented on Figure 4.7-4.8 and Fig. 5.8.

Simultaneous determination of three kinematic wavefield attributes defined for each zero-offset sample trace involves a great deal of time, even for modern computers. This is especially the case, when a 3D multicoverage dataset is processed and up to eight parameters need to be found. Depending on the overall quality of a dataset which

is related to the acquisition technique, the wavefield attribute determination can be divided into singular step-by-step search processes.

In the 2D CRS data processing flow, originally proposed by Mann *et al.* (1999), Mann (2002), the first step consists of CMP stacking in each CMP gather under the assumptions that the parameter of wavefield attribute obtained from equation 3.7 for the 2D case and equation 3.11 is limited to $\Delta\xi = 0$. In the result, due to an automatic velocity analysis, a stacking velocity is obtained and can be incorporated to equation 3.9 in order to obtain $R_{NIP}$ and $\alpha$. As the stacked section is acquired from the previous step, it can be used to perform a search for the first–order traveltime derivative from equation 3.9 defined by the parameter $\alpha$ under the restriction of $h = 0$ and $R_N = \infty$. The last parameter search for the second–order travelitime derivative $R_N$ requires the assumption of $h = 0$ for the CRS operator. After all three wavefield attributes are obtained, the last processing step is based on a local optimization, where each of the wavefield attributes can be calculated to obtain a stable CRS operator for the considered multicoverage dataset. The success of this operation relies on the sufficient S/N of the reflection events and an adequate number of traces.

Optimum results acquired during the parameter search procedures as defined with equation 3.7 and 3.13 strongly depend on the quality of dataset. Concerning reflection traveltimes, they decrease especially with distance from the ZO sample trace position in both midpoint and offset directions. Therefore, both the values of aperture selected in three parameter searches and the final CRS stacking step should be selected with special care to obtain appropriate results. The initial aperture estimation relies on the geologic information, however, its further values depend on the projected Fresnel zone. Its size is based on the intersection between first Fresnel volume and the reflector, thus it can be treated as a good indicator to determine $\Delta\xi$. More accurate width values of the projected Fresnel zone are provided through the processing sequence due to an automatic parameter search. The size of the projected Fresnel zone can be determined by the following equation:

$$F_{HW} = \frac{1}{cos\alpha}\sqrt{\frac{V_0}{2\omega\left|\frac{1}{R_N} - \frac{1}{R_{NIP}}\right|}} \quad , \tag{3.14}$$

where $\omega$ denotes the dominant frequency of the recorded seismic signal. Again, by limiting the maximum displacement $\Delta\xi = 0$, the stacking surface changes to the classical CMP form, known from equation 3.6 with one CMP gather only.

If the selected aperture is too small at larger offset, it will reduce the confidence level for the attribute determination. The same effect can be observed in conventional NMO stacking procedure, as the offset space is the common for both methods. On the other hand, if the selected aperture is too large, the parameter determined for the stacking operator might not satisfy the condition at the ZO sample trace location but only at larger offsets. The visual aspect of aperture determination in the half-offset-midpoint space is presented in Figure 3.5 whereas examples of offset and midpoint aperture tests and their effects on the dataset characteristics are presented later in section 4.4 in Figure 4.7.

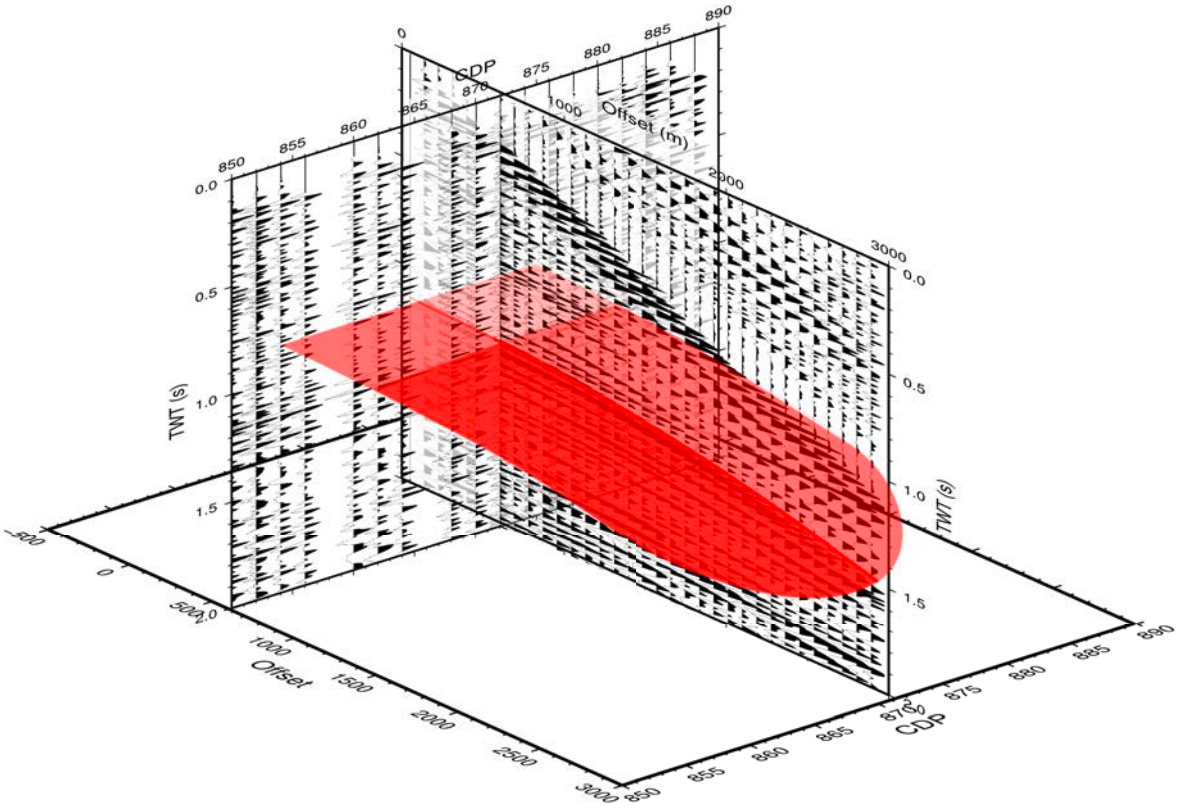


**Figure 3.5:** Visual representation of the CRS apertures. Description of particular elements in the text below.

As already mentioned in section 3.2, the *spread-length-bias* effect coincides with the second-order traveltime approximation, thus the aperture selections may affect it at some degree. Special attention needs to be taken in order to control its behavior, especially in a very complicated structural subsurface regime, therefore a proper

determination of optimum wavefield attributes may encounter major obstacles.

The general approach in conventional NMO analysis involves that the velocity values are picked at certain traveltimes only due to their high coherency. The remaining values are interpolated to make the velocity curve complete. In consequence, due to the interpolation at short offsets, the wavelet characteristics become distorted and a loss of temporal resolution can be observed. This effect, known as NMO stretch (Buchholtz, 1972; Yilmaz, 2001; Zhang *et al.*, 2011) must be removed in the further processing chain. Since the second-order approximation in CRS processing allows the operator to be determined independently for each ZO sample trace, such an effect does not appear for the considered ZO location.

Although the interpolation between highly coherent values of the stacking NMO velocity leads to a stretching effect, the sample-by-sample CRS processing may also cause small irregularities within determined attributes, thus the criteria for a stable operator calculation may not be fulfilled and these fluctuations can occur with all calculated attributes affecting further methods that are based on the CRS results.

It is worth to mention that the derivatives of traveltimes, as the kinematic wavefield attributes, keep the wavelet characteristics invariant of the recording time. Moreover, as the CRS stack meets the criteria of the paraxial ray theory, the variations of the kinematic wavefield attributes, that are proportional to the traveltime derivatives, remain smooth along the reflection event. The above statements allow to apply smoothing procedures to kinematic wavefield attributes before the final stacking to enhance its result. Different smoothing procedures were selected by the authors in order to meet a particular demands, i.e. Duveneck (2004) proposed an event-consistent smoothing algorithm to speed up the computation time in order to prepare the attribute sections for the tomography, Mann *et al.* (1999) originally proposed a local optimization algorithm and this algorithm was also used in this thesis.

**Advanced techniques and new developments in the CRS**

Kinematic attributes obtained during second-order traveltime approximation by means of the CRS stack can be used to determine laterally inhomogeneous 2D/3D velocity models that can be applied for further processing, i.e. depth imaging. The NIP-wave tomography method has been originally developed by Duveneck (2004) and applied by Dümmong *et al.* (2007) and Baykulov *et al.* (2009). It assumes the use of provided attribute sections/volumes serving as input data while their values are selected

by the number of pick locations in the CRS stacked zero-offset sections/volumes. Since the NIP-wave tomography is based on smooth model and reflection points assumed to be independent, only a few picks are necessary. The forward quantities are obtained by iteratively determined dynamic ray tracing along normal rays, while the calulation of Frechet derivatives is based on perturbation theory.

The CRS method has become the starting point for many other more sophisticated and advance processing methods. One of these is the partial CRS stacking method, originally proposed by Baykulov & Gajewski (2009). It allows to obtain regular and uniform seismic section/volume and can be used to fill in the gaps between traces within a sparse dataset. The idea of partial CRS stack is based on the summation of stacking surface that coincidences locally with the specific point defined in half-offset–midpoint domain of a chosen CMP location. In the results, the CRS supergather is obtained that consists of desired points determined by the summation surface. That surface is consistent to the surface of the CRS stack but smaller in size. Beside the data infill and overall S/N improvement, the partial CRS stack assumes the amplitude preservation that allows a method to be applied in wider spectrum (Baykulov *et al.*, 2009).

In the time migration methods, the velocities defined at the apex of migration operator are usually obtained in the iterative way from a stacking velocities. Another method to derive the migration velocities based on the CRS kinematic attributes was proposed by Mann (2002) and Mann *et al.* (2003). It based on the assumption that diffraction response can be obtained by the CRS operator, thus mapping the diffraction apex. Although, the method has limitation due to the selective characteristics based on points mapping, however it can be used as first approximation of the subsurface. Another solution to use the CRS attributes for Kirchoff depth migration was proposed by Jäger (2005). With the CRS attributes it was possible to estimate the minimum migration aperture and thus enhance the resultant seismic image, mainly by attenuating the migration artifacts and preventing an aliasing of migration operator. Spinner & Mann (2005) and later Spinner (2007) has used the CRS attributes and the idea of minimum–aperture in time migration. The main aim of this approach was to gain the stability of migration aperture and in consequence to lower the dependency from velocity model errors, that was considered as limitation of depth counterpart. A general approach of minimum time migration focused on accurate determination of location and size of migration aperture. Determined, with the assumption of straight

ray, the migration operator makes it possible to obtain the improved migrated image and preserved amplitude.

The latest developments of CRS technique focused on the structural imaging within the resolution beyond a half of wavelength. Such a structural details are usually associated with karst and fractured or pinch-out structures that are important in further interpretation. Landa *et al.* (1987) proved the useability of diffracted waves to image and highlight such a small structures. Dell & Gajewski (2011) make a usage of the CRS method to separate diffraction from reflection primary events in time domain, whereas the previous works of Krey (1952) and Kunz (1960) suggest the relationship between faults and diffracted waves. Generally, the key target of the algorithm is based on such a usage of CRS attributes, that makes the possible to attenuate the reflection events in the poststack domain while make a simultaneously summation of diffraction ones in the way of partial CRS stacking. Taking those processes together a new CRS-based workflow of seismic data processing can be established.

# 4

# Application to 2D reflection seismic data from the Alberta basin

## 4.1 Geological overview

The Western Canadian Sedimentary Basin (WCSB) is an extensive basin in Western Canada covering an area of $1.4 \times 10^6$ km$^2$ , similar in size to the area of Germany, France and Spain taken together. It is bounded by the Rocky Mountain Fold and Thrust Belt in the Southwest and the Canadian Shield in the Northeast (Fig. 4.1). It extends from the southwestern part of the Northwest Territories, to the southwestern part of the Manitoba province. The main deposition axis of the WCSB, called the Alberta Basin, has the form of northeastward-tapering wedge composed of supracrustal rocks covering the crystalline basement. The thickness of the wedge decreases gradually from about 6 km in the center of the main deposition axis in front of the Rocky Mountain fold and Thrust Belt (RMFTB), before completely tapering out close to the northeastern part of the Canadian Shield margin.

The origin and evolution of the WCSB is directly linked to the process that influenced the tectonic evolution of the Cordilliera as a result of North American craton interaction with lithospheric units to the west (Monger & Price, 1979) and its later orogenic deformation process (Porter *et al.*, 1982). Bally *et al.* (1966) and Price & Mountjoy (1970) proposed two stages of the WCSB development based on changes in the composition and origin of the clastic rocks within the sedimentary layers. The first, a Late Proterozoic to Late Jurassic stage, correlated with the rifting that initiated the Cordilleran margin, its nearby ocean basin and the continental terrace wedge. The

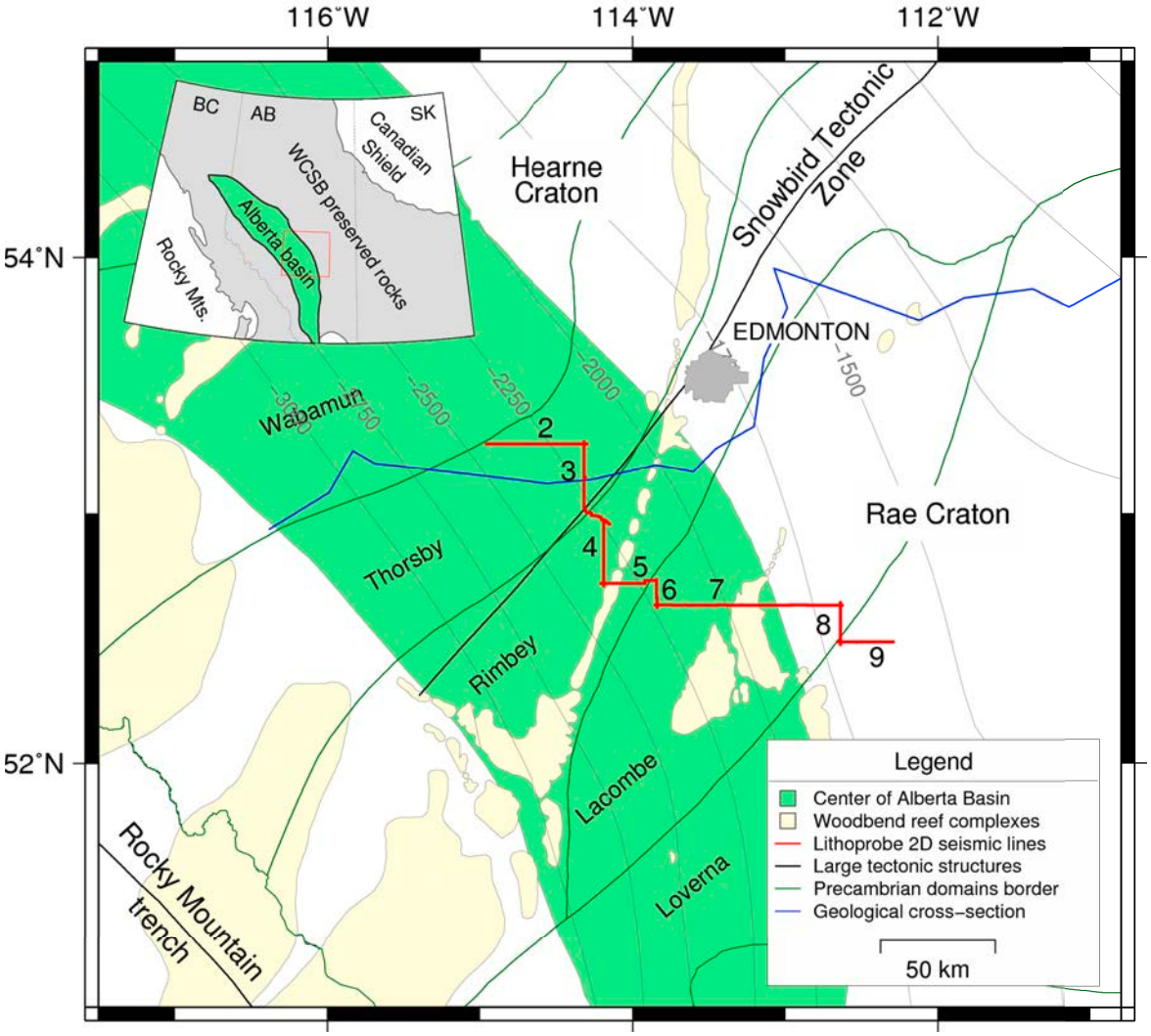


**Figure 4.1:** Location of the Central Alberta Transects seismic reflection lines, with an outline of main structural units within WCSB observed on seismic section (compiled after Mossop & Shetsen (1994)). Contour lines marked by grey indicate depth of the Precambrian basement below the sea level.

second, a Late Jurassic to Early Eocene stage, corresponds with the accretion of tectonically transformed oceanic terranes emerging in the foreland basin with the thickest deposition value in the southwest.

### Stratigraphy

The stratigraphy and evolution of the lower Paleozoic sedimentary cover has been

investigated by Stott & Aitken (1993) and Kent (1994) and Slind *et al.* (1994). Within the study area, the sedimentary succession above the basement collage consist of 500 to 800 m deposits from the Cambrian to the Lower Middle Devonian period. The thickest Cambrian succession of about 500 m, consisting of Basal Sandstone, shallow marine carbonates of the Cathedral, Eldon and Pika formations, shows northwest alignment to the continental margin. Clastic sedimentary rocks of the Upper Cambrian strata are overlain unconformably by the 70 m thick Upper Ordovician carbonates of the Red River Formation. The Devonian Elk Point sediments consist of Ashern clastic units while Winnipegosis and Prairie formations are mostly carbonate and salt with a total thickness of 150 to 180 m. These strata unconformably overlay the older Ordovican-Cambrian formation.

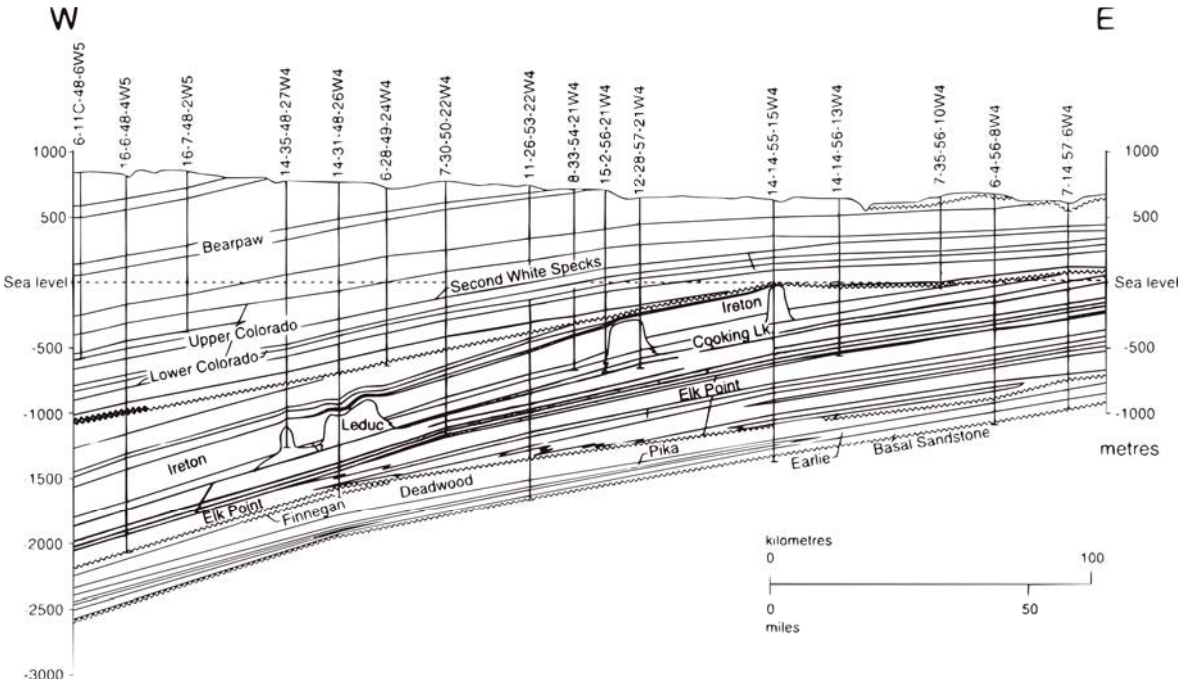


**Figure 4.2:** The geological cross-section of the Alberta basin east of Rocky Mountains. The section shows the general trend of southeast dipping and the reef structure (simplified after Mossop & Shetsen (1994)). For the line orientation see Fig. 4.1. Vertical exaggeration is approximately 40.

### Target horizons

There are others sedimentary layers of particular interest for geothermal exploration due to their unique features. These were selected based on physical rock properties

acquired from boreholes.

The Nisku Formation found in B.A. Pyrcz No. 1 well between 1,496.3 and 1,548.8 m is surrounded by two dolomitic complexes – the Woodbend Group on top which partly contains shales, and the Winterburn Group at the bottom also containing shales and additionally anhydrites. It varies between 40 to 60 m in thickness throughout central Alberta plains and exceeds 100 m in western part within the Winterburn Basin, while it thins slightly over the Leduc Formation (Stoakes, 1987; Watts, 1987). The layer of crystalline dolomite with minor admixture of shales and anhydrite whose exact contents depend on the environment in which they were formed. Leduc reefs are usually developed in pinnacle forms. The porosity of limestone rocks occurring in Nisku Fm. varies between 9.7 to 10.4 % while their relative permeability within $CO_2$2-brine system varies between 21.0 to 45.9 mD (Bachu & Bennion, 2008). The Leduc formation of Frasnian age occurs as reefal buildups developed in shallow water environment and platform complex with the thickness of 180 to 300 m. It consists of a mixture of shallow water reef facies, mostly stromatoporoids and skeletal mudstones, which are mainly dolomitized. This process usually creates a natural pit-like cavity in the rocks, hence the vuggy porosity in the Leduc formation varies between 2 and 14 % while permeability depends on the pore orientation and reaches the maximum value of 26.7 mD (Stoakes, 1980). The Cooking Lake formation covers the area of central Alberta and is limited in the south by the Woodbend shelf. Its thickness varies from 60 to 90 m at a depth of about 1,900 m. The formation occurs as the carbonate platform of limestone and their dolomitized counterparts including mudstones and wackestones. It is overlain by the Leduc Formation reefs and overlies the Beaverhill Lake Formation. Measurements performed by Bachu & Bennion (2008) for the drainage cycle in $CO_2$-brine systems provide permeability values up to 65.3 mD and a porosity as high as 9.9 %. The Keg River formation covers the area from the Precambrian shield to the north- east corner of British Columbia. Among different sub-basins, it occurs as a vuggy or cryptocrystalline limestone with minor admixture of dolomite, those thickness varies from 10 to 300 m.

**Structural features within the Basin**

The Central Alberta Transect crosses the boundary between the Rae province and the western part of the Archean Hearne Craton, called Snowbird Tectonic Zone, a structural discontinuity that can be traced from the Canadian Cordillera to the shore

of the Hudson Bay. The Snowbird Tectonic Zone can be distinguished on potential field images giving the strong pattern on both Bouger and magnetic anomaly images (Ross *et al.*, 1991; Villeneuve *et al.*, 1993).

In contrast to the sedimentary layers, structural features of the basement have not been widely investigated. One of the reasons for that is an insignificant number of boreholes that penetrate the basement rocks. In consequence, this limits the structural analysis to the borehole surroundings or large scale regional analysis. Nonetheless, based on that sparse information a large tectonic unit crossing through the central part of Alberta of about 2000 km long and with a general NE orientation called Snowbird Tectonic Zone (STZ), can be distinguished. The presence of the STZ was also confirmed by the analysis of potential field measurements performed by Ross *et al.* (1991); Sharpton *et al.* (1987) and Villeneuve *et al.* (1993). Results from these measurements helped to characterize the regional setting of the STZ from Alberta to the Hudson Bay, where it can be observed as clearly visible signatures on magnetic and Bouger anomaly maps. It is worth to note that a few anomalies are not directly correlated with dipping basement observed on seismic sections. These additional patterns were investigated by Ross *et al.* (1995) and seem to represent mid-crustal thrust faults.

There are some minor disturbances in the basement topography, most likely caused by the local tectonic activity linked to the basement faulting. In other cases, the surface of the crystalline basement appears to be smooth. Detailed investigations based on Lithoprobe seismic reflection profiles did not provide more details due to its limited resolution, which is 20 m. Nevertheless, the detailed analysis of available cores from the boreholes that penetrate the basement outcrop investigated in the Lower Paleozoic Project, provides the tectonic evidence on small scale basement faulting existence (Hein & Nowlan, 1998). This evidence for existence of fault zones oriented NE and located in central Alberta has been documented during the 3D seismic measurements near Joffre Field, where hydrocarbons have been found within the Nisku formation. Earlier measurements and data acquired in South Alberta proved the NE to NNE faulting orientation in post Leduc period Haites (1960).

**Natural resources within the WCSB**

The Western Canada Sedimentary Basin is considered one of the worlds largest reservoirs of hydrocarbons. It contains vast reserves of oil, natural gas and also has

huge reserves of coal. The bulk of the oil and gas resources of Canada and nearly all of its oil sands lie in the Alberta province (Stringham, 2012).

Although, the Alberta province contains most of the reserves of crude oil within the WCSB, its production will decline of about 40 % from 2006 to 2016 whereas its pools have been almost depleted (Davidson & Elsner, 2005). Light and heavy crude oil types are mostly accumulated in the Devonian reefal, while the Cretaceous ones occur mainly in porous sands, reaching 50.7 and 26.6 % in recoverable oil reserves in Western Canada respectively. Pool size and its numbers also depend on intervals age, i.e. Beaverhill Lake pools are dozen times larger than the shallower Upper Cretaceous pools. The average size of the Elk Point pools appears to be smaller, through the number of pools is large due to pinnacle reef type. Within the group of 14 largest oil pools, the 11 largest occur within Paleozoic formations. There are three important areas in Alberta accumulating oil sands which contain about $260 \,\mathrm{x}\, 10^9\,\mathrm{m}^3$ initial oil-in-place reserves. The major oil sand areas are located in the region of Athabasca, Cold Lake and Peace River and the reserves mostly occur in the Upper and Lower Mannville and some amounts in the Devonian Grosmont. Since 2005, the number of projects related to the oil sands exploration and exploitation rapidly increased gathering the total capital expenditures of about $125 billion. Canada is a leading country in production and exporting of natural gas with large quantities coming from the WCSB. The overall reserves within the WCSB are estimated at $4000\,\mathrm{km}^3$ of natural gas whose peak production occurred in 2001 at around $0.45\,\mathrm{km}^3$ per day. However, most of the discovered gas pools have been depleted and new discoveries give less gas with each new well indicating decline in production (Davidson & Elsner, 2005). The large portion of gas comes from the four Devonian intervals and five Cretaceous, 23.0 and 48.1 % of marketable gas reserves respectively. The WCSB contains almost the whole of Canadas coal resources ranging in age from Early Carboniferous (Mississippian) to Paleocene (Cameron & Smith, 1991). Large quantities of the coal resources found in Alberta are lignite to semianthracite. These flat-lying beds reach the average thickness of about a dozen meters and due to low sulfur contents and moderate ash level are mined for power generation purpose or coking feedstocks.

**Geothermal analysis**

The geothermal analysis in sedimentary basins is defined by mutual interactions between different heat sources and its transport methods towards the surface (Chap-

man & Rybach, 1985). In the WCSB such an analysis is based on three different methods showing a high degree of data correlation. These methods are: temperature distribution recorded in the wells reaching the basement; content of isotopes within the rocks and its radiogenic heat production; and thickness of sedimentary layers covering the basement outcrop (Majorowicz & Jessop, 1981). The highest correlation degree is obtained between radiogenic components and borehole data analysis, even for the areas with limited data availability as well as for small-scale anomalies.

The areal distribution of the geothermal gradient varies across the WCSB, reaching its maximum value of about 45 °C/km in the northeastern part and less than 20 °C/km in the southern part of basin. Similar to the geothermal gradient, a heat-flow distribution in the basement reach a maximum value of 80 mW/m$^2$ in the northern Alberta and Northwest Territories to the 40 mW/m$^2$ in southern Alberta (Bachu, 1993; Jones *et al.*, 1985). There is also a strong correlation between temperature recorded in the bottom of wells (BHT) with the thickness of sedimentary overburden giving the highest recorded temperatures of about 160 °C next to the thrust and fold belt zones. These high values can not be explained by topographically related features from the basement, which express in high radiogenic heat production. As suggested byMajorowicz *et al.* (1985) and Bachu (1993) these high temperature effects are additionally enhanced by the flow of formation water.

## 4.2 Experiment and data

In the 1990s, about 2000 km of active seismic reflection lines were acquired within the work of the multidisciplinary geoscientific project named Lithoprobe (Eaton *et al.*, 1995). Across the province of Alberta, surveys were carried out along three separate transects extending from Fort St. John in British Columbia southeastward to the southern border of Alberta province. These were the Peace River Arch industry seismic experiment (PRAISE), the Central Alberta Transects (CAT) and the southern Alberta Lithoprobe transect (SALT). Taken together, all three transects characterize the regional structure and tectonic activities of the Western Canada Sedimentary Basin (WCSB) over the last 500 million years (Hope *et al.*, 1999) and provide valuable information of sedimentary strata within the center of the WCSB.

**Table 4.1:** Acquisition parameters of the LITHOPROBE Central Alberta Transect survey (see the location of lines on fig. 4.1)) performed by Veritas Geophysical Ltd. of Calgary in July, 1992 (after Eaton *et al.* (1995))

| SURVEY PARAMETERS | |
|---|---|
| Source | Vibroseis©, 4 vibrators over 50 m |
| Source interval | 100 m |
| Sweep | linear, 10–56 Hz, 8 sweeps per VP |
| Sweep length | 14 s |
| Receiver group interval | 50 m |
| Receiver group spacing | 9 over 42 m |
| Recording system | I/O System One |
| Record length | 18 s |
| Sampling rate | 4 ms |
| Spread | asymmetric split–spread |
| | 3000 – 150 – VP – 150 – 9000 m |
| Coverage | 60 |

The Lithoprobe seismic reflection data from the Central Alberta Transects are composed of 10 seismic profiles with a total length of 520 km. The localization of the profiles extends from 60 km west of Edmonton, eastward to the Alberta-Saskatchewan border (Figure 4.1). Data were acquired in the summer of 1992 by Veritas Geophysical Ltd, mainly along the road grid of the Alberta province with overshooting at line intersections. Lines 2, 5, 7 and 9 were oriented in east-west direction, whereas Lines 3, 4, 6, and 8 were predominantly running north-south. The line location and their orientation was chosen to cross the basement domain borders perpendicular to the strike (Ross *et al.*, 1991).

Acquisition parameters originally focused to highlight features of deep crystalline basement and were described in details by Eaton *et al.* (1995). The research target of the Lithoprobe project required the application of a field geometry different from the common industry standards, i.e. the source signal was acquired from a group of four larger then usual Vibroseis units spaced at 100 m to ensure its penetration at greater depths, quite low frequency range of the sweep (5-56 Hz) to avoid too fast signal attenuation, larger spacing of receivers groups (50 m) placed in half of source position and very long offsets - up to 12 km obtained by the use of 240 channels recording system. Acquisition geometry was a combination of asymmetric split–spread with short offset up to 3000 m and long offset up to 9000 m. The main acquisition parameters are presented in Table 4.1.

In general, the quality of recorded seismic data was good along all lines with strong continuous reflections from the sedimentary layers (Figure 4.3) as well as all three

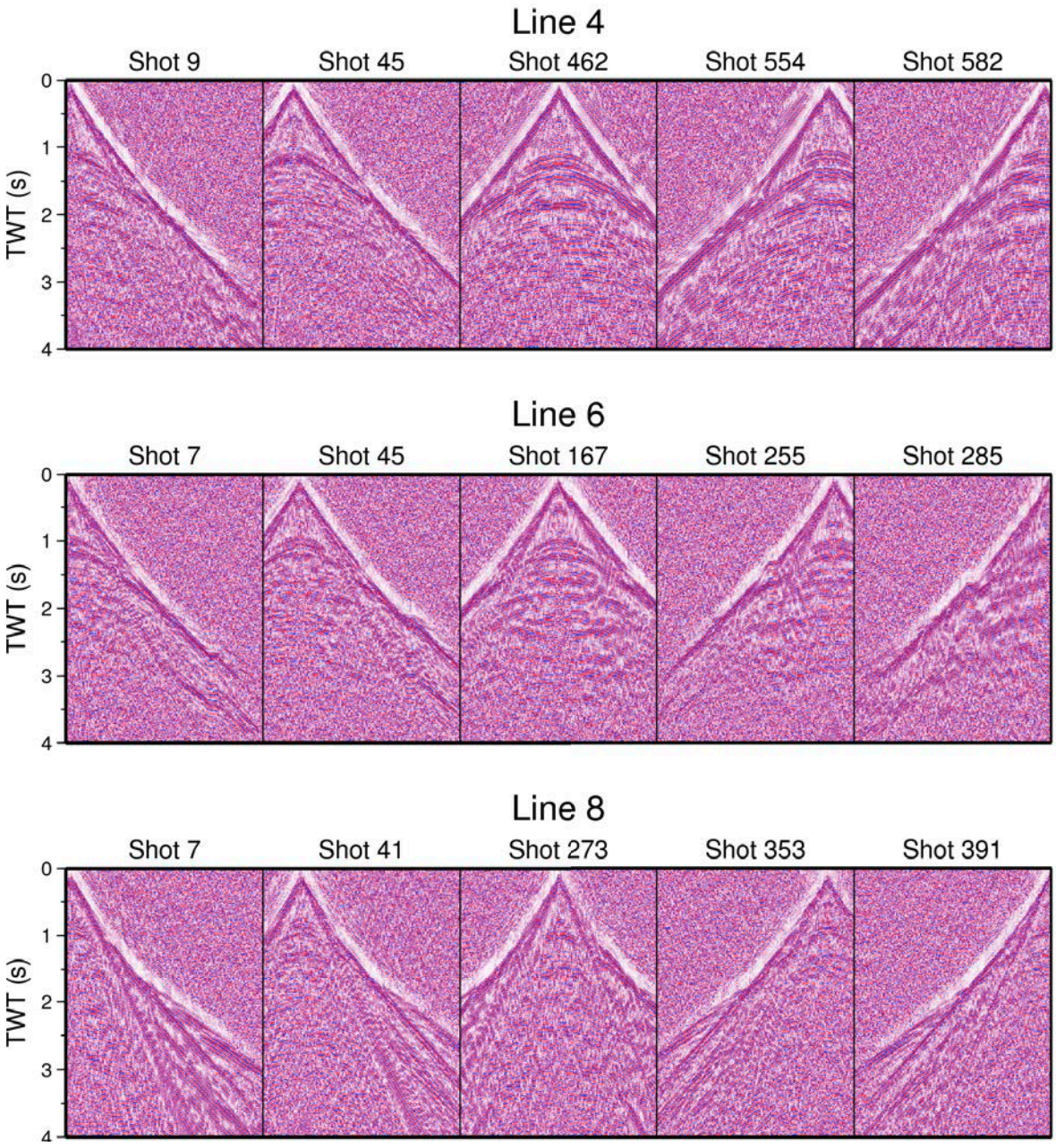


**Figure 4.3:** Common-shot gathers from the Central Alberta Transect recorded on line 4, 6 and 8 (see the line locations on fig. 4.1). Each diagram shows five shots fired at different location along the line. . First arrivals with reflection events are clearly visible on all shots. Additionally all shots from line 8 contain strong surface waves. An AGC of 500 ms and an Ormsby bandpass filter 5-10-56-75 Hz were applied to increase image quality.

transects throughout the crust due to 18 s of data recording (Hope et al., 1999). Sedimentary succession and its interface with the basement surface were recorded within the first 2 seconds of TWT as shown later in section 4.3. Additionally, the real-time noise elimination and precise monitoring of vibrator synchronization allowed to recover much more high quality seismic data.

The presence of high lateral reflectivity from sedimentary layers largely helped to compute residual static correction and assisted in the calculation of crustal velocities Eaton *et al.* (1995). A noticeable loss of reflectivity was observed at the first half of Line 1, probably caused by too high power energy output from the vibroseis trucks. Due to low quality of recordings along Line 1 and too complicated crooked geometry along Line 10, these two lines were excluded from the further CMP and CRS processing.

## 4.3 CMP Processing

The Central Alberta Transect 2D reflection seismic project was recorded in 1992 by Vertias Geophysical Ltd. and then processed by Pulsonic Geophysical Ltd. of Calgary. The original data processing scheme has been presented by Eaton *et al.* (1995) and the major steps are shown in Table 4.4. Originally, the Lithoprobe reflection project aimed at imaging the deep part of the crust due to 18 s of data recording which allowed to penetrate the subsurface down to 40 km. Since the target horizons presented in this study are located between 3 and 4 km depth, the data processing scheme demonstrated here slightly differs from that performed by the contractor and will concentrate on the first 2.5 s of TWT.

Since 1995, when first Lithoprobe results have been published, several new acquisition and processing innovations have become available to improve the data quality. Beside migration algorithms, dominant flows of the seismic data processing at that time focused on noise attenuation and removal of multiple reflections and application of *f-k* filtering. The processed data demonstrated here slightly differ from that described in Eaton *et al.* (1995), mostly by the application of other than original deconvolution method and filtration method focused to highlight the reflection events from the first 2.5 s TWT. All further processing steps have been carried out with PROMAX © software.

The original records provided by Natural Resources Canada (NRC) were stored in SEG-P format. As part of this thesis noise test files as well as corrupted shots

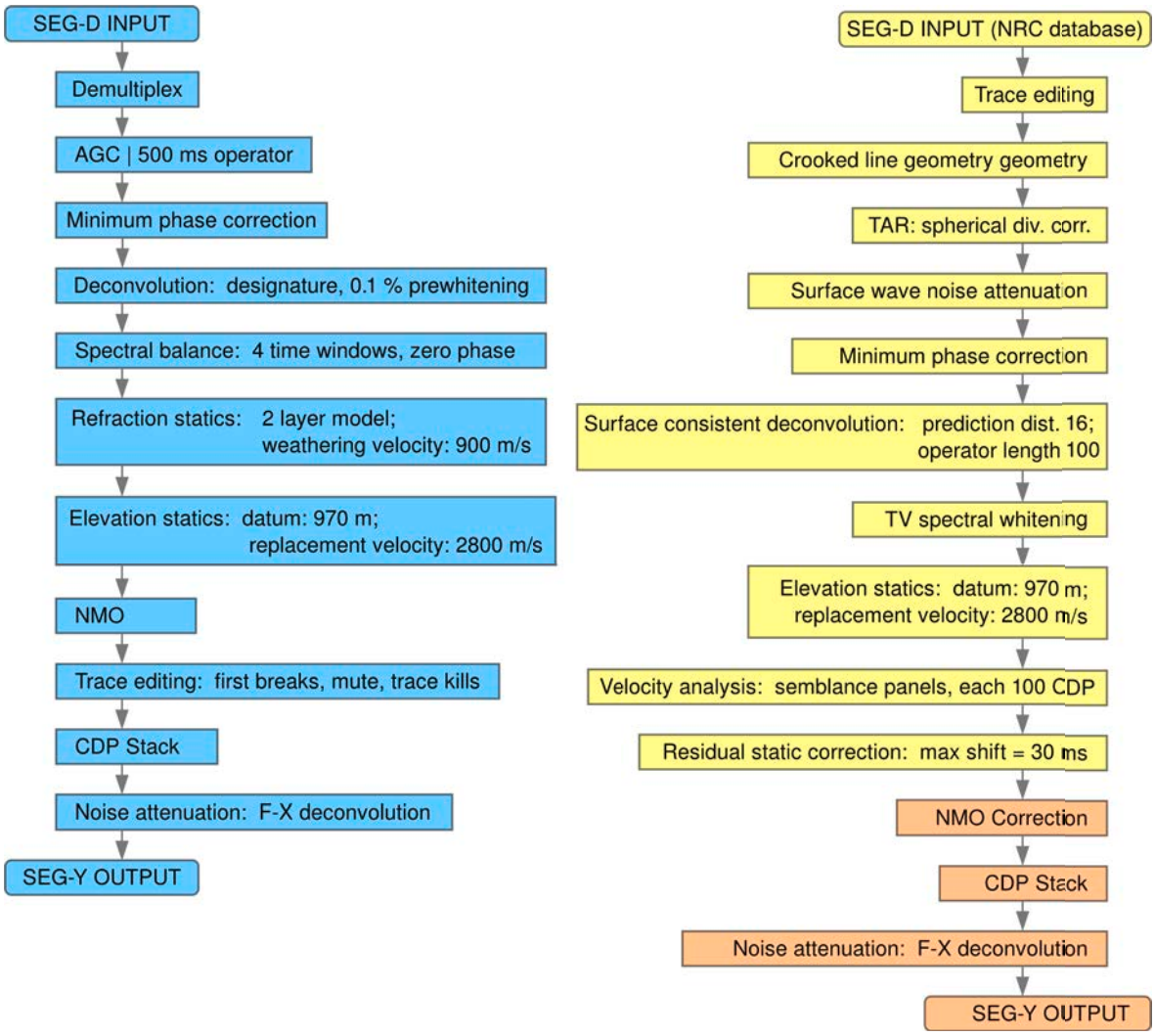


**Figure 4.4:** Comparison of the processing parameters applied to the LITHOPROBE Central Alberta Transect surveys (see line locations on fig. 4.1). Left column presents the processing sequence originally performed by Pulsonic Geophysical Ltd. in 1993 (after Eaton *et al.* (1995)). Right side shows processing flow performed for the purpose of this thesis. The steps indicated with orange color were excluded from the CRS flow as the input data can not contain CMP correction.

due to problems with cable or bad boxes have been removed. Also shots with higher noise level due to heavy rain during recording time or presence of underground springs which caused malfunction of the large receiver groups have been removed. After the data have been manually reviewed, based on the information obtained from headers and operator's field notes, the geometry was assigned to the traces. To meet the

comparison criteria the CMP bin spacing was 20 m equal to the half-distance between receivers.

The near surface disorders and other variation of the amplitude along the line were corrected by the use of amplitude gain control (AGC) with one window gate of 0.5 s length. A single band-pass filter with corner frequencies of 5-10-56-75 Hz was chosen after several tests and applied to each input trace. The original filter used by Pulsonic with corner frequencies of 5-10-60-64 Hz had a too small high-cut ramp suppressing reflections with smaller energy and causing stronger ripples effect in the wavelet. Also there was no reason to apply multi-window balancing or scaling as the contractor did, since the processing was performed up to 3.0 s time only.

In order to carry out the deconvolution process properly, data sets ordered in shot domain were convolved with the minimum phase filter obtained by an autocorrelation of a sweep signal. This was necessary due to the nature of the signal generated by the vibrator source which is not an impulse source. Later on, a few shot gathers have been selected to determine the proper time window for the application of the deconvolution filer.

The deconvolution approach applied here was a surface consistent type Levin (1989), a method mostly used in land seismic data processing since marine environment does not guarantee a permanent position of geophones. With this method all traces from the same source, receiver and CMP or offset location will have the same operator applied. Several parameters, as the length of the operator, the prediction distance and the percentage of white noise have been tested. As shown on Fig. 4.5b, prediction distance of 16 ms and 100 ms operator length gave the best effect both on single shots and the final stacks.

After deconvolution was completed, the data sets were designated for static correction. The elevation along CAT profiles varies significantly therefore correcting for static shifts can make a significant difference in the quality of a stacked image. In consequence, the floating datum was selected as the reference instead of a fixed datum. The floating datum was determined by smoothing of existing elevation and corrected to the final datum prior to stack. The replacement velocity was the same as used originally by contractor and varied slightly around 2800 m/s. Figure 4.6 shows the selected processing steps applied to a typical shot gather, before the data sets were sorted to the CMP domain.

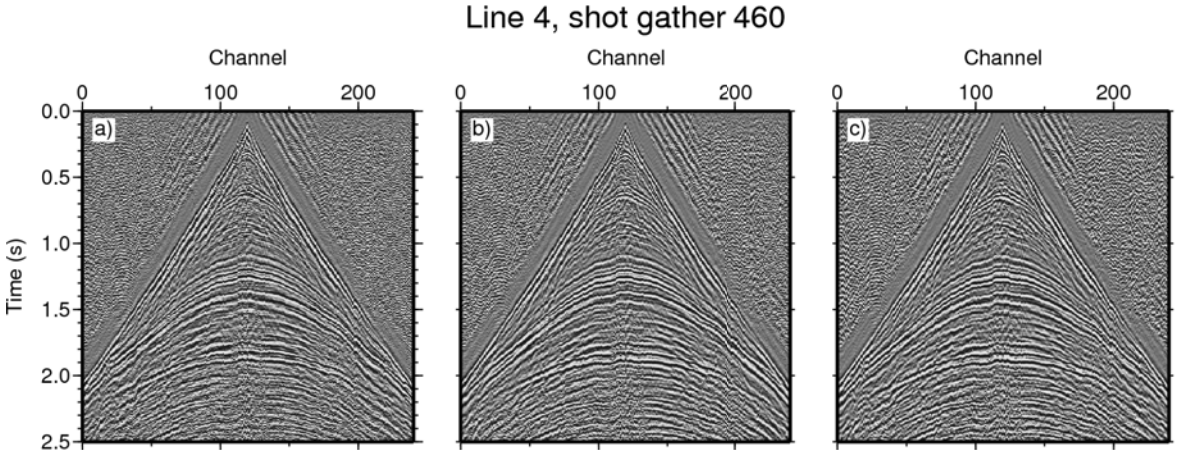


**Figure 4.5:** Surface consistent deconvolution tests were performed on shot 460 from Line 4 with different operator length as a) 40 ms, b) 100 ms, c) 200 ms. The test with 16 ms prediction distance and 100 ms operator length provided the best effect of preserved signals from all sedimentary layers and suppressed short period multiples. An AGC and band-pass filtering were applied for presentation purpose.

Since the processing of the data set was focused on the sedimentary succession, there was no need to divide the velocity analysis into two time windows as originally due to deep penetration (Eaton *et al.*, 1995). The semblance velocity panels were used to build a velocity model based on coherency criteria (Taner & Koehler, 1969). To obtain best results low fold part of the data was omitted and velocity analysis was performed with steps of 100 CMP along line. The supergathers consisting of 7 neighborhoods provided sufficient coherency and offset spectrum to determine accurate velocity model. Thus the obtained velocity model was applied to each CMP gather to make the moveout correction available.

To remove the effect of near-surface velocity variations that usually appears as small dynamic distortion a residual static correction was performed to minimize this effect. The Promax© tool, called Maximum Power Autostatics, is based on the method developed by Ronen & Claerbout (1985). It involves CMP sorting and the application of normal moveout correction to the input data sets. The key point to remove dip component from neighborhood CMPs is to provide a maximum allowed static shift value and picked horizon(s) centered on the time window containing the highest coherency signals. Then, a pilot trace for a reference CMP is cross-correlated with the trace extracted iteratively from smashed CMPs, where a maximum static shift value

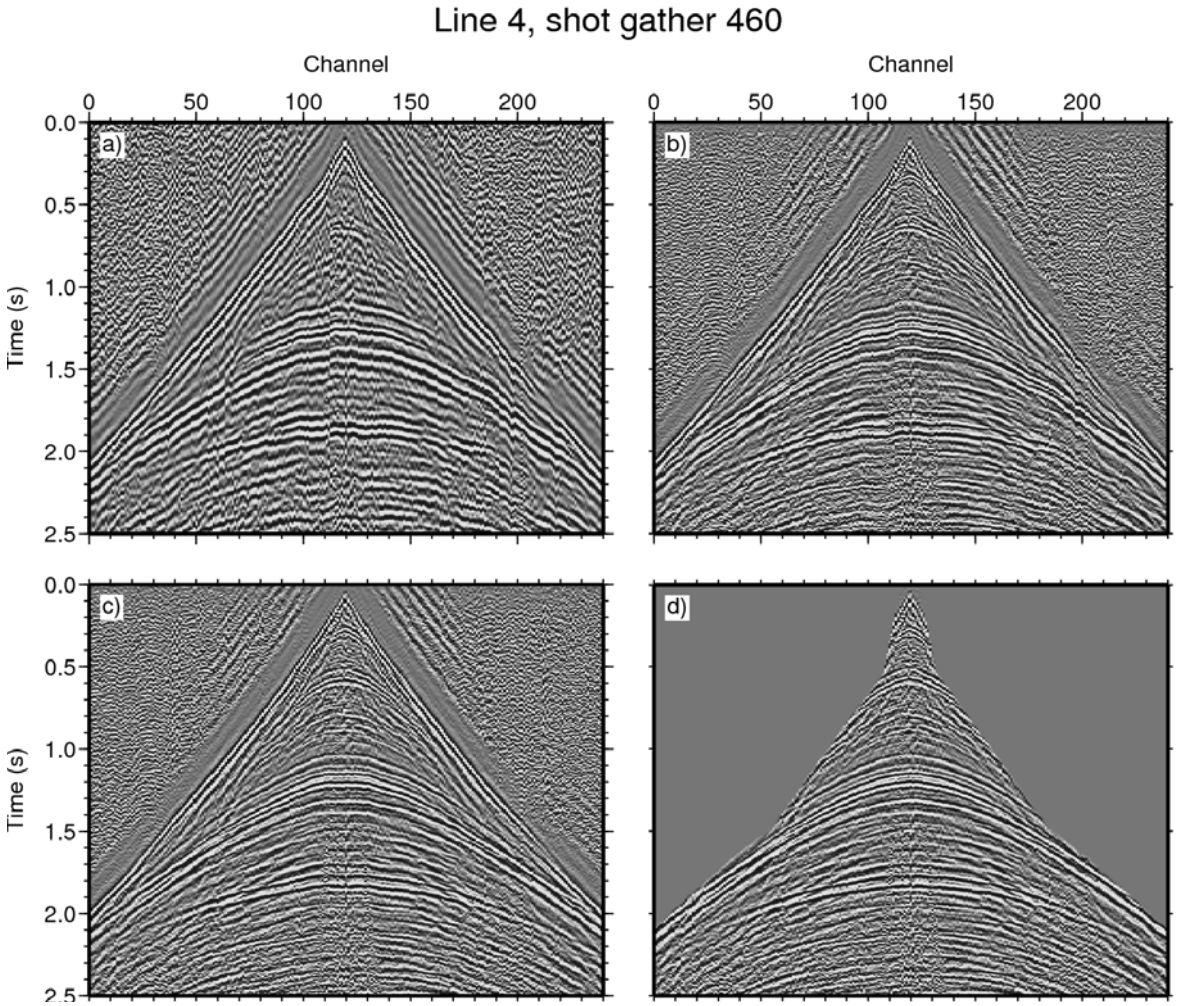


**Figure 4.6:** Results of the application of selected processing steps performed on typical shot gathers. The full processing flow as described in Table 4.4 was performed on shot gather 460 from Line 4 (see Fig. 4.3). For presentation purpose data were processed by the application of AGC and band-pass filter, a) raw data, b) deconvolution, c) statics correction, d) muting and residual static correction.

is specified. That obtained cross-correlation is a measure of stack power and is applied to the shot and receiver position of this trace. Here the maximum value of static shift was set to 30 ms whereas the horizon selected for smashing was Pika for all lines.

As the last step before stacking, the top muting was carried out to remove first arrivals and overstretched parts of the trace due to the CMP correction. Hand-picked mutes tested on three shot gather was sufficient to extrapolatefor the remaining shots. After the data set were stacked by the summation of traces with the use of the mean

stack algorithm, F-X deconvolution was applied to enhance lateral resolution of the reflection events and to restore high frequency attenuated during CMP correction and stacking. Before exporting to SEG-Y format an automatic gain control scaling with a window length of 500 ms has been applied to enhance image quality.

Later on, to compile a joint section from the individual CAT profiles it was necessary to apply static corrections with a floating datum and fixed replacement velocity slightly different between lines in order to resolve significant mis-ties. The large extent of the resulting composite section enables the attribute analysis of regional reflection characteristics spanning several basement tectonic domains, as well as interregional comparisons of key structural elements in the Alberta basin.

## 4.4 CRS Processing

As mentioned in the section 3.3, the CRS processing is aimed to provide the stacking operator for each zero-offset trace sample in order to obtain a simulated zero-offset stack section. In consequence, three of the CRS kinematic attributes obtained during the processing provide additional sections and can be utilized in other techniques, i.e. NIP-wave tomography (Duveneck, 2004). These attributes bring up their potential only where associated with the reflection event highlighted by a high coherence value. Thus, the coherency section is the first evaluator of reflection event occurrence and reliability of the obtained CRS attributes. The quality of coherency section depends on the number of contributing traces and S/N ratio of the event.

Since the simultaneous parameter selection is not efficient in the sense of computation time, an additional simplification steps are highly desired. In the 2D case, where three of the CRS attributes must be provided to obtain the final CRS stack such a simplification proposed by Mann *et al.* (1999) decrease the computation time significantly. As already defined by 3.7, the idea is to determine single attribute separately one after the other, under the assumption that the rest will be zeroed. As soon as the $\nu_{NMO}$ value is computed under the $\Delta\boldsymbol{\xi} = 0$ assumption it can be used to search for $\alpha$ parameter by setting $h = 0$ and $R_N = \infty$. Consequently, $R_N$ is obtained with $h = 0$ assumption which leads to the last step - an optimization of the all CRS attributes. As the alternative to local optimization an event consistent smoothing method is applied to determine a proper parameter values.

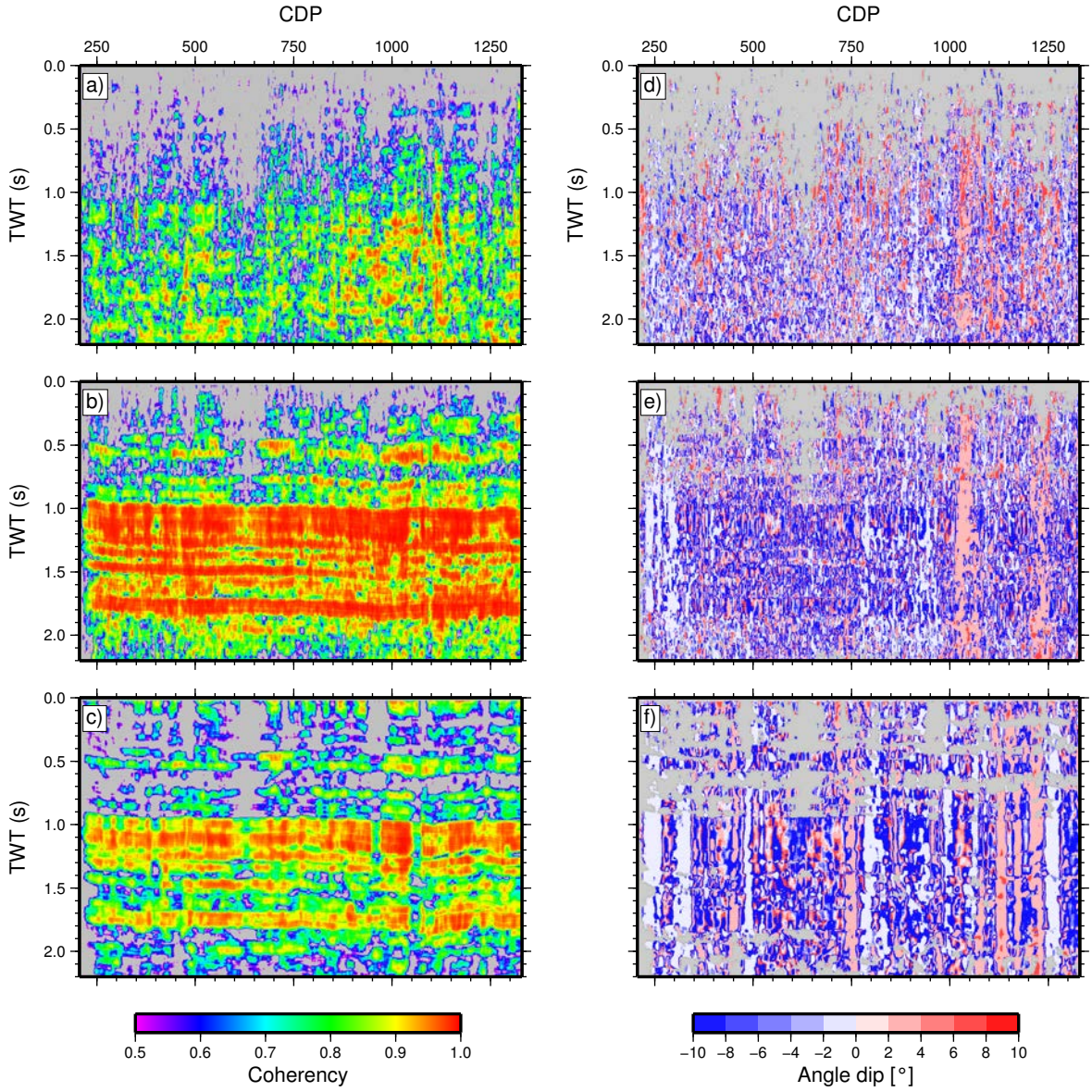


**Figure 4.7:** Results of parameter tests applied to the CRS data set from Line 4. Images show the consecutive steps in CRS stack data processing applied to the CMP sorted dataset along Line 4. (a) to (c) Coherency section , (d) to (f) emergency angle $\alpha$ search results. Low coherency values are masked in gray. Further description is given in the text below.

The travel time approximations defined by equation 3.9 are dependent on distance in the midpoint and offset directions and generally, its quality decrease with distance from the zero-offset location. Thus, the proper aperture selection, both in midpoint and

offset direction, applied during the parameter search, needs to be selected with special attention to obtain good quality results. Also, if the main aim is the determination of CRS attributes for further applications needs, i.e. tomography, controlling of spread-length-bias effect has to be undertaken with special care. For example when a large apertures is selected, the second order approximation may fit to the reflection not at the considered zero-offset location (see Fig. 4.7c and f). While too small, apertures will decrease the resolution and lead to inefficient number of parameters to determine the CRS attribute (see Fig. 4.7a and d). The efficient aperture selection mainly depends on differences between the traveltime moveout function and its theoretical hyperbolic shape. The larger the difference the less reliable is the CRS attribute determination.

The search for CRS parameters is performed on the preprocessed CMP data sets without normal moveout correction, as mentioned in CMP processing flow description (see Fig. 4.4). In order to make the full imaging available different apertures in offsets and midpoint direction were tested. During the first phase, the aperture estimation based on the test performed along selected shot gather with CMP corrected reflection events. These kind of tests make use of large number of traces increasing the coherency analysis and improve the spread-length bias effect. After several tests, the offset aperture was determined between 300 m for near surface times to 2500 m at 3.0 s TWT (see Fig. 4.7c) and interpolated linearly in between. The midpoint aperture was determined between 75 m for near surface times to 300 m at 3.0 s TWT. Figure 4.7 and 4.8 show example aperture search performed on Line 4.

The ZO section acquired during CMP processing is used as the input model in order to perform emergency angle $\alpha$ search. The emergency angle section presented on Fig. 4.7e shows gentle dipping to the south (see Fig. 4.1 for line orientation) which does not exceed 10 ° in agreement with the general tendency of the local geological framework that is proved by high coherency values 4.7b along the package of reflection events. This also indicates that the subsurface structure can be treated as 1D medium where the lateral velocity variations are expected to be relatively small.

Further steps of the CRS processing incorporate the constrains of the ZO searches that are more connected to the geological condition of the sedimentary basin.

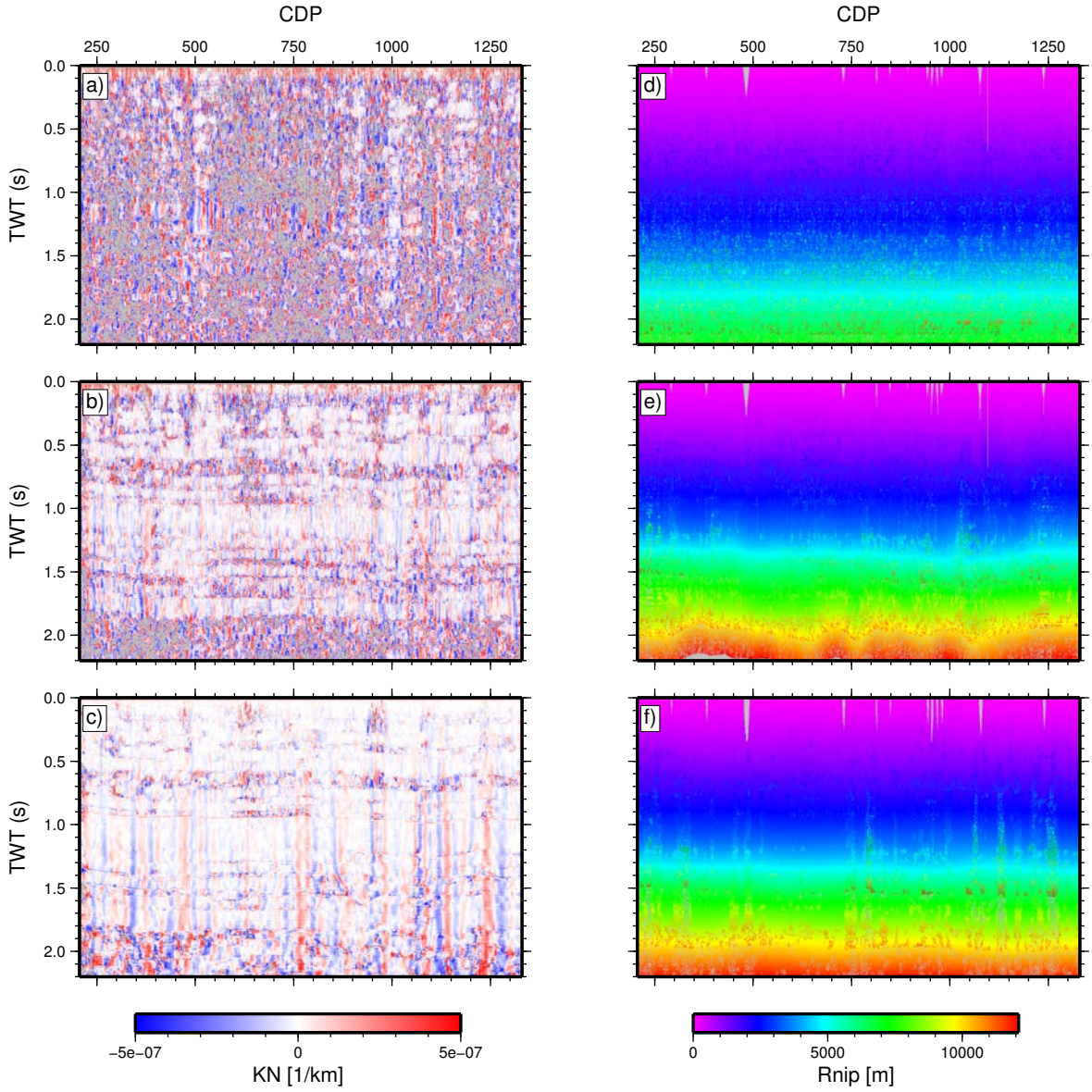


**Figure 4.8:** Results of parameter tests applied to the CRS data set from Line 4 (a) to (c) reciprocal value of normal ray $K_N$=$R_N^{-1}$, (d) to (f) radius of $R_{NIP}$ wave search results. Low coherency values are masked in gray.

## 4.5 Results of stacking

The composite section of all CAT lines was originally compiled by Eaton *et al.* (1995). It presents the sedimentary succession which overlays the upper crustal basement unconformable. The geological regime in the area covered by transects does not appear as

much complicated as regions influenced by strong tectonic movements. The structures like unit onlaps, buildups, pull-ups, drapes or gradual thinning/thickening were already indicated by Edwards & Brown (1999) or Dietrich (1999) and are mostly developed in close vicinity to the reef formations. Although carbonate platforms are considered as the potential geothermal reservoir (von Hartmann *et al.*, 2012) however due to low permeability the application of the EGS technology is required for its economic utilization (Moeck, 2014). Actually, these are not the subject of further geothermal exploration in the Alberta basin therefore I will not investigate differences between CMP and CRS stacked images with respect to these geological formations.

Eaton *et al.* (1995) has distinguished two major crustal-scale zones based on deep reflectivity characteristics, however, its influence on the sedimentary cover is still discussed (Dietrich, 1999; Edwards & Brown, 1999). The first half of the transect, can be associated with southeast-verging thrust formations whereas the remaining part is characterized by a constant inclination reflectivity to the southeast, interpreted as a crustal-scale belt with a reversal in vergence thrust formations referred to the East Alberta Orogen. Generally, the top of basement reflection (TBR) appears as a gently southwest-dipping undulating surface. Its contact with the sedimentary outcrop is indicated by the strong amplitude positive reflection (peak) occurring between 1.35 and 1.8 s TWT. Together with shallower reflections of the lower Paleozoic formations can be traced for most of the transect length. On the other side crustal reflections are characterized by a lower S/N ratio and presence of multiples recorded down to 4.0 s TWT.

Considering a good quality of prestack data sets from each line and therefore a good quality of CMP stacked section, there were not many additional reflection events resolved by the CRS approach. Stacking results represent a typical sedimentary environment in the form of gently dipping flat reflectors undisturbed by tectonic forces. Nevertheless, there are still some structural features that might be better visualized as the CRS processing of the Lithoprobe data was performed with emphasis on the geological constraints. Generally, the CRS stacked section presents more improved images and higher overall S/N quality of reflection events in comparison to the CMP stacked counterparts. Such an improvement is also visible on the resultant CRS attribute sections (see chapter 4.4), where i.e. high coherency values were acquired along reflection events, thus, indicating reliably determined CRS kinematic attributes.

Also significant improvement can be observed close to the surface, where reflections from shallow strata recorded at 0.2 s are better imaged by the CRS stack due to increased continuity of the recorded reflections. On the other side, insufficient number of traces within the CMP counterpart makes the identification of shallow horizons unclear. A sample set of final results of CMP and CRS stacked sections from the Central Alberta Transects are presented on figures 4.9 - 4.15.

Figure 4.9 and figure 4.10 show images of the CMP and CRS stacked sections acquired from Line 2 and Line 3 respectively located at the beginning of the Central Alberta Transect. The overall quality presented on the CRS image is higher than obtained from the CMP counterpart. The continuity of reflection events from the lower Paleozoic formations recorded between 1.0 and 1.8 s TWT are highlighted with more details. Most of horizons obtained from CMP stack are presented noisy whereas the same reflectors imaged by the CRS stack show better continuity and can be clearly identified. Especially the reflection event located between CMP 1050 and 1250 at 1.2 s TWT along Line 2 has been resolved at higher confidence level than the CMP counterpart.

The Mesozoic succession visible above 1.0 s TWT shows similar signal characteristic on both, the CMP and CRS stacked images, and allows the horizons to be clearly identified. The partial identification of the horizon recorded at 0.9 s TWT has been improved by the CRS stack where it shows reflection events with higher S/N ratio and better continuity. Due to irregular acquisition and limited amount of available shots, traces visible between CMP 1300 and 1400 on Line 2 were not resolved sufficiently on both stack producing noisy and disturbed stacked image.

Figure 4.11 presents the stacking results obtained by the application of the CMP and the CRS technique to dataset acquired from Line 4 located at the end of the southeast-verging thrust formations. The whole sedimentary succession is horizontally arranged due to perpendicular orientation of the profile in respect to the main axis of the basin subsidence. The CMP and the CRS sections show imaged horizons consisting of similar S/N ratio and similar reflection continuity. The Precambrian basement formation has been imaged with a weak amplitude reflection events recorded at 1.8 s TWT, while the Pika horizon at 1.6 s TWT. The reflection event from the basement which is observed along Line 4 (some influence is also visible on neighborhood Lines 3 and 5) shows a 'seismic anomaly' which is associated with precambrian Rimbey domain and the high amplitude Middle Cambrian reflection event. Initially it was defined by Eaton *et al.*

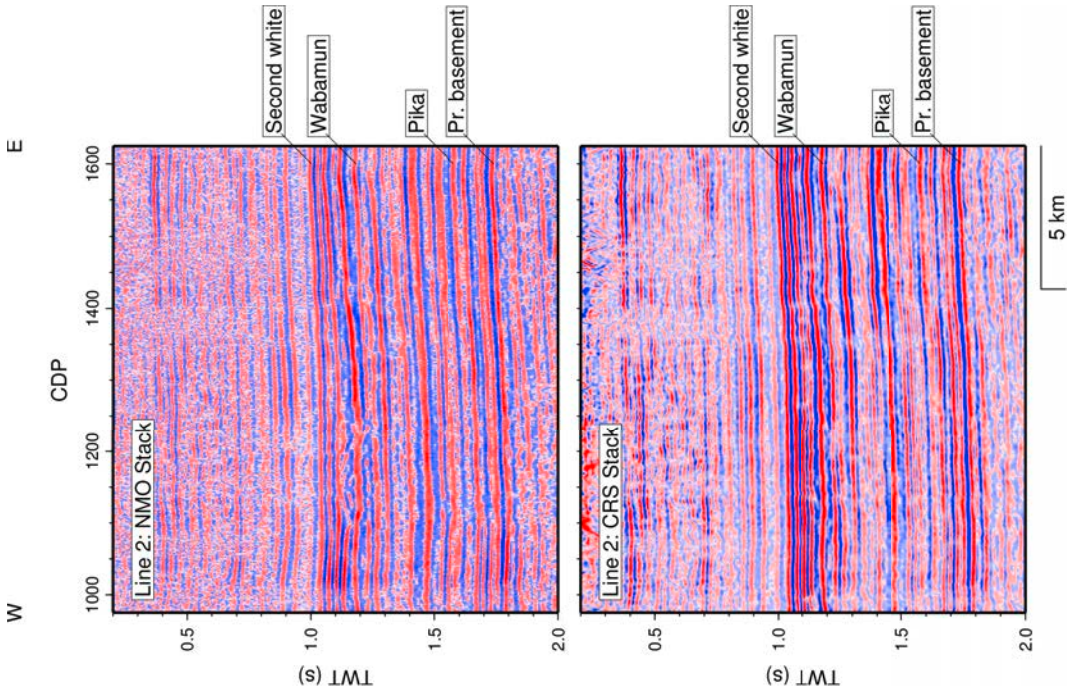


**Figure 4.9:** Seismic time section of Central Alberta Transect Line 2, processed with CMP (top) and CRS (bottom) method. The CRS image shows reflection events with higher S/N ratio and better continuity compared to the CMP stack section.

(1995) as 'basement precursor' and the authors addressed this feature to 'mineralized or diagenetically altered zone'. Later on, based on well data correlation, Dietrich (1999) indicated another concept, which identify the seismic anomaly as 'seismic-stratygraphic signature' associated with the Middle Cambrian lithofacies variations and wavelet tuning effect between carbonates and sandstone formations.

Figure 4.12 shows images of the CMP and the CRS stacked sections acquired from Line 5 located in the center of Central Alberta Transect. Gentle lowering of horizons recorded between CMP 600 and 800 may suggest structural interactions between two deeper crustal units that forms transition between Rimbey High and Lacombe domain as suggested by Dietrich (1999). The Rimbey-Midowbrook reef structure can be identified between 400 and 600 CMP at 1.3 s TWT, whereas the Basement reflection events are recorded at 1.8 s TWT.

The stacking comparison of the Central Alberta transect Line 6 has been shown on Figure 4.13. Similar to Line 4, all formations within a given sedimentary succession are horizontally arranged due to perpendicular orientation of the seismic profile to the main

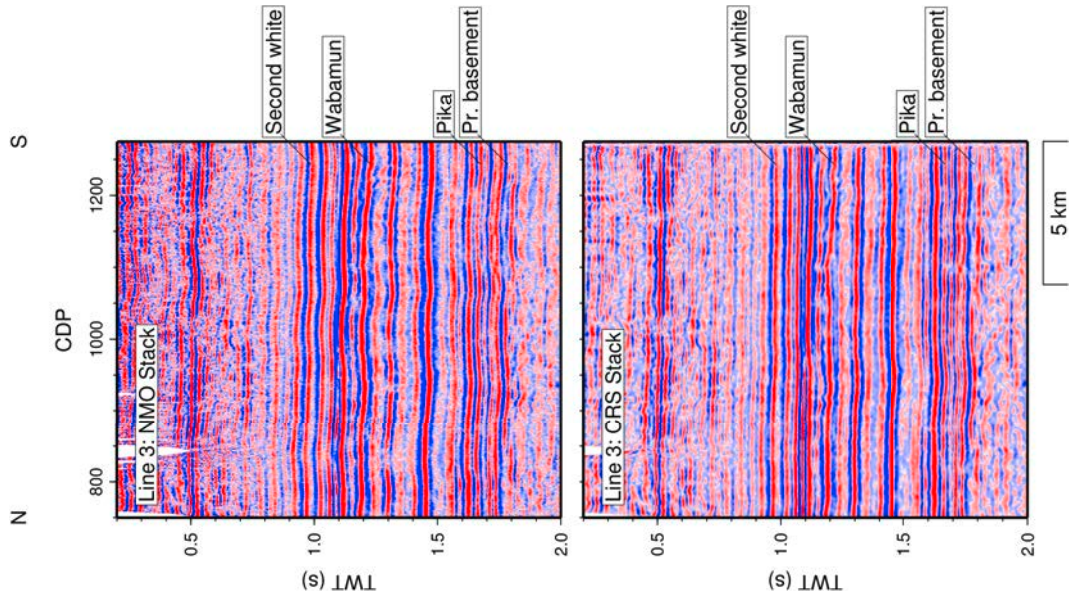


**Figure 4.10:** Seismic time section of Central Alberta Transect Line 3, processed with CMP (top) and CRS (bottom) method. The CMP and the CRS stacked sections show similar quality image.

subsidence axis of the Alberta Basin. The deepest Basement formation is recorded at 1.7 s TWT, whereas the Second White Speckled at 0.9 s TWT. Missing traces in the CRS image are caused by the crooked geometry layout.

Beside the general quality improvement, a better continuity and clearly visible reflectors are dominate on the CRS image. Acquired horizons allowed to be imaged more precisely within tested apertures, thus ensure reliable picking of target horizons. Interesting results were acquired between 0.45-0.65 s TWT at the beginning of profile where complicated structural image of the shallow succession could be interpreted by a violent sedimentation or local tectonic processes.

Figure 4.14 shows the comparison between the CMP and the CRS stacked image from the Line 8 located at the end of Central Alberta Transect. The overall quality of both processed sections are similar, however, there are some details less visible in the CMP stack section. Reflection events of Pika horizon recorded at 1.35 s TWT between CMP 400 and 500 show better continuity and are clearly identified. Also large package of reflections between CMP 550 and 700 at 1.0 to 1.25 s TWT disturbed due the higher located pull-up are better resolved.

The final part of Central Alberta Transect presented in Figure 4.15 shows stacked

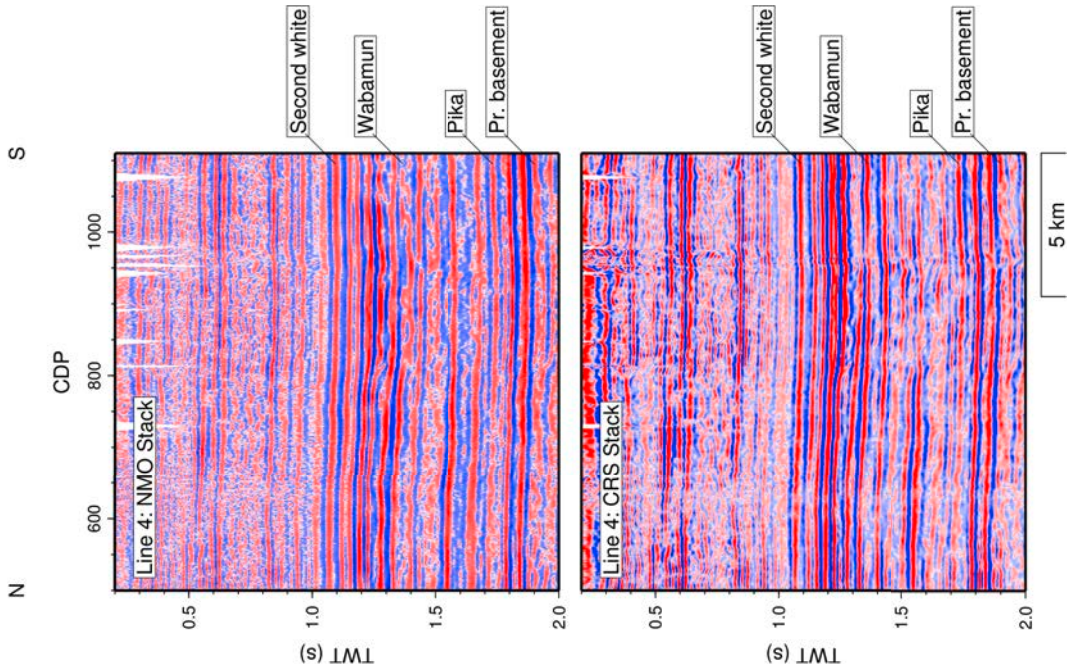


**Figure 4.11:** Seismic time section of Central Alberta Transect Line 4, processed with CMP (top) and CRS (bottom) method. Basement reflection events, visible as weak 'seismic anomaly' are recorded at 1.8 s TWT.

image of the CMP and the CRS method acquired from Line 9. The overall signal improvement and higher S/N ratio are presented on both images. The interface between basement and the sedimentary succession, recorded from CMP 400 shows strong reduction in amplitude associated with lithological parameters like high porosity of Cambrian formations lying over Precambrian rocks. It is worth to note the general tendency of increased lifting of the whole sedimentation complex as well as the characteristic pull-up recorded at the beginning of the section spanned through the whole complex. Also reflections package between CMP 850 and 900 at disturbed due to the acquisition and limited amount of available shots are better resolved and are clearly identified on CRS counterpart.

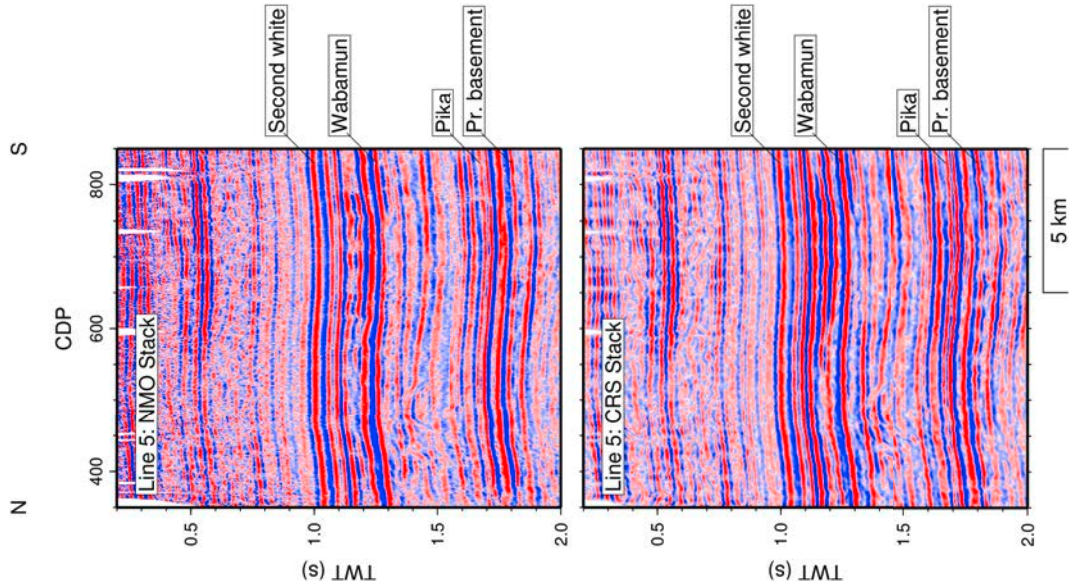


**Figure 4.12:** Seismic time section of Central Alberta Transect Line 5, processed with CMP (top) and CRS (bottom) method. Basement reflection events are recorded at 1.8 s TWT.

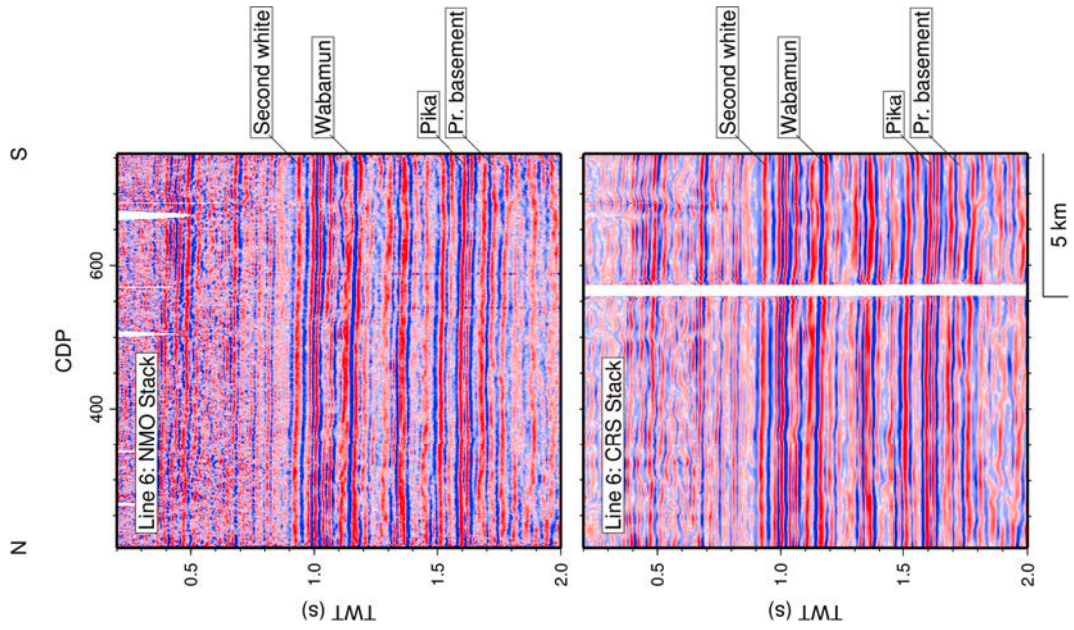


**Figure 4.13:** Seismic time section of Central Alberta Transect Line 6, processed with CMP (top) and CRS (bottom) method. The gap from the irregular acquisition geometry is filled out with data.

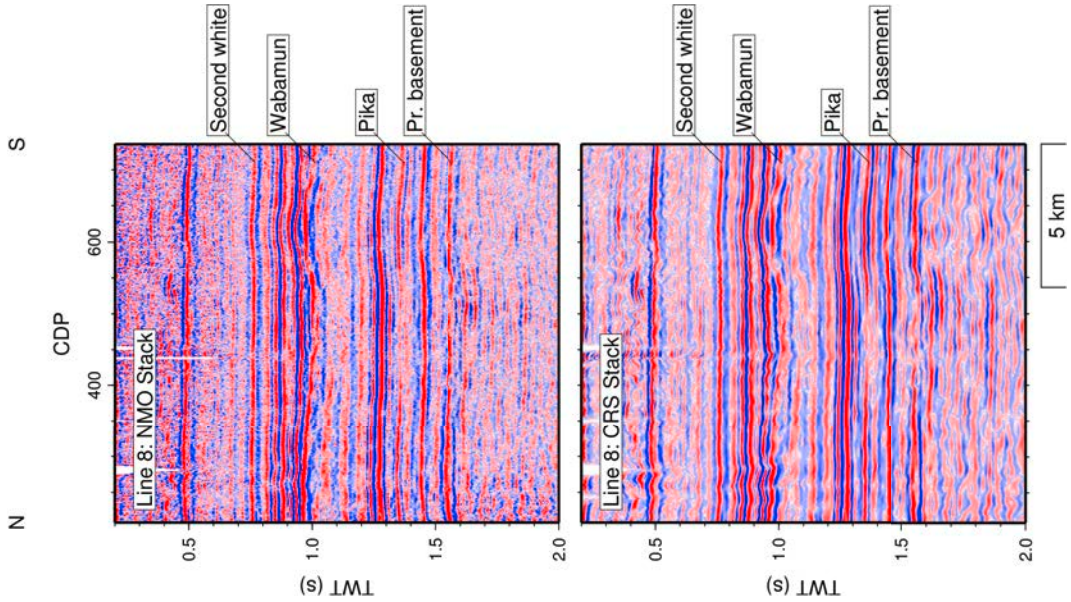


**Figure 4.14:** Seismic time section of Central Alberta Transect Line 8, processed with CMP (top) and CRS (bottom) method with similar overall signal improvement. Basement reflection events are recorded at 1.55 s TWT.

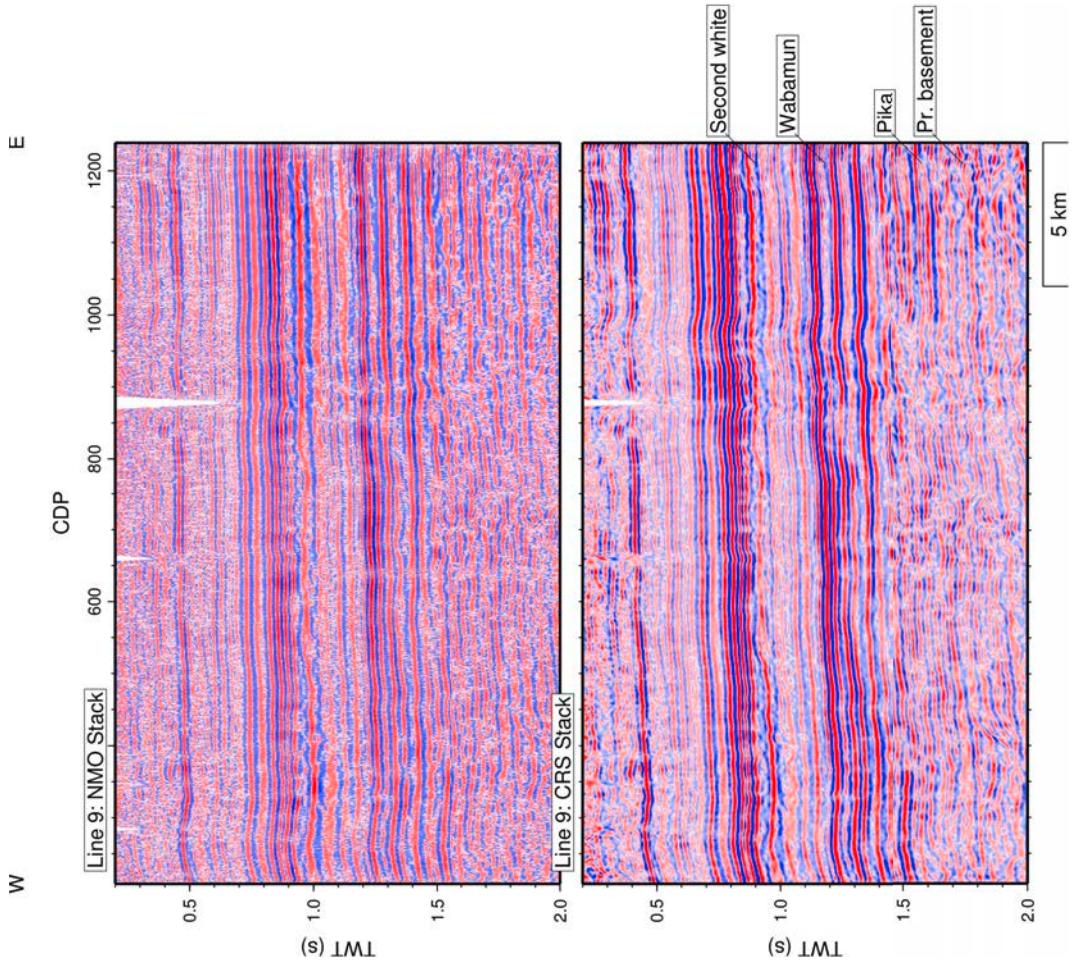


**Figure 4.15:** Seismic time section of Central Alberta Transect line 9, processed with CMP (top) and CRS (bottom) method. The termination characteristics of basement reflections are recorded at 1.4 s TWT.

## 4.6 Analysis of seismic signal attributes

The composite section of about 500 km length assembled from a 2D seismic lines and acquired within the Lithoprobe project (Eaton *et al.*, 1995) were used to facilitate differentiation of structural and tectonic units that spans over Western Canada Sedimentary Basin. In the previous chapter, Central Alberta Transect line's of the Lithoprobe project, serve as the input data to perform comparison between CMP and the CRS stack. Here, I used the resultant stack sections in order to calculate seismic trace attribute acquired along specific horizons and represented by attributes of RMS amplitude and instantaneous frequency. Both stack composite sections as well as the attributes image provide valuable information and can be used to show the interactions between the crystaline basement and sedimentary strata of the Paleozoic succession. While the reflection seismic image based on CRS stack allowed the structural identification of the horizon more clear, the seismic attribute analysis along the horizon obtained from that stack offer the possibility to distinguish the tectonic domains with higher order of confidence.

Seismic attributes were calculated to indicate the variations in lithology and thickness of the stratigraphic units that build the sedimentary package above the basement reflection event. Additionally, attributes were used to determine in more detail the location of lithofacies transition, structural features such as faults, alignments, lithological edges etc. visible between basement and sedimentary layers contact or directly within sedimentary formations. These structures were depicted in figure 6.3 and although their structural manifestation were presented on the seismic crosss-section however its representation in the form of seismic attribute also plays significant role, in geothermal exploration especially.

I used RMS amplitude and instantaneous frequency attributes as they are particularly useful for reservoir analysis within the basin environment. Both attributes belong to the primary group of seismic trace attributes and additionally may serve as the background for many others sophisticated or sometimes redundant attributes (Barnes, 2007; Taner, 2001). The RMS amplitude is computed as reflectivity within time window and can be treated as hydrocarbon or facies changes discriminator (Hammond, 1974). The higher values can also indicate intensive compaction of sediments due to a direct relationship with reflectivity (Chopra & Marfurt, 2011; Yilmaz, 2001). The instantaneous frequency attribute belongs to the group of instantaneous attributes that are derived from Hilbert transformation of the seismic trace and by definition is time

derivative of instantaneous phase (Taner *et al.*, 1979). It is commonly used in seismic data interpretation where can be used to perform a detailed assessment of reservoir lithology and its thickness variation (Barnes, 2001; Chopra & Marfurt, 2005; Zeng, 1991).

In order to fulfill an equal comparison criteria, all seismic lines from the the CAT transect were prepared based upon the same processing flow (see Fig. 4.4). The only differences were static corrections, which depend upon the elevation but did not influence the results of the attribute processing. That prepared datases, both CMP as well as the CRS, were ready for selection target horizons. The Promax© software offers the possibility of picking that can be performed directly on the screen where picks can be selected by hand or automatically with snapping option to peak or trough of the signal. I used automatic picking by the selection of peak centers at every 50th trace and snapping option in between. The basement reflection observed along lines 3 to 5 was picked manually due to its low coherency recorded along this horizon. The reflection events recorded below the Precambrian horizon, although appearing occasionally, were identified as multiple reverberations (Eaton *et al.*, 1999) and were not the subject of the presented analysis. In addition to this time consuming process it involved manual revision of the picks due to software malfunction as not every pick was saved successfully in the database. After the horizons were picked in both CMP and CRS stacks separately the data were ready to calculate the seismic attributes. Sample result of the picking steps performed along Pika horizon of line 6 is shown in figure 4.16.

Signal attributes were calculated within a wider window length above the Precambrian horizon of the basement. Different windows lengths were tested and finally the 200 ms window length located above the picked horizon was used since the smaller did not cover the investigated basement-sediments outcrop contact sufficiently. The investigation was performed along the composite profile and will be discussed in the final chapter (see Sec. 6.2 Fig. 6.4). It is worth to note that the selected window did not contained reflections belonging to the Devonian reef formations due to its significantly different amplitude characteristics that could disrupt the attribute analysis. This assumption was also valid for reverbations and multiples that was found below the basement reflector. Similar investigation that focus on crustal domains differentiation with the use of seismic signal attributes has been performed by Hope *et al.* (1999), but selected window was four times larger than selected here and contained almost all of Paleozoic sedimentary formations.

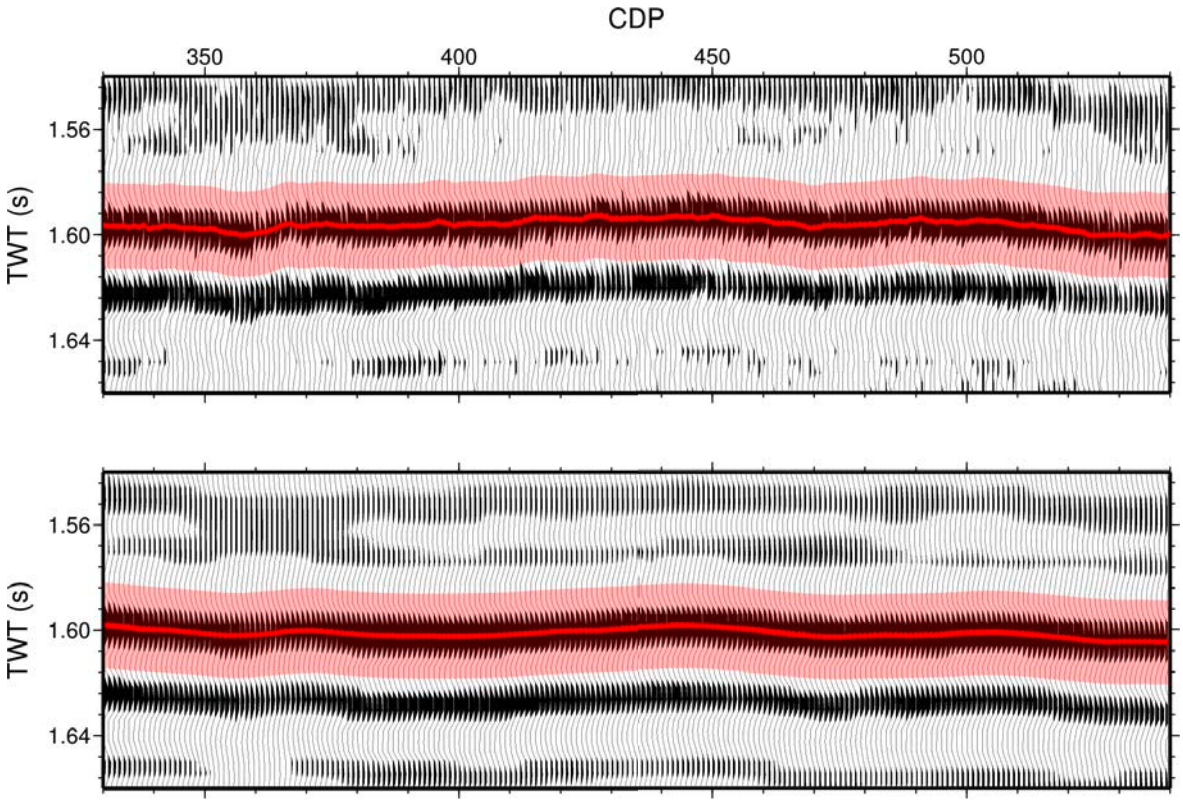


**Figure 4.16:** An example waveform of the Pika horizon obtained along CAT line 6 for the CMP (top) and CRS (bottom) stacked data. Note a visible improvements in the CRS stack corresponding to the reflection event observed below and above the Pika horizon.

Within a Promax© software length of the time window and its location in the relation to the signal waveform are the only parameters which the user must specify in order to calculate the attributes. A time window can be centered over the signal peak or shift up/down depending on desired effect. Figure 4.17 and 4.18 shows the RMS amplitude and instantaneous frequency attribute that where calculated within 40 ms window length centered on signal's peak of the Pika horizon. I made a window length selection upon the signal characteristics to encompass a full waveform of the reflection event.

The attribute values of RMS amplitude (see Fig. 4.17) falls between 0.4 and 1.4 for both stacks, while its average is significantly larger for the CRS stacked horizon. Such an effect lays upon the characteristic of the CRS algorithm in which stacked traces are characterized by significantly larger amplitude values (see Fig. 4.16). Generally, the RMS amplitude curve acquired from the CRS stack can be visible in the smoothed

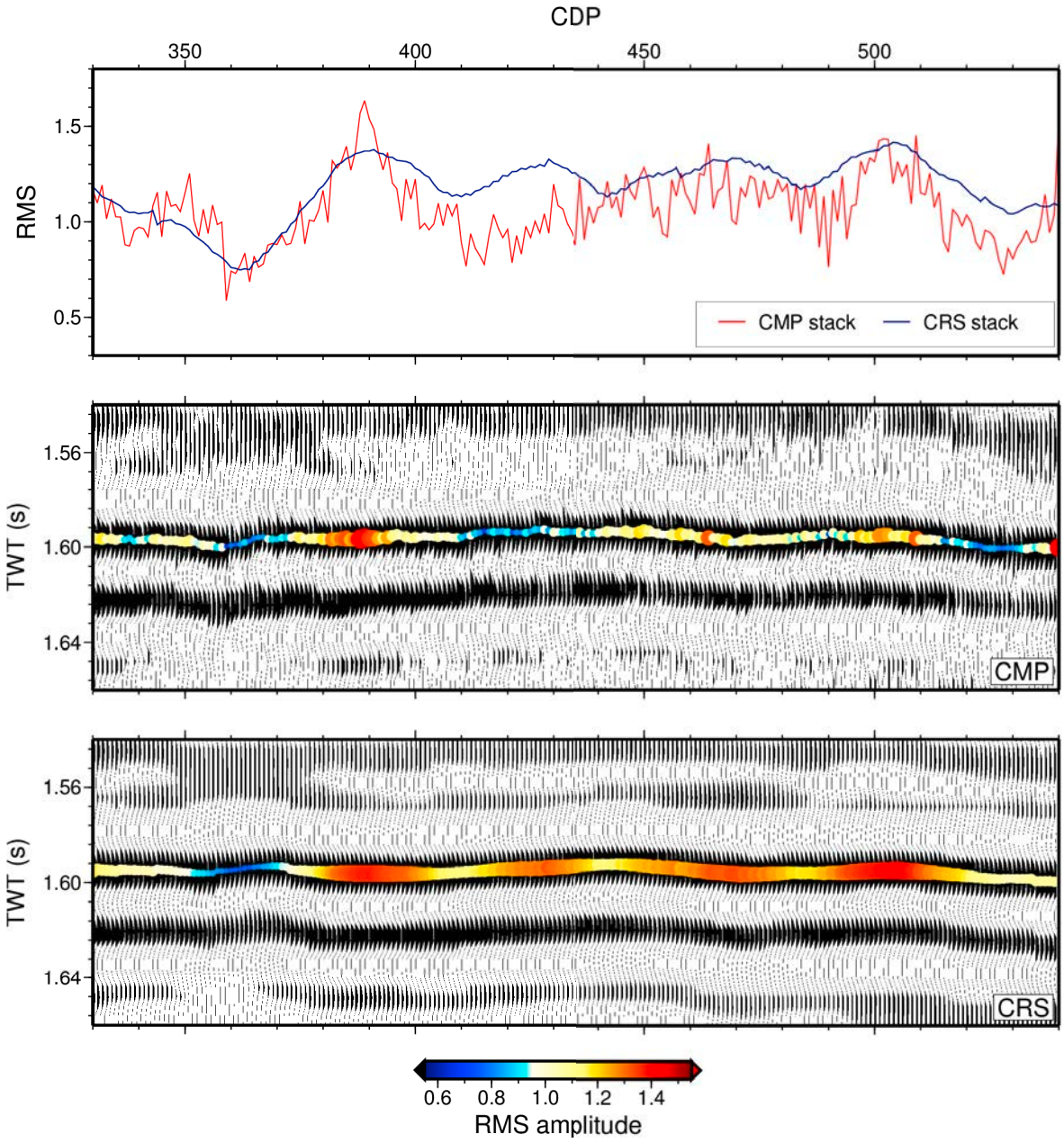


**Figure 4.17:** The result from a seismic signal attribute calculation obtained for both CMP (middle) and CRS (bottom) stacks acquired along Line 6 of the Lithoprobe transect. The attributes of RMS amplitude was calculated within ±20 ms window length (top).

form, leaving out noisy or other fine–scale structures that are typically observed within the CMP stacked dataset. Although the number of anomalies detected on both stacks shows high compliance in respect to the calculated values, however one anomaly did not

meet this criteria. In this case, the attribute values recorded between 410–440 CMP within the CMP stack are represented by negative anomaly while the CRS counterpart shown the positive trend.

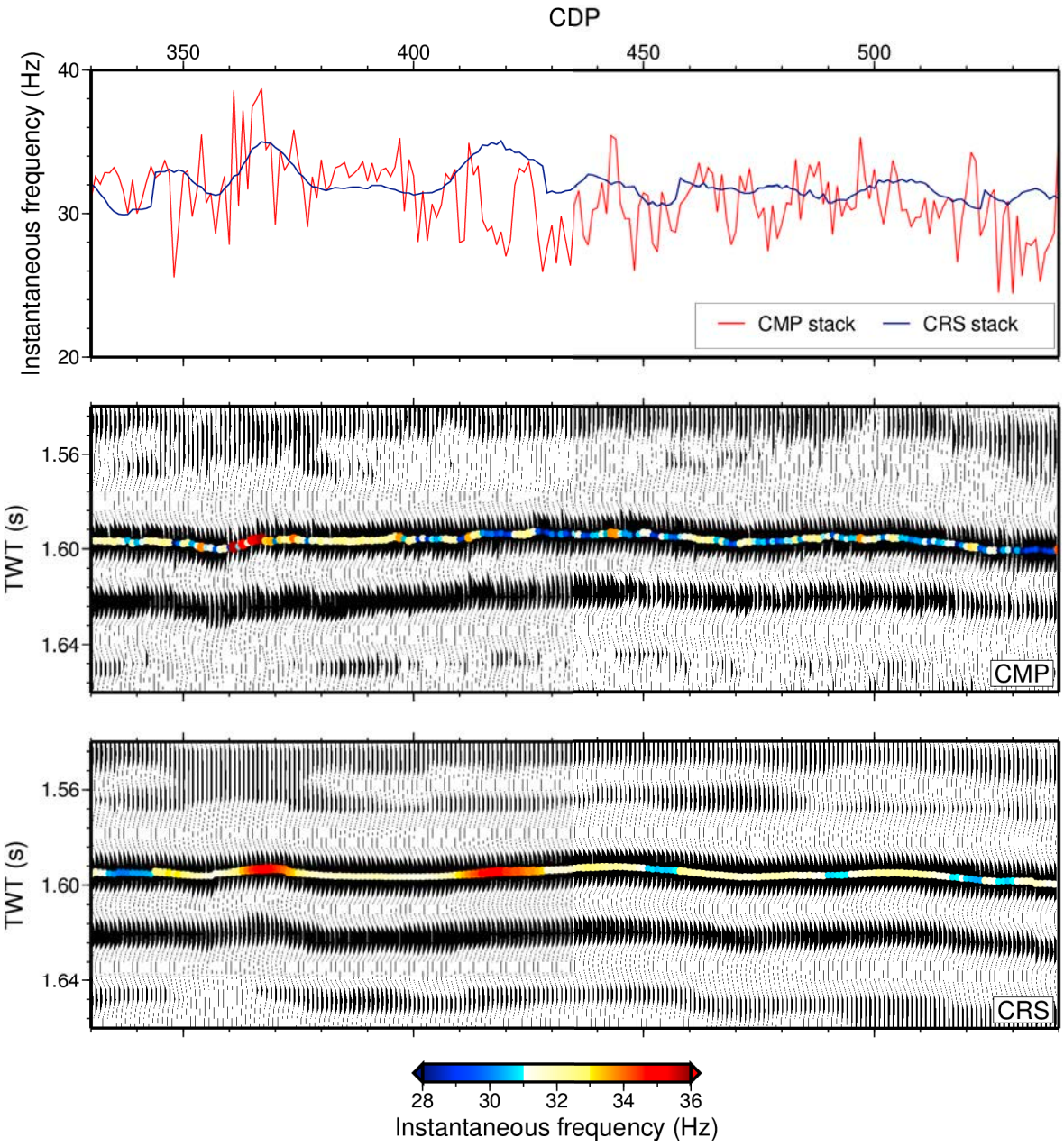


**Figure 4.18:** Typical results from an attribute calculation obtained for both CMP (top) and CRS (bottom) stacks acquired along line 6 of Lithoprobe transect. The attributes of instantaneous frequency was calculated within ±20 ms window length.

The attribute of instantaneous frequency calculated for the same sample profile of CMP and the CRS stack is presented on Figure 4.18. As can be seen, both profiles are dominated by an average frequency of 34 Hz showing anomaly peaks ranging from 20 to almost 40 Hz. Similar to the RMS amplitude acquired from CMP stack, the distribution of instantaneous frequency attribute is presented in the form of noisy curve dominated by a small–scale structures, however a three significant minimum anomalies can be clearly distinguished in the subset. Different results were obtained for the second curve, where as might be expected, a similar smooth effect is accompanied by the results obtained for the CRS stack. Even due to a considerable small variance values in the frequency distribution, which makes the detailed observation less visible, the same anomalies observed in the CMP stacked dataset were represented as the rapid phenomena of increased/decreased values.

Although a significant diversity in the frequency distribution makes the differentiation between CMP and the CRS method complicated, nevertheless it shows some specific correlation, especially those related to the CRS stacked data. For example, the effect of rapid phenomenons consisting of positive/negative pairs within amplitude and frequency can be easily identified at the CMPs 345, 430 and 460 suggesting the structural relationship. On the other side, there are positive amplitude anomalies recorded through the profile that are not correlated with frequency anomalies. Such an effect can be observed at CMP 390 and 470. Unfortunately, direct explanation of this effect can not be achieved by the simple signal comparison and other techniques or advance modeling studies should be incorporated. Therefore, more details concerning CMP and CRS stack comparisons as well as the detailed attribute interpretation I will present in the Chapter 6.2.

# 5

# Application to 3D data from Polish basin

## 5.1 Geological overview

The Polish Basin (PB) is an easternmost part of a set of epicontinental basins belonging to the Central European Basin System (CEBS). Numerous aspects of the origin and development of these basins have been analyzed by many authors in several syntheses and atlases (Bayer *et al.*, 2002; Dadlez *et al.*, 1998; van Wees *et al.*, 2000; Winchester *et al.*, 2002; Ziegler, 1990). The PB depocentral axis, named Mid–Polish Trough (MPT), is an elongated structure stretched in NW–SE direction and extends on the large area of the country (Fig. 5.1). MPT straddles the so-called Teisseyre–Tornquist Zone (TTZ; Guterch *et al.* (1986)) that defines the boundary between the East European Craton (EEC) to the NE and the Variscan front of the Bohemian Massif to the SW (Dadlez *et al.*, 1995). This boundary is formed by a very complex crustal structure, as recently indicated by newly interpreted deep seismic sounding data (Grad *et al.*, 2002; Guterch & Grad, 2006) as well as former gravity and magnetic studies (Grabowska & Bojdys, 2001; Grabowska *et al.*, 1998). The localization above TTZ, which is one of the major structural unit in Europe, makes the MPT unique among all the sedimentary European basins. Whereas intensive sedimentation process, since Permian times, makes the PB one of the deepest (10 km) and largest (500 km) basin over the CEBS (Ziegler, 1990).

The basin was initiated in late Carboniferous while its major development occurred in Mesozoic (van Wees *et al.*, 2000). Arthaud & Matte (1977) and Dadlez *et al.* (1995) argue that basin formation was due to the post-Variscan phase of wrench faulting

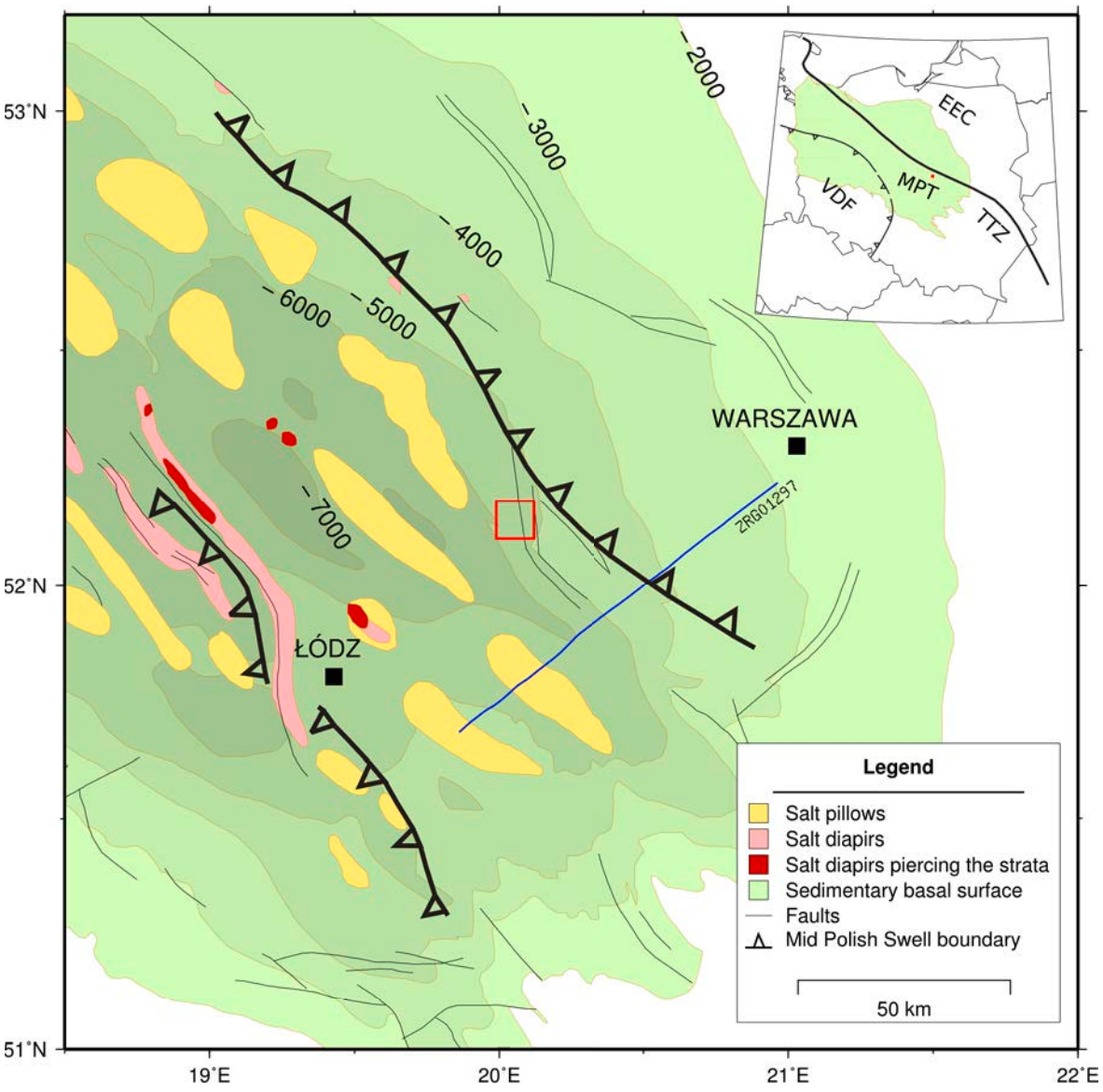


**Figure 5.1:** Geological map showing main structural units and tectonic features of the study area in central Poland (simplified after Dadlez *et al.* (1995); van Wees *et al.* (2000)). Red square indicates the study area. Abbreviations: EEC - East European Craton, MPT - Mid–Polish Trough, TTZ - Teisseyre–Tornquist Zone, VDF - Variscan Deformation Front.

coupled with Permo-Triassic rifting and preceded by Paleozoic accretion of Phanerozoic crust against the EEC. During the Late Permian–Mesozoic stage, PB was developed in the regime of thermal subsidence and continuous sedimentation along the basin axis and

interrupted by three tectonic subsidence pulses (Dadlez *et al.*, 1995; Karnkowski, 1999; Stephenson *et al.*, 2003; Ziegler, 1990). Those pulses of accelerated basin subsidence occurred in the Zechstein–Scythian, Oxfordian–Kimmeridgian and early Cenomanian can be explained by thermal attenuation of lithosphere (Dadlez *et al.*, 1995; van Wees *et al.*, 2000).

Structural trend of this complex is characterized by NW–SE-oriented syn-sedimentary and transversal faulting (Marek & Znosko, 1972). The remains of the subsidence process are several kilometers of sediments, interleaved by thick Zechstein salts layers (Dadlez *et al.*, 1998; Marek & Pajchlowa, 1997). In a later stage, from the Triassic to the Quaternary, syn-sedimentary salt movements caused the development of a complex system of salt structures (see Fig. 5.2). Various tectonics aspects as well as the heat transfer model have been analyzed by numerous authors (Bujakowski, 2003; Burliga, 1996; Krzywiec, 2004; Majorowicz *et al.*, 2003; Resak *et al.*, 2008). Later, during the Laramian orogenic event in the Late Cretaceous–Paleocene, sedimentary cover was inverted due to NE–SW-oriented intra-continental compression (Dadlez *et al.*, 1995) linked to a change of the convergence between Africa and Eurasia (Albarello *et al.*, 1995; Pichon *et al.*, 1988). This gave rise to the formation of regional tectonic unit called Mid–Polish Swell (MPS, Dadlez *et al.* (1998); Kutek & Głazek (1972)), intensively eroded in the Tertiary and covered by Paleogene sediments (Dadlez, 2003).

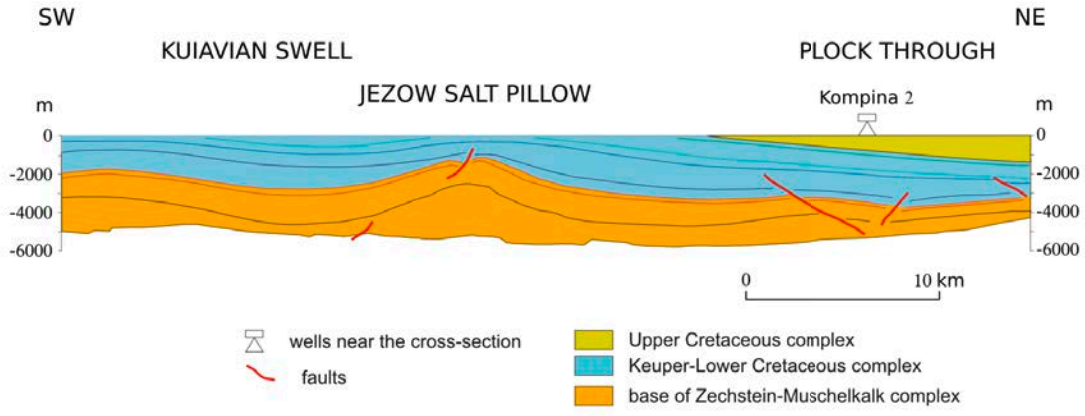


**Figure 5.2:** Regional geological cross-section illustrating the general geology of the Polish Basin, simplified after Górecki (1995). The locations of cross-sections is shown on the insert.

### Natural resources of MPT

The Mid–Polish Through is the major reservoir of natural gas in Poland. The gas deposits are accumulated in the southeastern part of MPT within the Permian horizons while in the northern part within the Carboniferous and Permian. The economic reserves within the MPT consist of $78.5 \times 10^9$ m$^3$ and represent of about 70 % of the total exploitable resources in Poland (Szuflicki *et al.*, 2013). The biggest gas fields located in southeastern part of MPT, Barnówko–Mostno–Buszów (BMB) that was discovered in 1993, has proved resources of around $9.9 \times 10^9$ m$^3$ (Mamczur & Radecki, 1998) accumulated within a dolomite reef structure.

In 2012, the crude oil resources that are hosted in Permian, Carboniferous and Cambrian formations stored within MPT represented 75 % of total Polish oil resources while the economic reserves within MPT consists of about $18.8 \times 10^6$ t crude oil (Szuflicki *et al.*, 2013). Similar to the gas field, the biggest oil field is BMB (Mamczur & Radecki, 1998), that has proved resources of around $7.8 \times 10^6$ t crude oil (double of the total reserves before its discovery). Another of great importance is the Lubiatów–Midzychód–Grotów (LMG) oil field, that was discovered in 1993 and has proven resources of $5.4 \times 10^6$ t (Papiernik *et al.*, 2009). The resources of the LMG oil field are stored in the Main Dolomite strata of the Zechstein cycloterm PZ2.

The major source of salt resources located within the area of MPT are Zechstein salts, that stretch over the late epicontinental basin and consist of the evaporates with the salt sediments, reaching 1000 m in thickness. Salt formations have structures of pillows and diapirs that have elongated form, stretched parallel to the general subsidence axis of MPT, as depicted on Figure 5.1. Although, the total exploitable resources consist of about $85 \times 10^9$ t (Szuflicki *et al.*, 2013), the exploitation is currently performed with limited scale (about $3.9 \times 10^6$ t) but these structures are in great interest for petroleum industry due to storage capabilities.

**Geothermal regime**

The Polish basin belong to a group of three main geothermal provinces in Poland (Sokolowski, 1993) that are selected based on geostructural units division. Basins formations host numerous geothermal aquifers developed by extensive sedimentation processes between the Triassic and the Cretaceous period. Relatively large thickness (from 7 to 12 km) of sedimentary succession dominated by the presence of sandstones and carbonates rocks makes it possible to distinguish six aquifers, reach in occurrence of geothermal resources (Górecki, 1995). Generally, the mesozoic formations are characterized with good hydrogeological and reservoir parameters. The heat flow rate values

vary from 20 to 90 mW/m$^2$ (Szewczyk & Gientka, 2009), while the reservoir temperatures that can be found at depths down to 4 km vary from 30 to 130 ° C. Water reserves differ between the horizons from several to 150 l/s, whereas total dissolved solids (TDS) of the water varies from several to 300 g/l (Górecki, 2006; Górecki *et al.*, 2003).

Determination of recovered geothermal heat in the manner of economic performance can be carried out in order to classify the perspective zones from which the geothermal heat can be commercially produced. Górecki (2006) applied the so-called "power factor" method (Gosk, 1982) to perform the economic evaluation of the Paleozoic aquifers in a simplified way. Based on such evaluation it was possible to indicate that the Lower Jurassic aquifer has the largest disposable resources among all geothermal aquifers of the Polish Basin and can produce $1.88 \times 10^{18}$ J/year of geothermal energy. On the other side, relatively low disposable resources occur in the Upper Jurassic aquifer. Its poor reservoir properties due to average permeability about 90 mD and low production rates from the boreholes allow to obtain $2.54 \times 10^{17}$ J/year of geothermal energy.

Currently, there are four plants using the geothermal water for heat production while another five are in realization phase (Kepińska, 2010). Two geothermal plants n are operated next to the site, which utilize the heat of underground waters for district heating. Since 1999, geothermal heat plant in Mszczonów, located 40 km southeast of the test site, utilizes water with a temperature of approx. 40 °C from the Cretaceous sandstones. The very low mineralization of the exploited water (TDS 0.5 g/l) makes it possible to use it both for heating and drinking. In Uniejów, 80 km west of the test site, since 2001 a heat plant exploits geothermal waters hosted in the same Cretaceous sandstones with temperature about 60 ° C and TDS about 5 g/l (Kepińska, 2003).

**Target horizon**

Within the study area, the basin is filled with sedimentary rocks ranging in age from Early Permian to Maastrichtian and its sedimentary succession is about 6000 m thick. Tectonic patterns are related to the Polish Basin general development stages and the layers lying below are the Permian–Mesozoic complex, however, the former seismic image indicates two zones, separated by a major N–S normal fault (Fig. 5.1). The eastern part presents a complex system of normal and reverse faults, striking predominantly in NW–SE direction. The western part is a basin with a sedimentary thickness that varies from 600 m near its borders to 2300 m at its center.

Three horizons, the most perspective for the geothermal usage, were found in the well Kompina-2 (Fig. 5.3) located in the central place of the site. Generally, Lower

Cretaceous horizon and Lower Jurassic are more productive and the temperature of geothermal medium reach below 100 °C. On the other side, the deepest reservoir, Upper Triassic found at depth of 4100 m, provides water with temperature about 110 °C but its production capabilities is fairly low.

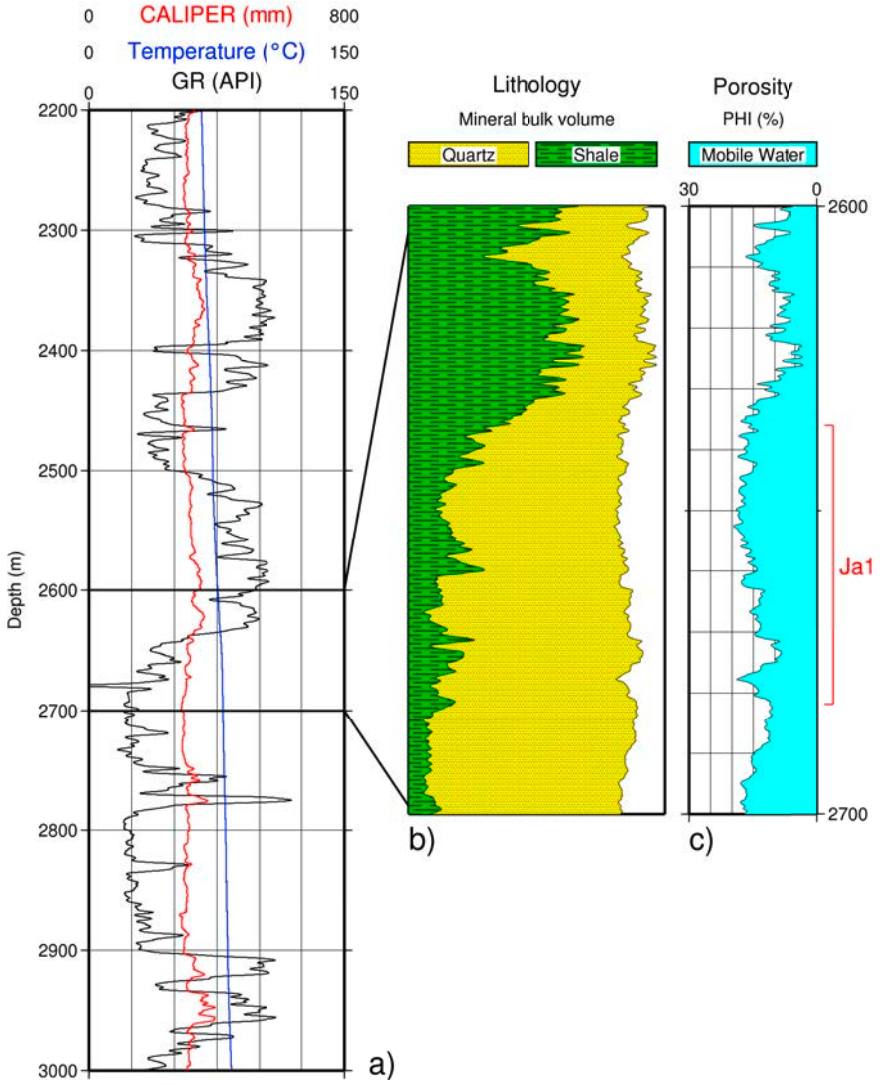


**Figure 5.3:** Well log curves for Kompina-2 well. From left a) Gamma, Temperature and Caliper, b) Lithology and c) Porosity profile where the brine outflow of 40 $m^3$/h was recorded from J1 horizon.

Three horizons, the most perspective for the geothermal usage, were found in the well Kompina-2 (Fig. 5.3) located in the central place of the site. Generally, Lower Cretaceous horizon and Lower Jurassic are more productive and the temperature of

the geothermal medium reaches below 100 °C. On the other side, the deepest reservoir, Upper Triassic found at depth of 4100 m, provides water with a temperature about 110 °C but its production capabilities is fairly low. The Lower Cretaceous aquifer spans over about 128 000 km$^2$ whereas its total thickness varies from several to over 400 m (Leszczyński, 2012; Marek, 1988a). Lower Cretaceous water saturated beds are composed mainly from permeable sands, sandy-marly and sandy-muddy sediments which forms a common water-bearing layer. Temperature distribution varies from 20 to 40 °C while in the survey area the temperature rises to over 50 °C which is related to the higher thickness of sediments in the axial zone. Among the Lower Cretaceous groundwaters, the lowest TDS was found in the survey area, where its value equals several g/dm$^3$ . Pumping tests performed in 60 water wells showed an average hydraulic conductivity value of about $7.8 \times 10^5$ m/s (Górecki, 1995). The Lower Cretaceous sedimentary succession reveals a higher permeability and occur at smaller depths but show comparable pressures in comparison with Lower Jurassic aquifer. Chemical contamination of the Lower Cretaceous groundwater is dominated by $HCO_3$ and Ca, whereas a salinity over 10 g/dm$^3$ is mostly due to the Cl–Na type brine (Górecki, 2006). Additionally, bromide and iodine ions within the geothermal waters of the Lower Cretaceous formation allow their balneological and recreational utilization.

The rocks, that build the Lower Jurassic aquifer, are composed of sandstones, interbedded with semi- or impermeable claystones, mudstones. Variable thickness of sandstone rocks, locally cracked due to tectonic activities, creates a typical artesian to subartesian aquifer (Bojarski *et al.*, 1979). In the survey area its thickness equals about 600 m whereas the permeable rocks build 50 % of its total thickness. Although, the Lower Jurassic sediments show vertical variability and facies changes, it may be suggested that reservoir waters developed as a continuous aquifer (Górecki, 2006). The hydrogeological parameters were obtained mostly from an old petroleum borehole and are sufficient to determine the complex storage efficiency values in limited accuracy. The chemical composition of the Lower Jurassic waters depends on geostructural factors that are characterized mainly by increased mineralization with depth. Its value varies from 0.2 to 174 g/dm$^3$ due to recharge areas fed with fresh, infiltrational waters, while its composition is dominated by $CO_3$–Ca, $HCO_3$–Na–Ca, $HCO_3$–$SO_4$–Ca types (Bojarski *et al.*, 1979; Górecki, 1995). Similar to the Lower Cretaceous aquifer, high concentration of iodine and bromine components make the geothermal water of the Lower Jurassic suitable for balneological purposes. Within the survey area the salinity

value is more than 100 g/dm$^3$ which is typical for that exceeding below 1500 m due to slow exchange rate of waters in the deeper parts of the Lower Jurassic aquifer (Bojarski & Sadurski, 2000). Since, the water discharge factor strongly depends on thickness of water bearing layer the discharge rate of about 250–350 m$^3$/h can be expected in the survey area. High intensity of exchange rate also affects the temperature distribution that makes from those typical of shallow fresh waters to 120 °C in the deeper part (Górecki, 2006).

Based on the production test carried out in well Kompina-2 and the quality of obtained data, the Lower Jurassic (J1) horizon was selected for further investigation. It is composed by the alternating layers of sandstone and claystone with total thickness in the 400-900 m range. In Kompina-2 they yield more than 150 m$^3$/h of about 80 °C water that has a TDS between 80 and 120 g/l (see Fig. 5.3).

Sediments of the Lower Triassic formations were developed within the marine environment of hot and dry climate (Marek & Znosko, 1972) that results in claystone–siltstone rocks with isolated patches of sandstone lithofacies. Although, the total thickness of the formation varies between a dozen meters up to 1600 m in the center of the basin axis, the aquifer thickness does not exceed 400 m in the central part and is less than 200 m in the remaining areas ((Marek, 1988b; Nawrocki *et al.*, 2013). The lower temperatures of a few degrees were measured at the edge of the structures, mostly on the eastern side, whereas the rising tendency was observed towards the basin center, where temperatures over 140 °C were observed. Similar trends characterize the distribution of mineralization, where values of a few g/dm$^3$ were measured at the marginal part whereas values up to 350 g/dm$^3$ dominate in the center (Górecki, 1995, 2006). Within survey area a temperature as high as 100 °C was observed and the mineralization of the geothermal medium was 250 g/dm$^3$. The whole area of the Lower Triassic aquifer is characterized by low hydraulic conductivity values (1-3 x $10^{-4}$ cm/s) that qualify it as poor aquifer. Its capabilities of discharges do not exceed 50 m$^3$/h over 50 % of the aquifer volume (Górecki, 2006).

## 5.2 Experiment description and data assessment

Several 2D seismic reflection surveys were acquired near the investigation area in the 1970s (Cianciara, 1975; Cianciara & Piech, 1977). Although, the measurements were performed by the use of 12-channel digital recording, however, in the results it was

possible to trace strong reflections from the formations of the Lower Cretaceous and Jurassic. The weaker reflections were obtained from the Triassic, mainly from dislocation zones and salt pillows in the Zechstein formations. Additionally to the seismics, there were semi-detailed magnetic survey and regional scale gravity measurements that indicate the presence of a big anomaly which is directly linked with the TTZ tectonic zone that crosses the entire country (Grabowska & Bojdys, 2001; Majorowicz, 2004).

The reprocessing of the old seismic surveys performed in 2006 (Borowska, 2006) showed the presence of three clearly visible structural levels, (1) the Dogger–Cretaceous level, characterized by gentle tectonics and the quite intensive subsidence that occurred during the Cretaceous; (2) the Upper Permian–Triassic–Lias level, mainly marine sedimentary rocks locally perturbed by salt tectonics; (3) the Precambrian–Lower Permian level, characterized by weak reflections and hard to identify without the borehole data.

The new experiment, a 3D reflection seismic survey was carried out in November 2007. Project was conducted within the scope of $6^{th}$ Framework European Programme titled "Integrated Geophysical Exploration Technologies for deep fractured geothermal systems - I–GET" (Contract No. 518378 SES6) and operated at the site by Mineral and Energy Economy Research Institute of Polish Academy of Sciences in Kraków (MEERI PAS). The main target of the project was to use the combination of seismic and magnetotelluric (MT) methods as the integrated tool to improve the detection of geothermal deposits and thus minimize the geological risk prior to drilling operation.

The Polish site, named Skierniewice, was treated as the test site selected due to low and intermediate enthalpy of geothermal deposits occurring in sedimentary rocks of the Cretaceous, Jurassic and Triassic formations (Bujakowski *et al.*, 2010; Cumming & Bruhn, 2010). Within the I–GET project similar formations were tested at Gross Schönebeck site, Germany (Bauer *et al.*, 2006). Based on that surveys experience, star–like arrangement for seismic layout was considered insufficient and was replaced with a grid seismic layout presented below.

The study region (Fig. 5.1) covered an area of about 30 $km^2$ and is located 70 km west of Warsaw, central Poland. The acquisition was carried out on an agricultural area that is crossed by a dense network of drainage channels which increased the acquisition time due to many bypasses. The land relief is characterized by a weak diversity in terms of topography and elevation along the individual profiles varying from about 95 m in the NW to about 85 m in the SE part of the survey. The complete survey took

**Table 5.1:** Acquisition parameters of the Skierniewice 3D seismic survey, 2008

| SURVEY PARAMETERS | |
|---|---|
| Receiver spread array | 8 lines x 170 active channels |
| No. of shot lines | 6 lines: S11-S12, S14; S16-S18 |
| No. of receiver lines | 8 lines: R11-R18 |
| No of source points | 252 (42 per line) |
| Shot spacing | 120 m |
| Receiver spacing | 40 m |
| Source | 4 x Vibrator Mark IV |
| Sweep type | Nonlinear +3 dB/Oct |
| Sweep length/frequency | 16 s/8-100 Hz |
| Taper | 0.3 s, 0.3 s |
| Recording system | I/O IMAGE |
| Geophone type | SM-24 |
| Geophone frequency | 10 Hz |
| No. of geophones per set | 12 over 2 m circle |
| Recording length | 6 s |
| Sampling rate | 2 ms |
| Maximum offset | 6178 m |
| CMP bin size | 40 m (inline and crossline directions) |

6 days, while 2 days were directly assigned to the data recording. The summary of the acquisition parameters is presented in Table 5.1.

To investigate the structural features around borehole Kompina-2 the orientation of source lines of the 3D seismic layout was designed perpendicular to the main geostructural trend (Fig. 5.4), indicated by NW–SE subsidence axis of the Polish basin (see Fig. 5.1). Therefore, three lines (S12, S14, S17) were oriented NE–SW, the three others (S11, S16, S18) in NW–SE direction. Additionally, to make the link between borehole and seismic volume more precisely, two of the source lines (S14, S16) intersected near well Kompina-2. Seismic signals were recorded along eight receiver lines (R11-18). Six lines (R11-12, R14, R16-18) were parallel to the equivalent source lines whereas the two additional lines oriented N–S (R13) and W–E (R15) also intersected well Kompina-2. The reason of using two additional lines allowed to increase the minimal fold and incorporate additional offsets, as expected. The total length of the six source lines was 29 km whereas the eight receiver lines was 54 km.

Due to the environmental regulations (Borowska, 2006), acquisition was performed with the use of Vibroseis© technology, performed over reflection seismic layout. As seismic source, four vibrator trucks were used in-line along six source lines oriented in a grid with lines spaced at 1000 m. The seismic signal was generated by the vibrators at the frequency range of 8-100 Hz and a sweep length of 16 s. A recording system based on single-element, vertical component geophones spaced at 40 m, was used to record

the signals during the time of 6.0 s at sampling rate of 2 ms. With differential GPS technology and GPS devices mounted on the vibrator trucks the recording sites and shot localizations reached the accuracy of about 0.01 m. Recorded signals were stored on 4 mm tape in SEG-D format (Barry *et al.*, 1975) whereas survey parameters in SPS format (SEG, 1995).

Shallow refraction measurements were performed in addition to the reflection survey in order to investigate the low velocity zone (LVZ). A hammer source was used to generate seismic signals along five short profiles (not indicated on Fig. 5.4) over a spread of 180 m length with various receivers spacing. The velocity obtained below the LVZ from refraction measurements varies between 1700 and 2200 m/s and was interpolated over the whole layout (Borowska, 2006).

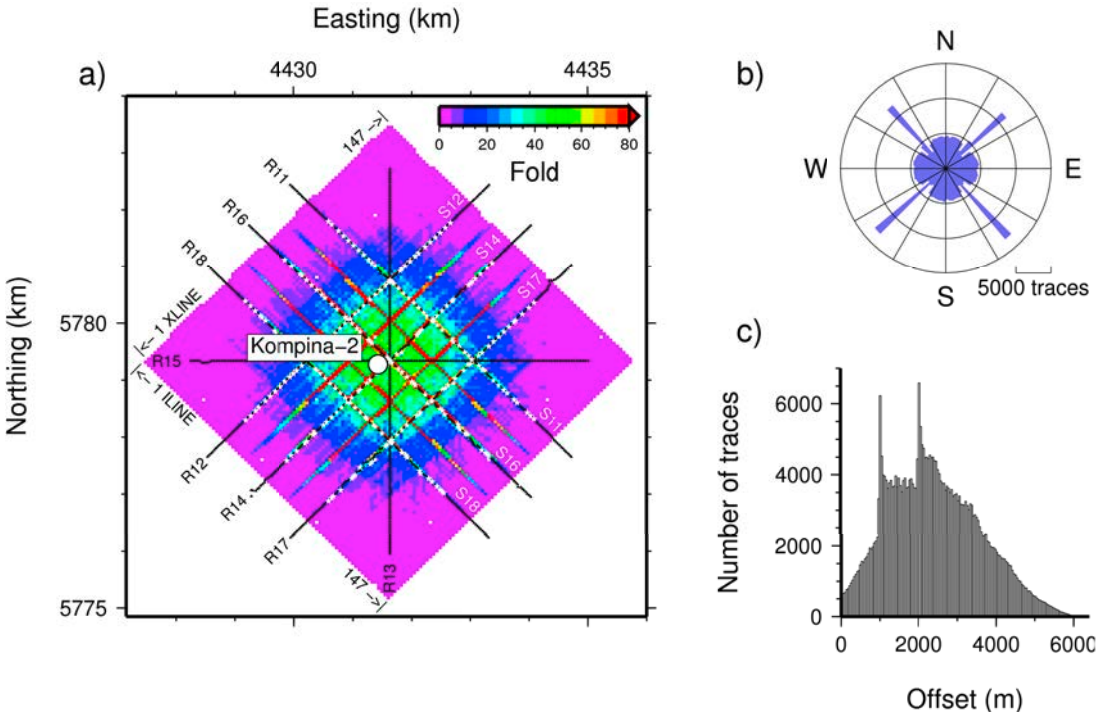


**Figure 5.4:** The layout of a sparse 3D reflection seismic survey acquired in Skierniewice site. (a) Acquisition geometry plotted onto CMP fold coverage map obtained for a CMP bin size of 40x40 m. The sources are indicated by white stars, receivers by black triangles and Kompina-2 borehole is located in the middle b) Azimuth distribution form the survey (grouped together into sector for display purposes), c) histogram of Source-Receiver offset distribution.

Seismic reflection data were acquired at 252 source localization, spaced at 120 m

intervals over a grid with 1360 channels used simultaneously. In the results, about 342 000 seismic traces were collected during the data acquisition. Although, a maximum obtained offset of 6188.78 m (see Fig. 5.4c) ensured the identification of the deepest Permian horizon within the survey area, however, due to limited number of traces with such long offsets, the penetration depth was rather limited to 4000 m depth.

Overall dynamic range and continuity of recorded signal was good and allowed to trace the reflections from the sedimentary succession of the Cretaceous, Jurassic and Triassic formation. The seismic reflection events from deeper parts are characterized with less quality of recorded signals, however the lower Triassic formation expected at 2.5 s TWT are still observed. Figure 5.5 shows typical raw shot gathers with high quality of recorded signals and clearly visible first arrivals. Also several distinct reflections can be found deeper along all receiver lines, however its number and quality decrease with distance from the source. Analysis of the amplitude spectrum indicates that dominant frequency ranges vary between 40-50 Hz and the low-frequency noise is mostly associated with ground roll, typically below 30 Hz.

## 5.3 CMP Processing

Within the frame of this thesis, simultaneous recordings from 1360 active channels were processed as a sparse low fold 3D survey with a 2.44 $km^2$ homogeneous fold area in the center of the survey. Such a sparse survey becomes widely accepted and allows to reduce acquisition cost while achieving imaging objectives with sufficient resolution (Eisenberg-Klein *et al.*, 2008; Trappe *et al.*, 2005). It is worth to note that the survey, however, was designed as a sparse 3D measurement that also allows to process the dataset in the form of six independent 2D lines, composed of 170 channels each (with 28 CMP fold).

The review of original processing sequence performed in 2008 (Bujakowski *et al.*, 2010) followed the setting of new processing parameters. This allowed to identify crucial steps that were applied to solve some key data or noise issues occurring within the dataset. The original processing sequence was based on the standard procedure for land seismic reflection data (i.e. (Yilmaz, 2001)), although special attention was given due to non uniform offset and fold distribution within bins. Table 5.6 shows the parameters of principal steps applied during the processing. Generally, it based on the assumption that the flat sediment deposits with different acoustic impedance found in the study

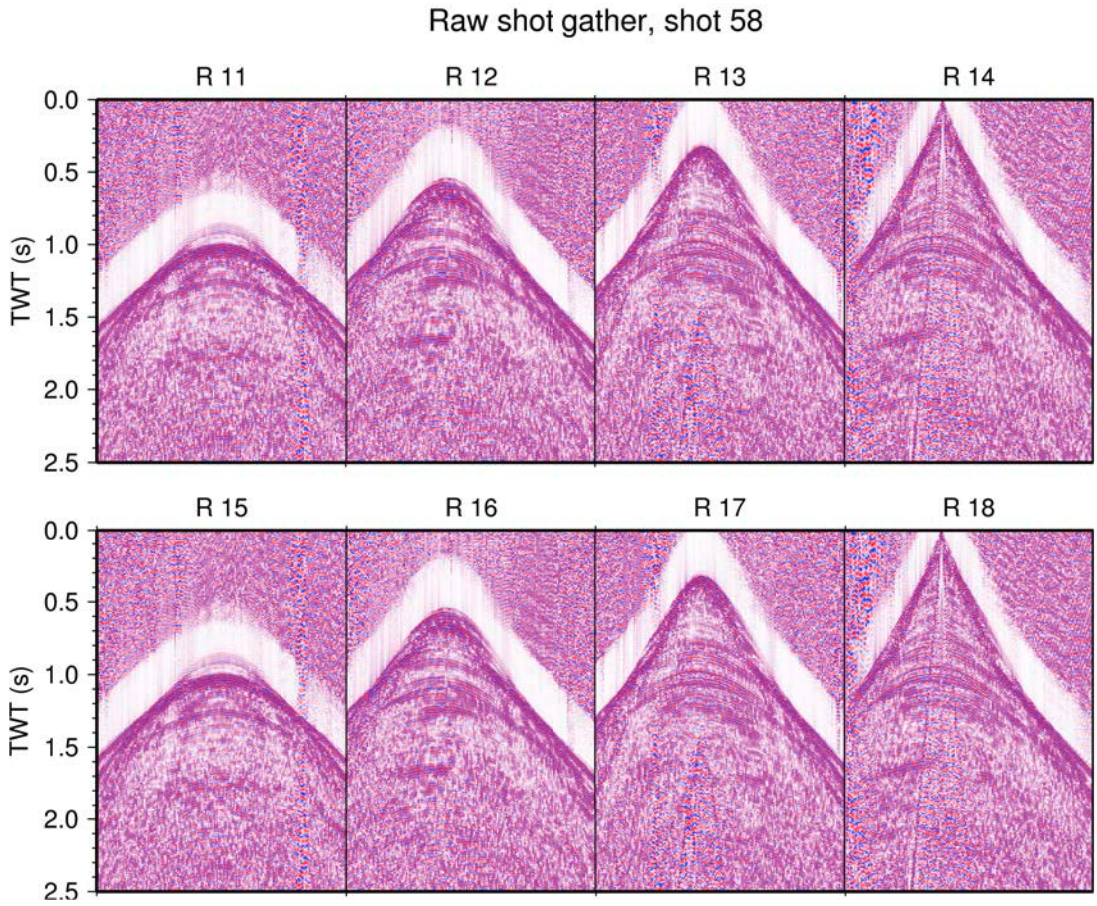


**Figure 5.5:** Raw shot gather from the shot number 58 recorded onto receiver lines R11-R18. Reflection from the sedimentary successions are still visible down to 2.0 s. In addition to the very good signal quality of the several primary reflections, note the ground roll visible on line R13-15 and R18.

area, should produce strong reflections. The original data were provided as a single file in SEG-Y format. An additional file, containing the survey information stored in SPS format, was used to set up the geometry within the Promax© processing software. Provided records had already been demultiplexed and correlated with vibrator signal. In the first step, data were loaded into the processing software and changed to its internal format which increases the speed up the whole processing.

An important question for further processing was the appropriate CMP binning. Typically, bin size equals half of the receiver group spacing, however this produced a very low CMP fold value of around 6. Such a low value covered a large part of the grid which caused a high disproportion in fold distribution, and allowed credible

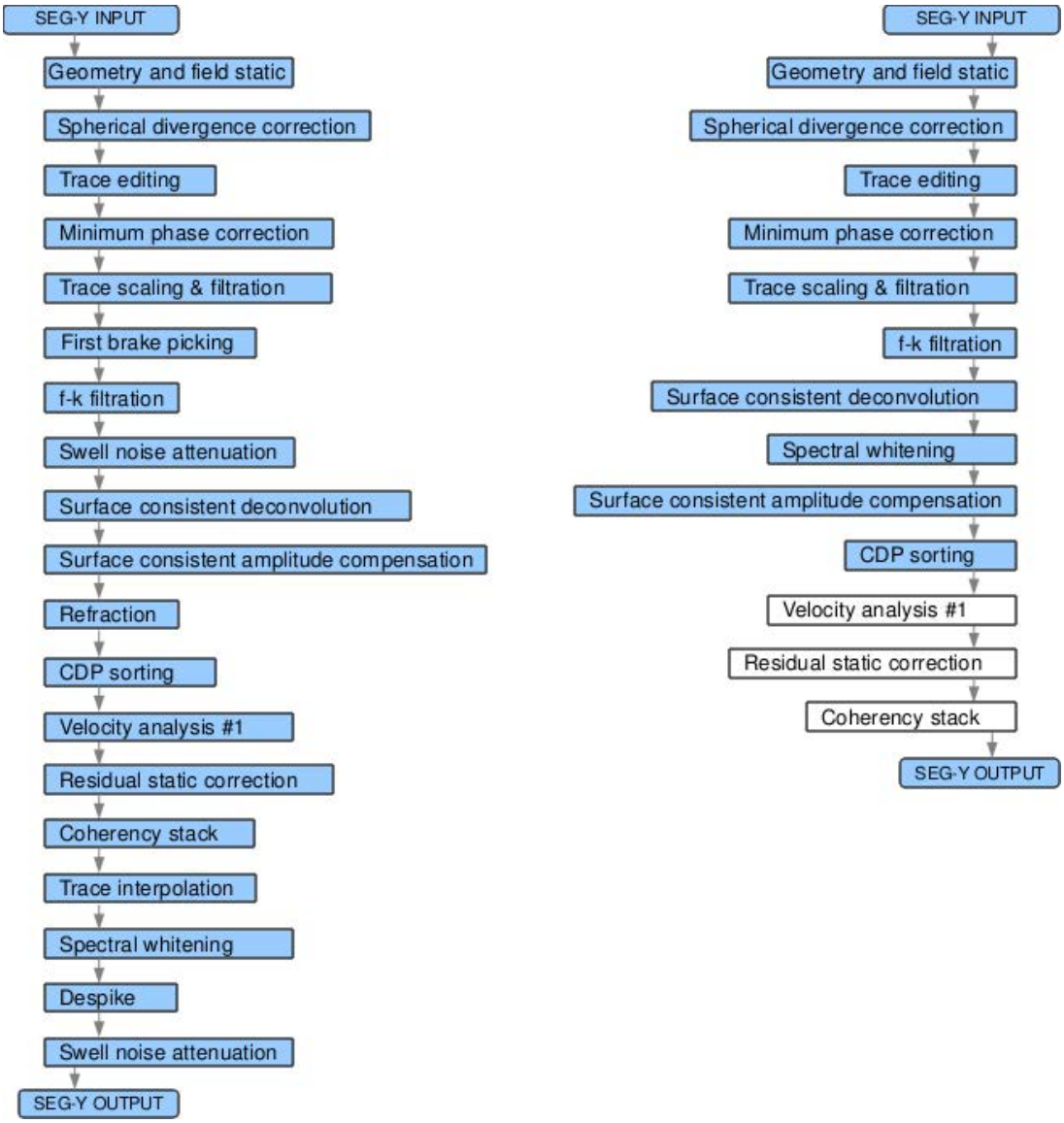


**Figure 5.6:** Processing flow of 3D seismic reflection data from Skierniewice site, Poland. On left side, processing sequence performed by Geofizyka Krakow (Bujakowski *et al.*, 2010). Right column contains the steps of processing adapted for the comparison purpose. On white are the matched the steps not included within the CRS processing method.

interpretation only along source lines. Based on tests with various bin sizes that may increase heterogeneous value of the coverage factor, I decided to choose a CMP bin size of 40 m by 40 m, which is equal to the group spacing along receiver lines. I followed the equation proposed by Yilmaz (2001) which defines the relationship between the bin size

and the frequency required to resolve the target reflector (spatial sampling theorem). For an assumed depth of a target reflector of about 3400 m and the structural dip of about 20°, the maximum allowed non-aliased frequency is about 80 Hz which is close to the maximum emitted frequency. The new bin size provides a homogeneous coverage of over 40 (Fig. 5.4 in the central area delimited by the source lines 11-18 and 1217, while the lowest fold values were obtained near the grid border.

Promax© 5000 of Landmark was used in order to increase S/N ratio and enhance quality of the seismic recordings. I used it also to prepare the input data for the CRS processing. Prior to geometry installation, records were checked to remove noisy traces or malfunctioning geophones from the shot records. I applied timing correction, elevation statics correction, automatic gain control (AGC) and bandpass filtering. After the trace editing, top muting was applied to remove direct and refracted waves. Because of smooth elevation changes in the investigated area, a fixed flat datum was chosen for the processing instead of a floating datum. Elevation statics were already acquired within the dataset and were incorporated into database geometry at the beginning. Dataset was filtered by the use of single zero phase Ormsby bandpass filter defined by 8-13-60-100 Hz frequency corners. The first two numbers represents corners of the 0 % and 100 % of the low-cut ramp, whereas the last two 100 % and 0 % of the high-cut ramp on designed filter. A single gate, 750 ms length, automatic gain control (AGC) was applied to the CMP gathers in order to enhance the amplitude reflection response recorded at later times.

From general definition, seismic recordings may be considered as the composition of signal and noise. Moreover, any kind of recorded energy which interferes with the seismic signal can be seen as a noise. Therefore, noise removal is an essential process in order to obtain a high quality seismic image, although, the wide spectrum of noise types often makes its extraction a challenging process. One of the important processing steps is the application of deconvolution in order to increase the temporal resolution, preserve a high frequencies and remove multiples effect. Multiples can be removed by the use of a later portion of the wavelet auto-correlation, where arrival times of multiples can be predicted from the knowledge of the arrival times of primary reflections. In order to fulfill this assumption and find optimum resolution for the target horizons a surface-consistent deconvolution (Levin, 1989) was applied using the following parameters: prediction step 12 ms, operator length 120 ms, single-time gate: 350-1250 ms. Additionally, in order to increase resolution of the data I applied f-k filter

(Yilmaz, 2001) to remove acoustic and surface waves. The step helped also to remove high-amplitude disturbance and to suppress steep amplitude variations. Figure 5.7 presents sample shot gathers with the influence of various processing steps and their impact on signal to noise ratio (S/N) reduction.

Until now, the seismic dataset was stored as shot gathers, however further processing steps i.e velocity analysis requires additional CMP sorting that includes CMP bin location beside existing information of source and receiver locations, field record numbers, etc. Determination of NMO velocities was performed by the use of semblance analysis on a subset of the in-line and cross-line CMP positions. These locations overlapped with high fold lines source lines and between. Then, velocities were interpolated for all CMPs in the 3D volume. There were no significant velocity variations lateral nor vertical observed throughout the volume that could indicate the presence of salt structures in the region characterized by strong velocity variations compared to the surrounding sediments. Relatively continuous distribution of reflections over the volume allowed stacking velocities of the topmost reflection to be picked and determined reliably.

As the final stage data were stacked by the use of common-mid-point stacking procedure (see Fig. 5.8a,d). In consequence, an increase in reflection continuity and reduction of the refracted energy were observed along all control lines. Despite a non-uniform offset distribution and fold area inside bins, the final stack image is comparable with the processing results obtained from standard 3D seismic surveys. Good quality of the seismic reflections from the Cretaceous, Jurassic, Middle and Lower Triassic horizons allows to recognize the geological formation in the study area. Even the seismic horizons with lower quality signals (i.e. Upper Triassic) can be discerned. Within the structural interpretation, it can be seen that investigated area is represented in the form of a complex structure formed under the influence of uplift and salt tectonics (Borowska, 2006). Although, CMP stacked volume was ready to compare with CRS counterparts its further analysis was expanded to include lithofacial interpretation based on the application of seismic attributes i.e. root-mean-square (RMS) amplitude and instantaneous frequency (see section 6.2).

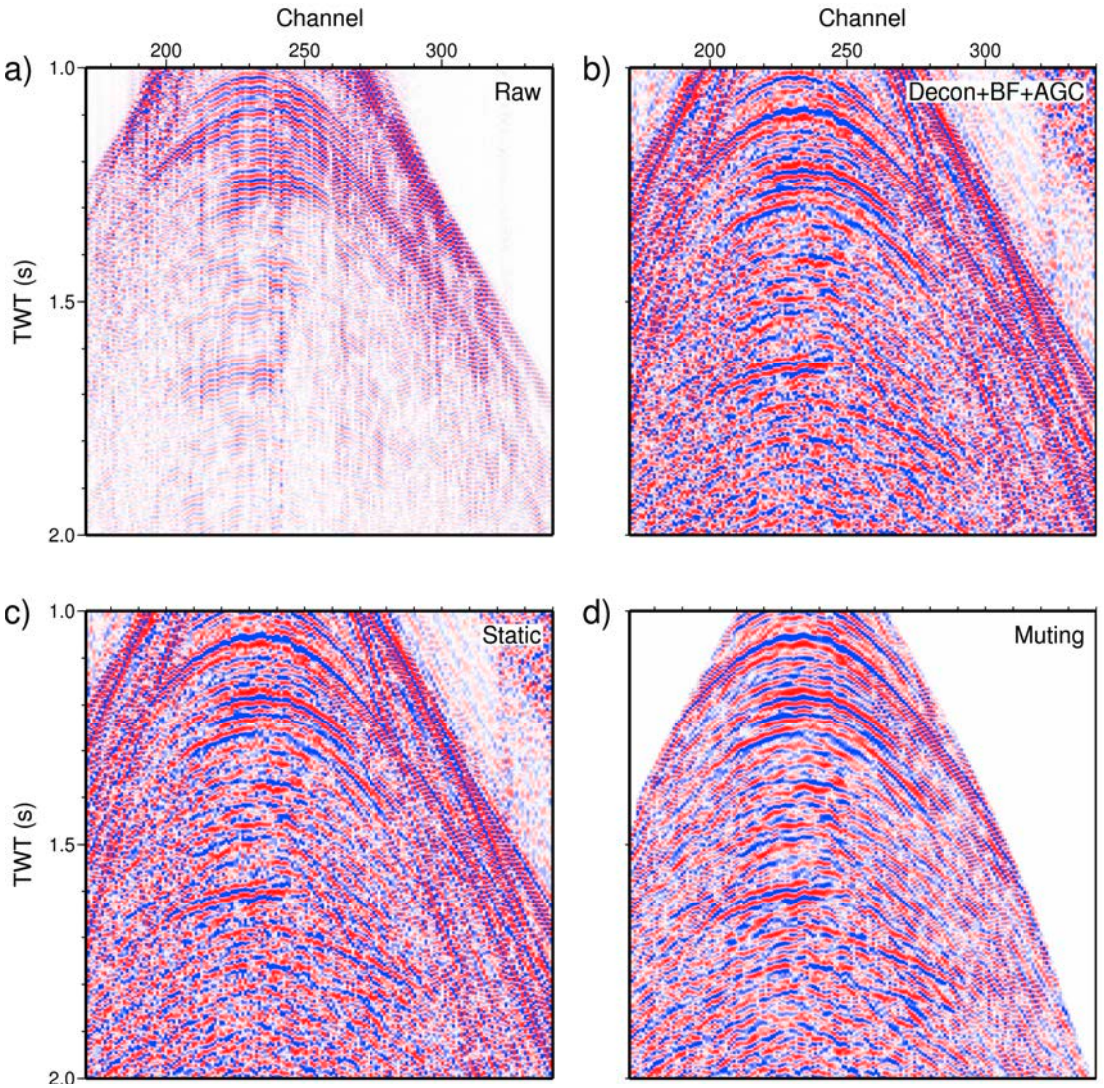


**Figure 5.7:** The consecutive results of processing steps performed on shot records data from Skierniewice site - a) raw shot gather, b) surface consistent deconvolution, c) static correction and d) top muting.

## 5.4 CRS Processing

The CRS method of Mann *et al.* (1999) was applied parallel to the conventional CMP stack processing. As described in section 3.2 conventional CMP stacking method is based on the assumption of planar reflectors. An interactive velocity analysis tool is used to determine the NMO velocity, the required parameter to correct for the geometrical effect of different source-receiver offsets and perform the summation process. The

CRS stack represents a more generalized approach in which the assumed correction is defined by the location, orientation and curvature Mann *et al.* (1999) of an assigned surface. As a consequence, parametrization of the CRS stack operator allowed the CRS method to be applied without a known macro-velocity model, which means no an additional velocity analysis is required in principle. Within the general data processing work flow the CRS method can be used as a substitute for the NMO velocity analysis, and subsequent stack of the NMO corrected traces. The processing steps applied to the data before the CRS stack are identical with the conventional processing. Practically this means the data were processed in the conventional way as described in section 5.3 (Fig. 5.6), but were exported without the following application of the NMO correction. The subsequent CRS processing includes the determination of the CRS stacking operator and the application of this operator during stacking (see Sect. 3.3). As mentioned, the CRS stacking operator is based on the concept of so-called eigenwaves (Hubral, 1983). These hypothetical waves include (1) an up-going Normal Incidence Point (NIP) wave generated from a point source at the reflector, and (2) an up-going normal N wave generated from an exploding reflector. Following this proposed idea, the reflected wave field measured at the surface can be described by three parameters forming the CRS stacking operator (Mann *et al.*, 1999): (1) the common emergent angle $\alpha$, (2) the curvature radius $R_N$ of the N wave front, and (3) the curvature radius $R_{NIP}$ of the NIP wave front. These quantities are used in a parametric description of the wave field at the surface based on par-axial ray theory (Schleicher *et al.*, 1993). In the implementation of Mann *et al.* (1999), the three parameters are determined for each sample of a simulated zero-offset section by fitting the measured data with maximum coherency (Neidell & Taner, 1971).

The CRS parameter estimation is carried out by subsequent solution of single-parameter determination (Mann *et al.*, 1999; Müller, 2007). Recent developments by Garabito *et al.* (2012) make use of global optimization approaches instead of the single-parameter estimation concept, but this method is established in 2D but not yet in 3D so far. The data are first processed in the offset-domain similar to the CMP processing, where a NMO velocity is determined automatically based on the maximal coherency fitting of the data. This automatic NMO velocity implicitly depends on a combination of the CRS parameters curvature radius $R_{NIP}$ and the emergent angle $\alpha$. All three CRS components are subsequently determined in the zero-offset-domain, with additional consideration of the previously derived automatic NMO velocity values. More details

**Table 5.2:** CRS processing parameters applied for 3D land seismic data from Skierniewice

| | |
|---|---|
| Surface velocity | 1600 m/s |
| Minimum offset aperture | 1200 m at $t_0$ |
| Maximum offset aperture | 1500 m at $t_{max}$ |
| Maximum midpoint aperture | 200 m |

of the CRS method and the corresponding work flow are given in Mann *et al.* (1999) or Müller (2007). The main aim of successful CRS processing is to find out the proper size of the CRS input parameters. To minimize the processing time of simultaneous parameter search, which is expensive from the computation point of view, I used a technique of single parameter search originally developed and modified by Mann *et al.* (1999), Jäger *et al.* (2001) and Müller (2007). The computer center at the GFZ with a cluster consisting of 32 nodes served mostly during data processing. Due to elongated calculation time it was necessary to perform the initial test on a smaller volume, as the total computation time of the 3D seismic volume took of about two weeks. The major parameters of CRS processing selected for the final search are summarized in Table 5.2, whereas the following section presents its results.

As described in section 3.3, CRS processing is a multiparameter search method where eight kinematic wavefield attributes (in case of 3D input data) need to be determined. Because the simultaneous parameter determination is inefficient, the CRS method is divided into three subsequent steps to obtain each of the kinematic attributes respectively. In the results of the CRS processing sequence, each step provides a CRS stacked volume and additional volumes of CRS kinematic attributes. The first step within the CRS processing chain is the automatic process of hyperbolic CMP search. It is based on the calculation of best-fitting stacking velocity curves within the CMP domain. As the consequence of the hyperbolic search step, CRS parameter and coherence volumes are created as well as CMP stacked ZO volume that is derived by the application of the stacking operator to the prestack dataset (see Fig. 5.8b,e). The information about velocity field was not provided, therefore the search was performed under unconstrained circumstances. I used stacking velocities within the range of $v_0$=1600 m/s and $v_{max}$=4800 m/s.

The result from the hyperbolic search, the CMP stack section derived from preprocessed CMP gathers with a velocity model obtained and a stacking operator determined under unconstrained conditions, is shown on Figure 5.8b,e for both low and high fold

cross sections. An AGC of 500 ms window was applied to enhance the image resolution and improve the visibility of deeper reflections. The obtained image shows that the reflection events can be identified as deep as 2.0 s TWT. Furthermore, the CMP search brings out a some more improvements when compared to the standard CMP stacked section. The reflection events show a better continuity along the horizons as well as from the target reflector recorded at 1.8 s TWT and deeper one. The improvements on the low fold section (Fig. 5.8b) are not significant and the noise level is comparable to the low fold section obtained from CMP stacking (Fig. 5.8a). This fact is important due to an AGC filter enhances both the amplitude of seismic signal and the noise, therefore its further interpretation should be performed with special care. The initial comparison of the conventional CMP stack (Fig. 5.8a,d) with the results obtained by the automatic CMP stack (Fig. 5.8b,e) shows already that minor improvements can be achieved in the first step of the CRS processing. The proper selection of the aperture size in the offset-domain is the most influential parameter at this step. Based on the many tests I used the aperture size within the range of 200 m at 0.0 s and 2000 m at 3.0 s of recording time that allowed to include as much reflection wave forms as possible.

Generally, the automatic CMP stacked volume is characterized by good quality reflections that have been recorded in the time window of 0.1-2.0 s TWT. In particular, the gently dipping sedimentary succession of the Cenozoic, the Cretaceous and the Upper Jurassic is depicted in form of good continuity events with a noticeably impedance contrast visible at 0.8-1.4 s TWT. The Lower Jurassic formations package, significant due its geothermal potential, is visible down to 1.8 s TWT. Within the Lower Jurassic package, the most productive horizon Ja1 has been imaged with high impedance contrast (marked by gray arrow). The differences between low fold and high fold images (b,e), however similar to the standard CMP stack, present little more improvements. These are visible mostly within younger formations up to 1.5 s TWT on both cross-sections. Although the reflections from deeper horizons are not resolved ultimately, and can be seen as disturbed and without continuity, some improvement is observed, especially on the high-fold cross-section.

The Ja1 horizon recorded at 1.65 s TWT is very well imaged and allows for highly reliable correlation, both in inline and cross-line direction. Moreover, the remaining horizons show similar structural engagement, repeating the tectonic features between neighborhood units located below and above. Conflicting dip situations often appearing within sedimentary environments due to the presence of salt structures, were not

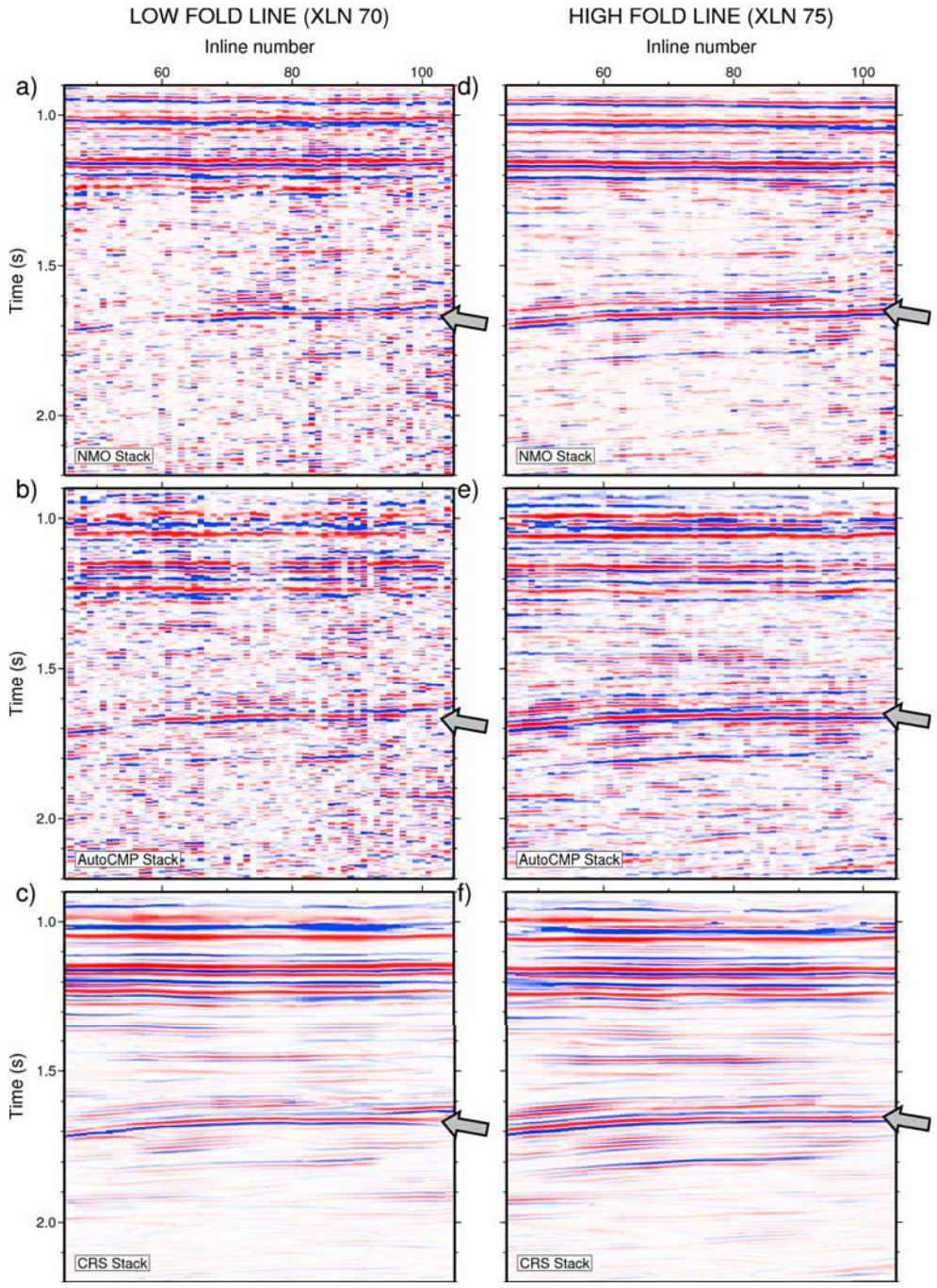


**Figure 5.8:** Distribution of the zero-offset two way-time from the Skierniewice site obtained in terms of coverage. The Ja1 horizon, indicated by gray arrows represents the major geothermal target within the investigated area. Description of particular figures in the text below.

identified, thus most of migration technique should provide very good results of a real image of subsurface. Reflection responses in both, the CMP stack and the CRS stack, recorded below 2.5 s TWT are poorly imaged due to the relatively low S/N ratio, therefore the correlation of deeper horizons is more complicated than those recorded at shallower parts due to energy loss with depth.

In the last procedure, the CRS processing flow is based on the calculation and the application of the CRS stacking operator in order to obtain the CRS ZO volume. The main components of this procedure are the kinematic attributes acquired in the previous steps and the resulting stacking operator. Similar to the previous steps, the final CRS stack volume is accompanied by a coherency counterpart. Figure 5.8c,f) shows the result of the final CRS step acquired after the determination of all three kinematic CRS attributes. It represents a significant improvement when compared to both, the conventional stack (Fig. 5.8a,d) and the automatic CMP stack (Fig. 5.8b,e). In the last step, a crucial control parameter was the proper choice of the aperture in the midpoint-domain. Based on estimations of the first Fresnel radius, supported by acoustic measurements in the well Kompina-2, I used aperture size within the range of 50 m at 0.0 s and 300 m at 3.0 s recording time. The improvements achieved by the CRS stacking are obvious in the cross-sections considering the continuity of the wave forms along the target reflector and in its vicinity. The most valuable reflector is marked by an arrow on. Based on the results of Bujakowski *et al.* (2010) this structural horizon was identified as the lower Jurassic horizon Ja1, which represents one of the major target for geothermal exploitation at this location.

Although the improvement between CMP and CRS cross-section is easily visible, an interesting difference can be seen on the low fold sections, where many additional reflections and structural features were identified. The shallower sedimentary succession which is characterized by the undisturbed and continuous sedimentation process (Borowska, 2006; Bujakowski *et al.*, 2010), is easily identified along both low- and high-fold crosssection of the CRS stack. For example, two horizons recorded at 1.37 and 1.45 s TWT provide sharp and continuous horizons, whereas the CMP stack image shows hardly visible partial reflectors which can be identified only by the correlation with high fold cross-section. Similar conclusions can be achieved when considering the deeper parts of subsurface, additionally affected by tectonic activity visible on the left side. Here, the horizon recorded at 1.75-1.8 s TWT on the high fold line of the CMP

stack is not visible on low fold section (Fig. 5.8a), whereas can be easily recognized on their CRS counterpart, providing sharp and continuous reflection events.

The practical aspect from this experiment allows to assume that the application of the CRS stack not only improve the imaging capabilities itself but when applied to the low fold data it allows to image the reflection events that are partially or even not visible when resolved by the CMP stack technique.

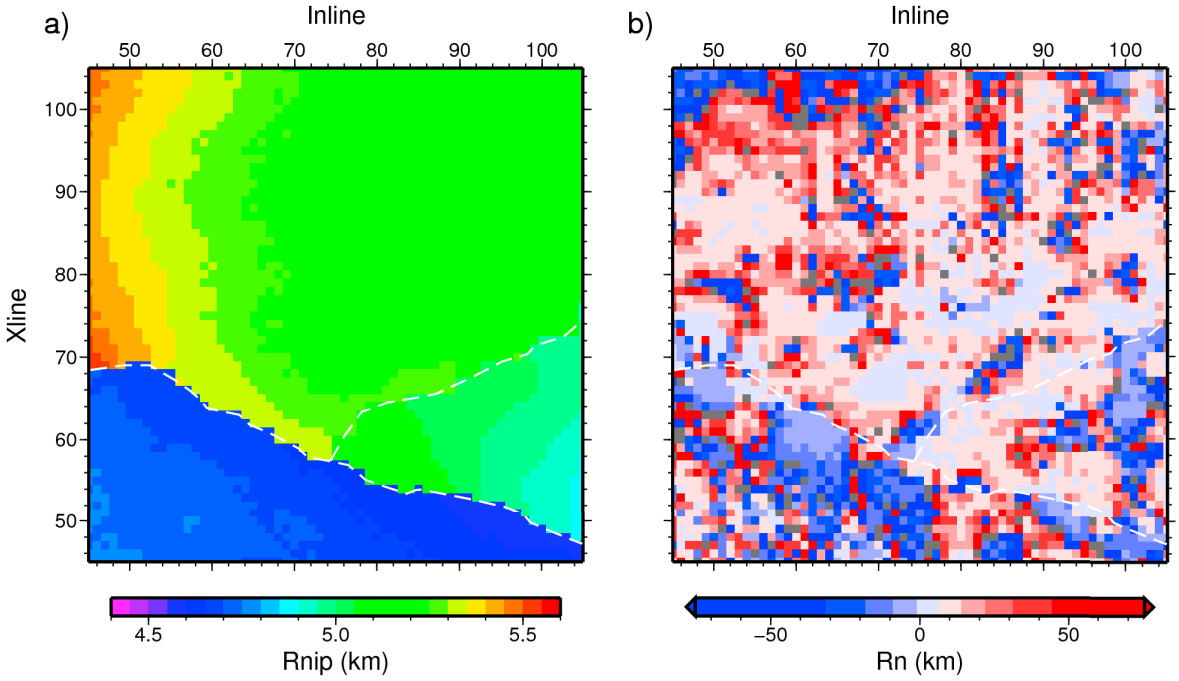


**Figure 5.9:** Results of the CRS stack processing obtained along Ja1 horizon: (a) CMP hyperbolic search and radius of $R_{NIP}$ wave, (b) linear ZO search and the value of normal ray $R_N$, (c) ratio of $R_{NIP}/R_N$. Missing values are masked in gray.

Figure 5.10 of the corresponding coherency cross-section proves its usefulness helping with the fault identification due to its higher values. In the coherency attribute the amplitude of the signals along the structural or time horizon are observed in order to find discontinuities within the amplitude field that are towards changes within structural characteristic of the formation (Klein *et al.*, 2008). Coherency attribute belongs to the group of a post-stack attributes that measures the signal continuity and are often used to delineate structural features like faults, channels, etc (Bahorich & Farmer, 1995; Marfurt *et al.*, 1999).

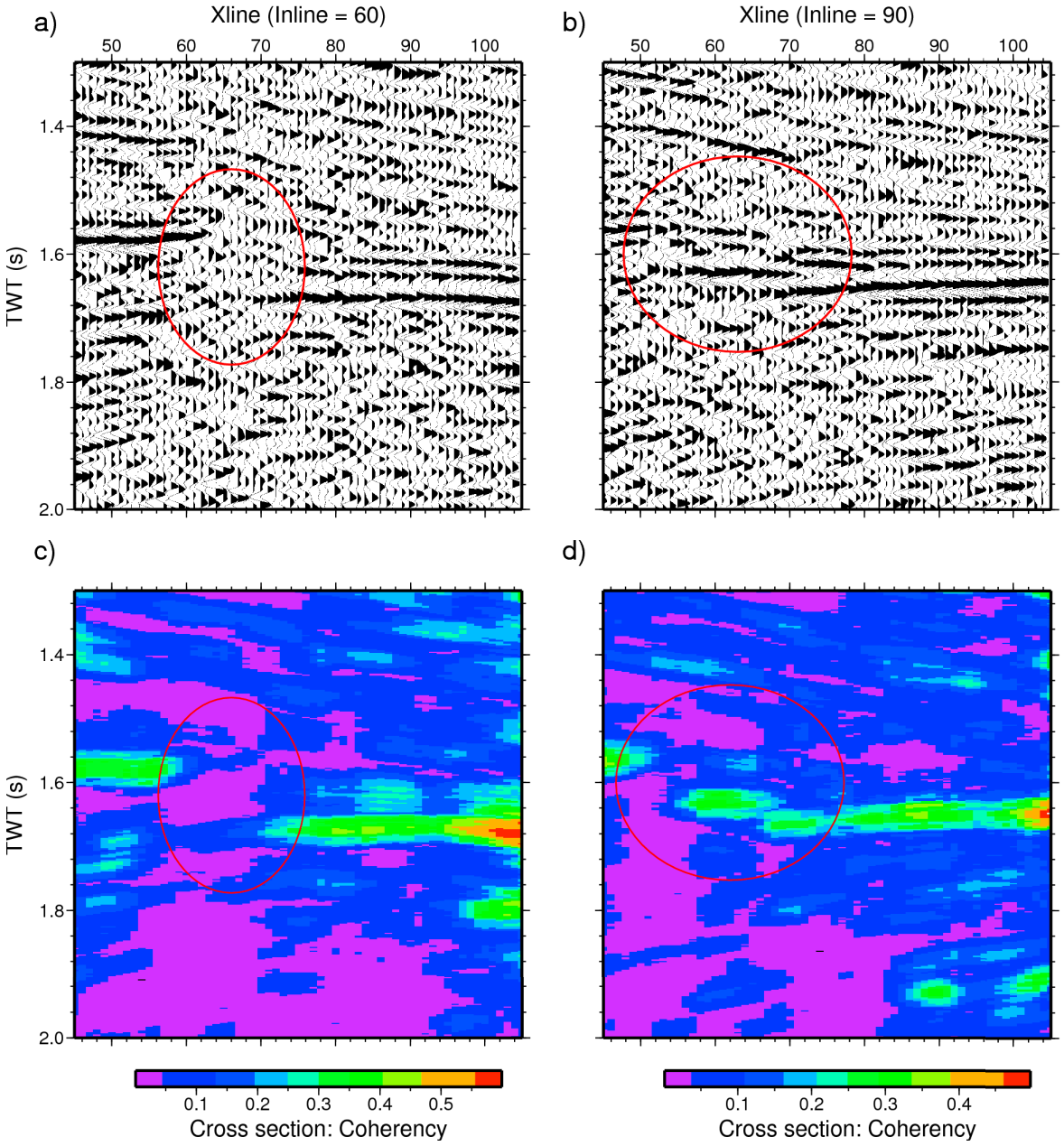


**Figure 5.10:** Seismic cross section obtained from CRS stack (top) and corresponding distribution of coherency attribute (bottom). The structural discontinuities observed along Ja1 horizon are indicated by red ellipses.

Images presented on Figure 5.10 show two seismic cross sections obtained along in-line 60 (a) and 90 (b), that were acquired with the use of standard CMP processing sequence described on Fig. 5.6. The corresponding distribution of the coherency at-

tribute obtained from the CRS processed sections are presented at the bottom (c,d). Areas marked by the red ellipses indicate the discontinuity of structural elements that were already recognized as two faults (see Fig. 5.11). The section that goes along inline 60 crosses the main fault showing the broad zone between hanging and footwall. The same results can be observed on the corresponding coherency section where Ja1 horizon is marked by the highest coherency values. More interesting results are visible on the cross section obtained along inline 90 where it goes through the main unit and the smaller fault. Similar to the cross section of inline 60, the coherency image perfectly match the location of Ja1 horizon.

The full spectrum of the CRS stack application is far more wider, but many aspects of the CRS processing have been neglected due to the limited range of this thesis. As a supplement to recent developments, describes in the section 3.3, it is worth to mention others that are of particular importance. For instance due to the flat survey area and a homogeneous 3D acquisition, the aspects of elevation variations and its influence on time shifts and static correction that has been extensively described byHeilmann *et al.* (2006); Zhang (2003) and Koglin (2005) were omitted. Another important problem of nonuniform and arbitrary land acquisition geometries has been discussed by Boelsen & Mann (2005) was also not implemented it this thesis. It is worth to mention that as the results of these developments CRS method has been successfully adapted to the ocean bottom seismic (OBS) and vertical seismic profiling (VSP) acquisition geometries. Another optimization aspect, consisting of a 2D CRS stack series performed on restricted azimuth, described by Höcht (2002) however efficient in respect to the o computational cost, was not applied d to heterogeneous distribution of azimuths. In the next paragraph I will present the investigation on seismic signal attributes analysis acquired from conventional and the CRS stacking method mapped across Ja1 horizon within the 3D stacked data volume.

## 5.5 Analysis of seismic signal attributes

Seismic data volume usually contains particular information that can be extracted by the analysis of seismic signal attributes, which allows to acquired an additional characteristics of the subsurface. Additionally, seismic attributes are used to enhance an image of structural features that helps to characterize reservoirs parameters or provide information about media content accumulated within a sedimentary succession

(Chopra & Marfurt, 2007; Neidell & Taner, 1971; Taner *et al.*, 1979). Attributes are obtained from data cube over a time, depth or horizon within a specific time window. Usually they describe signal characteristics or structural properties as well as its statistics (Chopra & Marfurt, 2005; Taner, 2001).

Although the number of developed attributes still expand and many new were evaluated since the introduction, there are only a few that have strong foundation and relationship to the a physical properties of seismic signal. There are even many of seismic attributes that can be seen as excessive or their application do not bring any improvements, thus even make the interpreters even confused (Chen & Sidney, 1997; Taner, 2001).

Generally, signal attributes are determined by the mathematical operation on amplitude, frequency or their spatial distribution, however, some specific information can be provided by the use of multiple attribute apprach and/or its particular combination. Seismic datasets may gain profits in the frame of structural interpretation, where several attribute of seismic trace are extracted and evaluated. In this study, the attribute analysis will focused on the application of the three attributes that can serve as a base of signal characteristics classification.

In order to get the most benefits from the signal attribute analysis on Skierniewice site, input dataset were prepared in the form of horizon picks. The selected Ja1 horizon was picked manually within the stacked data volume. Special attention was given the check the quality of picked horizon, where both in-line and cross-line grid orientation were considered. The distribution of two-way-time picked zero–offset reflections obtained for horizon Ja1 is presented on Fig. 5.11.

The amplitude response of Ja1 horizon showed the presence of three distinct zones. Its major border (marked by dashed line in Fig. 5.11) was identified as normal fault of N330 azimuth that divides the structure on two parts. Southwestern part forms the hangingwall, whereas the northeastern a larger block, shows an additional minor fault of azimuth of N105. Proposed division remains in compliance with the fault interpretation that was presented by Bujakowski *et al.* (2010).

Acquired picks of Ja1 horizon (Fig. 5.11) were used as the reference basis for the attribute analysis. The selected attributes: root-mean-square (RMS) amplitude, instantaneous frequency (Taner *et al.*, 1979) were successively calculated within +/- 20 ms time window centered on amplitude peak derived from Ja1 horizon (see Fig.5.12). The selection of window length based on signal characteristics that is equal to one period

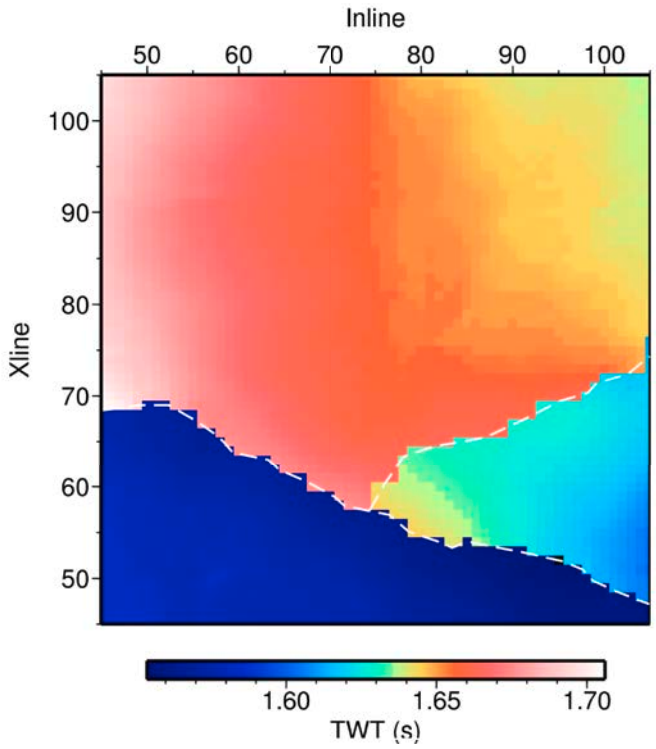


**Figure 5.11:** Distribution of the zero-offset two-way-time for the Ja1 horizon obtained within the study area.

of the waveform of that horizon. Larger window length caused inappropriate attribute determination influenced by the neighborhood horizons due to their close location. Figures presented later in the this section, will show the attribute images calculated along the Ja1 horizon acquired from both the NMO and the CRS stacking volume.

The attribute of RMS amplitude which can be seen as the smoother version of reflection strength (Barnes, 2007) is often used as first order and important indicator of bright spots and comprehensive amplitude measuring tool. Its usage is dated since the 1970' (Hammond, 1974) where it was found that the structural traps containing hydrocarbons can cause such anomalies within a seismic dataset. In seismic, it enhances significantly the changes in acoustic impedance over the particular time interval. In general, when consider compacted lithologies that can be matched by particular seismic resolution, higher RMS values towards the higher acoustic impedance variation. Thus, the RMS attribute is useful tool in reservoir mapping and serves as a direct hydrocarbon indicators or due to lithological characteristic can indicates structural deformation zones. It is worth to mention that the direct application of RMS amplitude attribute

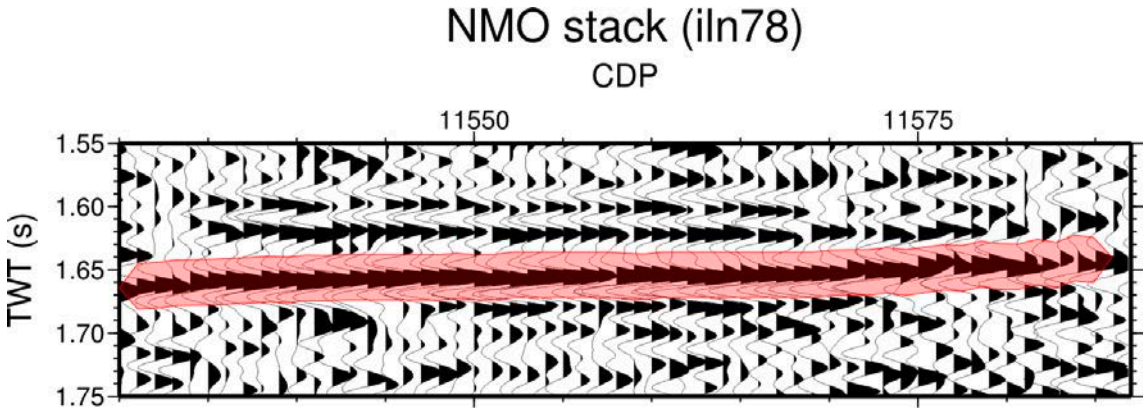


**Figure 5.12:** Window length used to determine seismic attributes along Ja1 horizon.

is sensitive to noise as it squares every sample within the measured window. Since no true amplitude processing was applied in this study, the interpretation of amplitude-related attributes must be carried out with caution (Yilmaz, 2001). RMS amplitude variations can be discussed only qualitatively. Figure 5.13 shows the attribute section obtained from the picked Ja1 horizon. The applied +/- 20 ms time window allows to identify clearly the main fault zone on both processed images which is corresponding to the structure observed on picked travel-time section.

Although the attribute of RMS amplitude derived for NMO processed data (Fig. 5.13a) shows similarity to the travel time section in respect to the main fault structure, however the smaller fault has not been visualized clearly, making the interpretation more difficult. The structure located on the eastern side to the major fault, hence is more compact it shows non-uniform distribution of the attribute values. The CRS processed data (Fig. 5.13b) shows similar structure to that of travel time but instead to the CMP processed image the attribute section of RMS amplitude consists of three individual units separated by the channel composed of low values. The structure located on the western side reaches its maximum values in the form of elongated structure parallel to the fault edge within its close vicinity. The shape of its maximum forms the edge and also shows a slight rotation relative to the isochrone curves of the picked horizon (see Fig. 5.13b). Additionally it becomes more distorted with the distance from the fault edge. The southernmost unit has the maximum of the attribute in the form of elongated structure parallel to the fault edge, located close to the smaller fault. The largest, northeastern unit has been imaged is composed of two elongated structures connected on the east, forming a bay-like area of the low attribute values. Additional

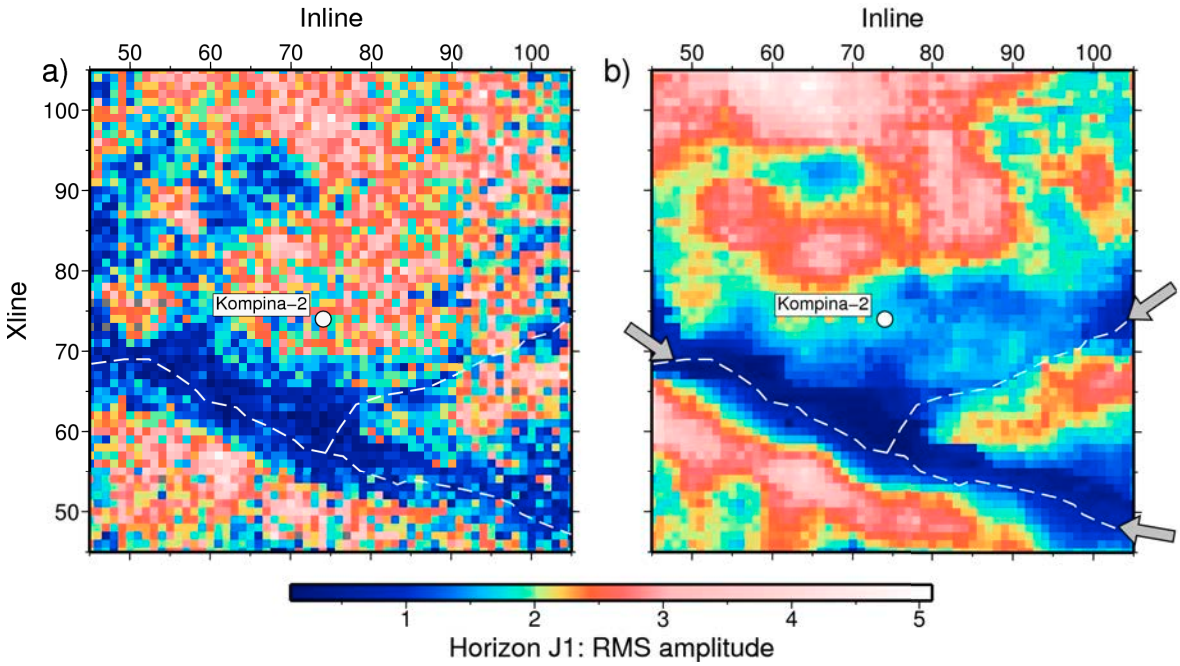


**Figure 5.13:** Comparison of seismic signal attribute analysis performed on Ja1 horizon acquired from CMP and CRS stacked seismic volume. The attribute of RMS amplitude was calculated along Ja1 horizon within the window of +/- 20 ms. Gray arrows indicate fault structures identified on Fig. 5.11

island of moderate values is located on its southeastern side. All these structures are significantly moved away from the fault edge and due to higher values may indicate both the increased porosity or the presence of hydrocarbon.

The Ja1 horizon was processed within the same window length for both NMO and the CRS processed datasets. The results of the comparison can be seen at first glance where the image of the CMP stack (Fig. 5.13a) looks more noisy than the CRS processed (Fig. 5.13b). The CRS shows depicted structure more clearly and overall quality is much higher while the three high amplitude anomalies are characterized by continuous shape. These structures are separated by wideer zone of low attribute values which is in conformity with fault observed on travel time image. Although the major fault can be distinguish on both image, however the detection of a minor fault is obvious only on the CRS processed stack.

Low values of RMS attribute derived for the Ja1 horizon composed of sandstone may indicate increased porosity, thus suggesting higher fluid saturation. This was confirmed during drilling operation when outflow of geothermal water has been recorded

(Bujakowski *et al.*, 2010). Additionally, the lowest value of RMS attribute may confirm the presence of fault zone since it represents mainly the weak acoustic impedance contrast. Since the highest amplitude values can be seen as direct hydrocarbon indicator (Chopra & Marfurt, 2005; Hammond, 1974; Taner, 2001), the recorded outflow of geothermal water from Kompina-2 well Bujakowski *et al.* (2010) can be correlated undoubtedly with moderate values of obtained RMS attribute in borehole location as it is located in close vicinity to the highest amplitude anomaly. Those zones of higher RMS attribute values was identified by Pussak *et al.* (2014) as compacted sandstone of less fluid content due to higher P velocities and indirectly the facies variations.

The attribute of instantaneous frequency is a first derivative of instantaneous phase attribute and is usually applied to identify thin-beds tuning effect and enhanced the abnormal attenuation along the reflector (Bahorich & Farmer, 1995). It also helps to detects gas saturated beds with abnormal low frequency values instead of high RMS amplitude (Chopra & Marfurt, 2005).

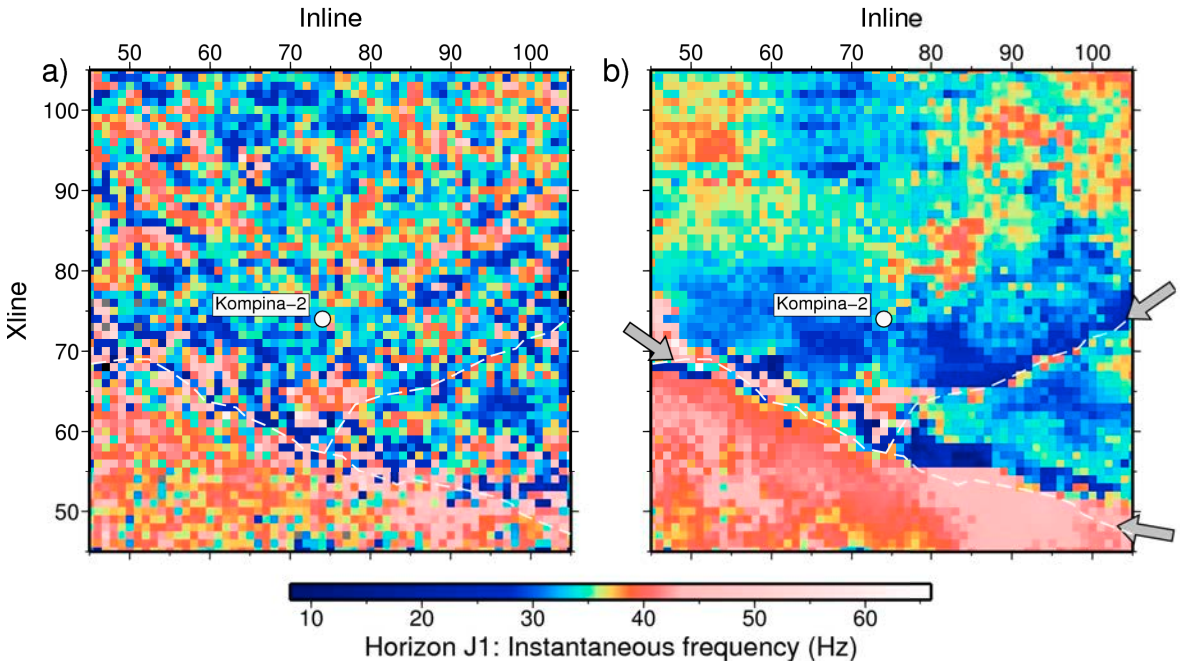


**Figure 5.14:** Comparison of seismic trace attribute analysis performed on Ja1 horizon acquired from NMO (a) and CRS (b) stacked seismic volume. The attribute of instantaneous frequency was calculated along Ja1 horizon within the window of +/- 20 ms. Gray arrows indicate fault structures identified on Fig. 5.11

The results of instantaneous frequency attribute derived from Ja1 horizon is presented on Figure 5.14. Similar to the attribute of RMS amplitude the time window length was selected to contain the whole signal of accompanying seismic horizon. The image derived from NMO processed data (Fig. 5.14a) allows to distinguish two areas separated by the fault of N330 azimuth. The area located on the western side is composed of the homogeneous high frequency body with average frequency of 40 Hz. Its boundary that runs over the fault is characterized by heightened frequency. The eastern part consist of noisy area with hardly visible structure of mixed frequency, where the identification of smaller fault is not possible.

Figure 5.14b shows the results of attribute derived from the CRS processed volume. Instead of CMP stacked data, the CRS volume contains clearly visible structure with evenly distributed frequencies. The western block is dominated by high frequency attribute values of above 40 Hz while the transition to the eastern block is characterized by rapid decrease of frequency which delineates the fault pattern as very sharp edge. Frequency values of about 35 Hz are typical for the eastern segment showing additionally three distinct and separate zones of higher frequency. Special attention deserves to the smaller fault which edge can be easily traced due to its high values of frequency.

The comparison of instantaneous frequency attribute performed along Ja1 horizon from the CMP and CRS stacked section shows a large similarity to the RMS attribute but differences between images are more evident. The CMP stack (Fig. 5.14a) allows to determine two zones of different frequency separated by the border going over the faults line, however the image is more noisy and its general quality is far away from the much better imaged CRS stacked section (Fig. 5.14b). The CRS provide very clear image of two blocks with perfectly matched major fault determined by sharp border between these two units. An additional structure of minor fault is also mapped, however, its acute transition is marked by a thin line consisting of high frequency values. Such a sharp border of the frequency are usually connected to bed thickness or indicating edge of low impedance thin beds (Chopra & Marfurt, 2005).

Since the instantaneous frequency shows its discrimination features due to the propagation effect and the depositional characteristics (Taner, 2001), the area located in the close vicinity of two faults allows to determine the degree of tectonic activity due to its lowest frequency values. This is visible especially where two of the faults are connected showing the anomaly of the lowest frequency value which is obvious due to the biggest deformation occurred in that area. The lower frequency values located in

close vicinity of Kompina-2 well can be seen as bed thickness indicator where lower frequencies may suggest a sand rich bedding, while on the other side, the lowest frequency values recorded along faults plane can be seen as the fracture zone indicator (Barnes, 2007, 1991; Taner, 2001).

# 6

# Discussion and conclusions

In this thesis, a method for the improvement of seismic trace attribute quality has been presented. The method is based on the application of the Common Reflection Surface stack to prestack reflection data sets acquired from sedimentary basins. Instead of conventional CMP stack, higher S/N ratio obtained from the CRS sections/volumes allows to illuminate the structural elements with better accuracy. In consequence, results of CRS imaging are used to enhance the seismic trace attribute calculation, thus providing significant improvements in geothermal exploration campaign and help in the determination of exploitation parameters at higher confidence level.

Imaging of seismic trace attributes acquired from CRS volume allows to indicate potential zones for geothermal exploitation. The RMS amplitude and instantaneous frequency attributes obtained from the CRS volume show higher quality when compared to their CMP counterpart. Improved structural imaging performed in the close vicinity of fault zones and its further lithological interpretation based on attribute determination may significantly decrease drilling risk in further geothermal projects.

The method was tested on real data sets acquired from two sedimentary basins, where different layouts of reflection seismic surveys were applied. The 2D seismic reflection sections were obtained from the Alberta Basin within the Lithoprobe project, whereas the 3D volume was acquired in the Polish basin within the I-GET project of $6^{th}$ EU Framework Programme. The remaining part of the chapter shows the most important improvements and conclusions within the CRS processing and seismic trace attribute calculation.

## 6.1 Improvements of stack images

### 2D seismic, Alberta basin

The Lithoprobe seismic reflection data (Eaton *et al.*, 1995) presented within the thesis consists of seven active seismic reflection lines of about 500 km total length acquired within the Central Alberta Transects stage. The project was originally aimed to provide the structural characteristics across the Western Canada Sedimentary Basin (Hope *et al.*, 1999) and deep crystalline basement. The acquisition parameters where determined upon the strategy of deep basement imaging (see Table 4.1)) and allowed also to highlight reflections from a sedimentary succession. In order to ensure the penetration of very deep targets, the Vibroseis source was spaced at 100 m in asymmetric split–spread layout over the large offsets up to 12 km length, while the seismic lines crossed perpendicular the basement domains borders. Such a setup, highlighted the very deep structures at expected resolution. The illumination of the shallower part allowed to image the sedimentary succession only with moderate resolution, mostly due to limited range of frequency content.

In the frame of the thesis, seismic data processing was performed within 2.0 s TWT in order to provide structural images of the Alberta Basin with emphasis in development of further geothermal exploration strategies. The investigated area can be characterized by a regular subsidence process, undisturbed by far located tectonic units and dominated by unique continuity of reflected horizons over regional scale. Generally, as presented in Section 4.5 (see Fig. 4.9–4.15), the processed data show lateral homogeneity and continuous character within the sedimentary section, while holding the consistency in vertical scale.

The top of the basement structure was depicted at 1.5-1.8 s TWT separating the sedimentary succession from the low S/N image of the crustal zone, which is additionally affected by multiple reflections. The undulating trend of the south-west dipping monocline has shown a particular diversity in amplitude distribution across the cumulative transect line. Its characteristic and correlation with respect to the location of tectonic domains (see Fig. 4.1) will be discussed in the next section of attribute analysis.

Figure 6.1a-c presents a selected example of stacked seismic line obtained with CMP and CRS stack technique. The high quality image of CRS stack section has shown its unique imaging capabilities with comparison to less quality reflections obtained from

CMP counterpart. Independence from a given velocity model and rather small human interaction, belong to the advantage of the CRS method.

Reflection events shown on Figure 6.1a can be easily distinguished on the basis of exceptional continuity, visible only on the CRS stack section. Additional structural feature of stratigraphic element, recorded on the right side at 550 ms TWT, could be interpreted as apparent onlap simulated by further tectonic movements. It is worth to note that an overwhelming number of minor stratigraphic interfaces, visible between 500 and 600 ms TWT show its continuity on the CRS image. Figure 6.1b can be seen as an example of the unique feature of the CRS method, where redundancy of the seismic traces is used to fill gaps in the shallower parts along stacked section. These gaps are often visible for shallower parts of the CMP stack due to insufficient number of traces with short offsets. Another improvement is shown in Figure 6.1c where noisy CMP stack image can gain from the CRS technique. In this example the CRS stack shows not only the overall improvements in signal characteristic and reflection continuity, but also reveal the tectonic patterns that can be interpreted as a small listric fault (visible on the right).

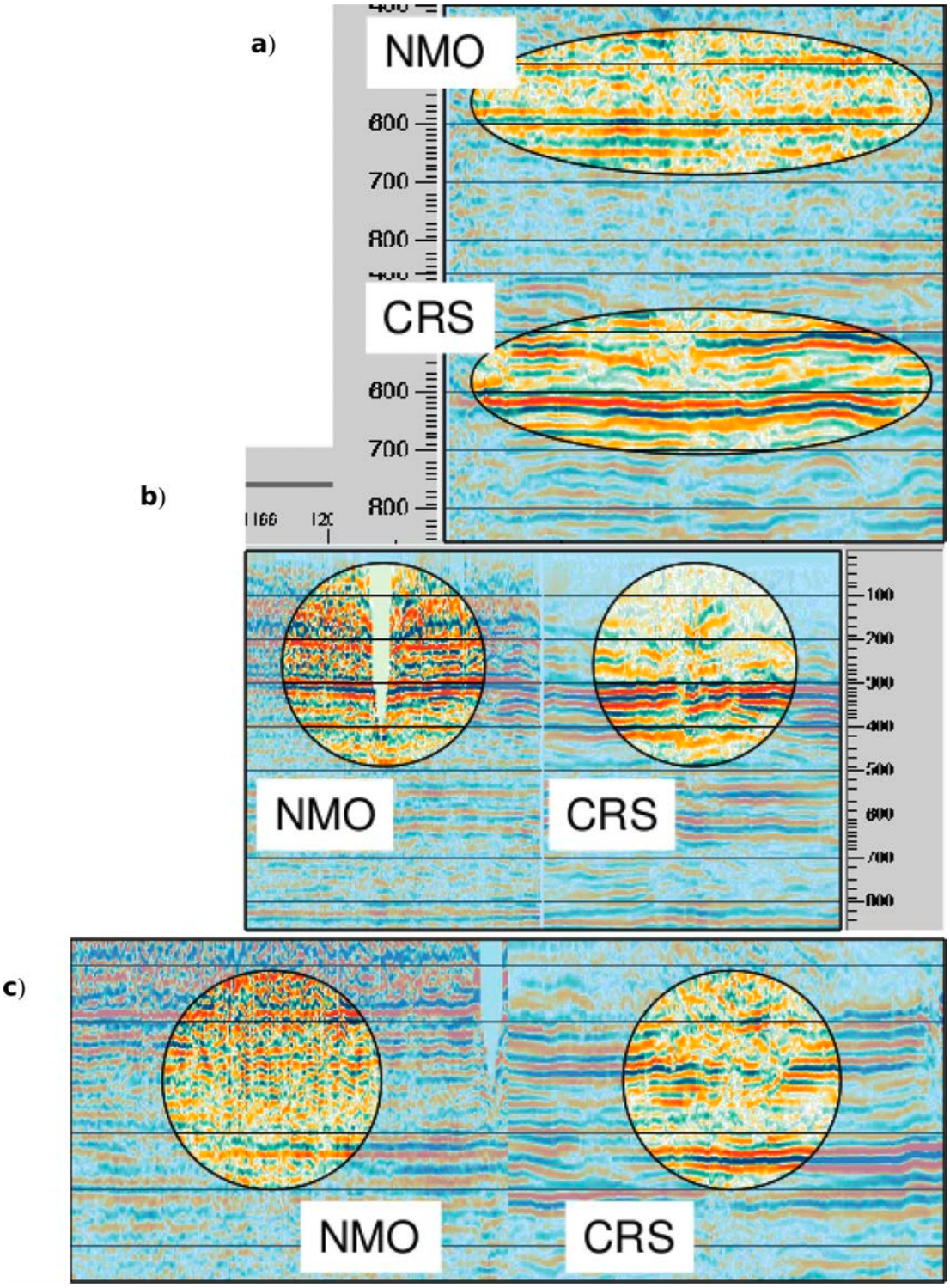


**Figure 6.1:** Examples of CAT profiles showing improvements in the CRS stack over CMP counterpart. Imaged reflections are more precisely and have better continuity, moreover, even small events, recorded at are imaged.

### 3D seismic, Polish basin

Seismic reflection data set, recorded in the central Poland that geologically belongs to the Polish basin formation (see Fig. 5.1) were collected to perform the structural analysis of the selected geothermal horizon that host within the Mesozoic sedimentary formations. The acquisition geometry based on grid layout, with the well Kompina-2 located within its center. The log analysis from that borehole (see Fig. 5.3) indicates the presence of geothermal waters within the Lower Jurassic aquifer. Seismic data were acquired with the use of Vibroseis technology on the area characterized by a flat topography. The layout consisted of six source lines oriented in the grid form where three parallel lines spaced at 1 km were oriented perpendicular to the three others. Six receiver lines followed the source lines orientation, whereas two supplemented lines crossed the well Kompina-2. The signal from four Vibroseis trucks was generated at 252 locations and recorded by 1390 geophone groups that resulted in about 350 000 traces in total (see Sec. 5.2 for further details). Signal quality is high on all shots and reflections from sedimentary succession were observed down to 1.5 s TWT. Although the geometry layout of the survey allowed to obtain high coverage factor along source lines the fold breaks down in between. Thus, the obtained seismic data in a sparse acquisition were suited well (Trappe *et al.*, 2005) to perform the CRS processing and in order to enhance the S/N ratio.

The collected dataset, prepared in the form of preprocessed CDP gathers, were used for both CMP and CRS stack methods. Within the CRS stack processing work flow, eight kinematic wavefield attributes are obtained as well as the resulting CRS staked ZO volume. Although the wavefield attributes contain the information that can be used to perform the velocity inversion, a simultaneously eight-parameters search procedure is the hard task even for nowadays computer centers. Therefore, in order to conduct the search strategies within reasonable time frame, the complete evaluation of the attributes is performed as the one-parameter search split into three steps. The final step that is based on the constrained optimization provides the CRS staked ZO volume. Figure 6.2 presents the results of the stacked CMP and CRS method.

Seismic processing using the CRS has shown its unique features to produce high quality image of stacked seismic data volume. This method, which has a limited human interaction and independence of external velocity model allows to obtain an image of higher S/N ratio where reflection events are characterized by better continuity when

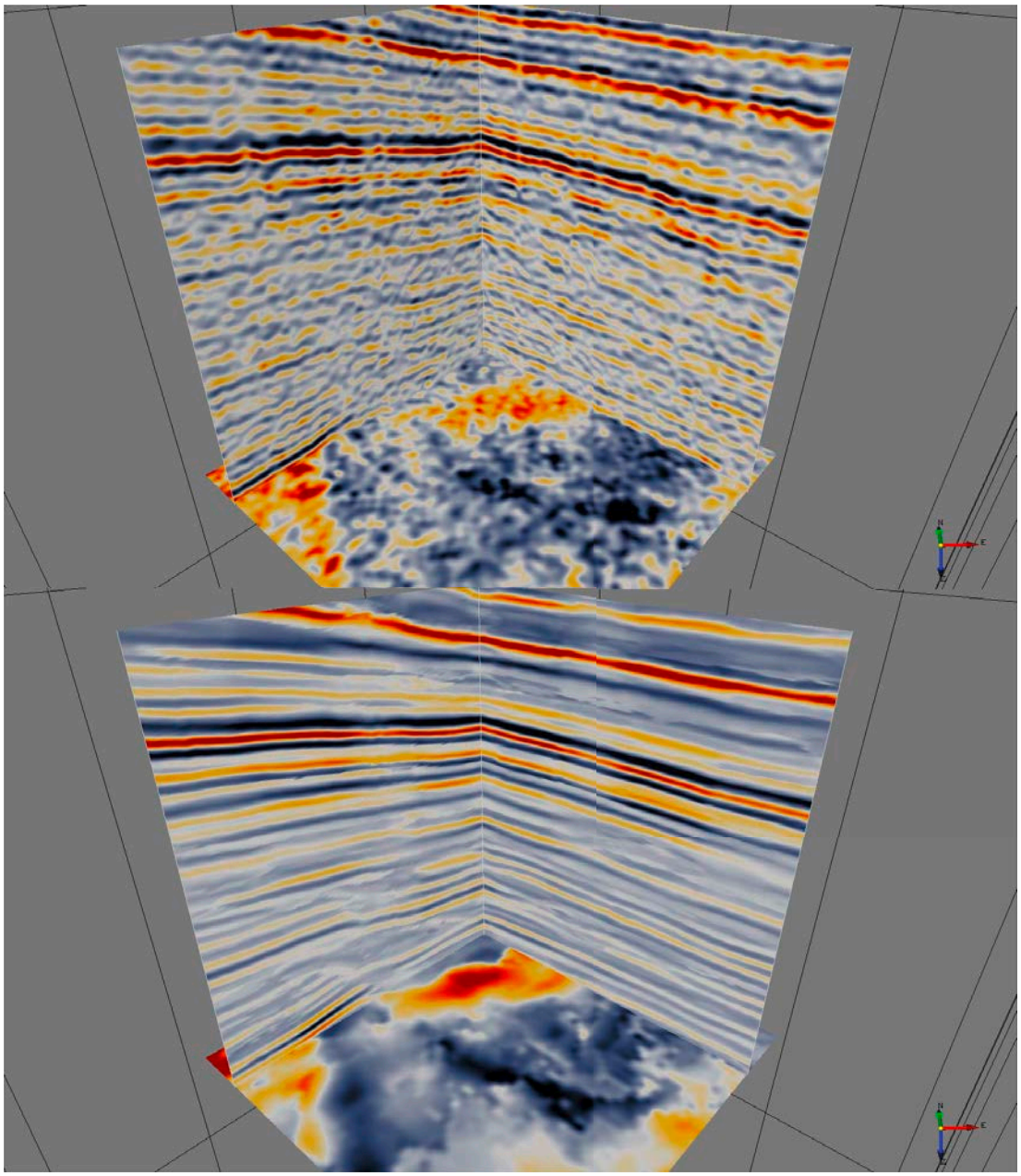

**Figure 6.2:** 3D seismic volume showing the stacking results obtained with CMP (top) and CRS (bottom) method. The overall signals quality and continuity of reflection is much higher on CRS processed data.

compared to the conventional CMP stacking technique. Additionally, the secondary outcome of the data processing are bundle of CRS attributes estimated during the automatic searches. These attributes are particularly useful for depth migration tech-

nique, where depth velocity model is acquired by the NIP-wave tomographic inversion Duveneck (2004).

A high quality volume provided by the CRS stack method proved that the structural setting of investigated geothermal site can be revised at higher confidence level when compared to the conventional CMP technique. Acquired time-domain reflectors of higher S/N ratio allows the horizon to be picked more easily and accurate. Figure 6.2 clearly demonstrates that the capabilities of low-fold data can be gained to the level comparable with an image of higher fold data processed with conventional CMP method Buness *et al.* (2014); Pussak *et al.* (2014). Additionally, the CRS method is particularly suitable in the area located in the neighborhood of salt domes where conventional velocity building methods can not achieve of the required reflections accuracy due to limited coverage Baykulov *et al.* (2009).

The sedimentary succession within the investigated area was imaged down to 2.5 s TWT, with the special focus on Ja1 horizon which corresponds to 2.7 km depth. The structural interpretation of CRS stacked seismic volume allowed to distinguish the Ja1 horizon more precisely, while the remaining reflectors at shallower depth also show higher continuity compared to the conventional CMP stack. The time slice shown in Figure 6.2 that pass through the horizon allowed the fault system to be imaged more precisely within tested apertures. Moreover, more structural elements were recovered in correspondence to rather scattered amplitude distribution within the CMP volume. In consequence, manual picking performed in both in-line and cross-line direction can be performed at higher confidence level.

In the thesis special attention was undertaken to highlight the reflection event of the most favorable horizon from geothermal exploration perspective. It is worth to note that improvements within the CRS volume strongly depend on selected apertures, thus imaging of small scale structural discontinuities within the horizon may need special parameters selection focused on investigated targets only. In the results of this tradeoff solution other targets will require different apertures whose sizes do not meet criteria of equality in relation to Fresnel zone selected for the main target. Nevertheless, the CRS method provides advantageous results in geothermal projects of limited budget when the target zone is known i.e from reprocessing of archive data (Buness *et al.*, 2014).

## 6.2 Improvements of attributes and interpretation

### Alberta basin

The Central Alberta Transects (CAT) of about 500 km length spans over the basement body composed by five different crustal domains (see Fig. 6.3) originated in a series of Paleoproterozoic crystallization processes that were aggregated about 1.8 Ga (Mossop & Shetsen, 1994; Ross *et al.*, 1991). Potential field data and a limited number of boreholes intersecting the basement outcrops were used to identify regional patterns of those domains (Hope *et al.*, 1999; Ross & Eaton, 1999; Ross *et al.*, 1995). Although the reflection seismic method is capable to identify these structures with sufficient resolution, seismic attributes analysis may also play a critical and complementary role providing a new insight to the lithological differentiation. The RMS amplitude and instantaneous frequency attributes were used to identify and characterize four structural markers (see Fig. 6.3). Beside the identification of structural patterns, attributes allowed to determine the interrelationship between basement and overlying Paleozoic sedimentary cover.

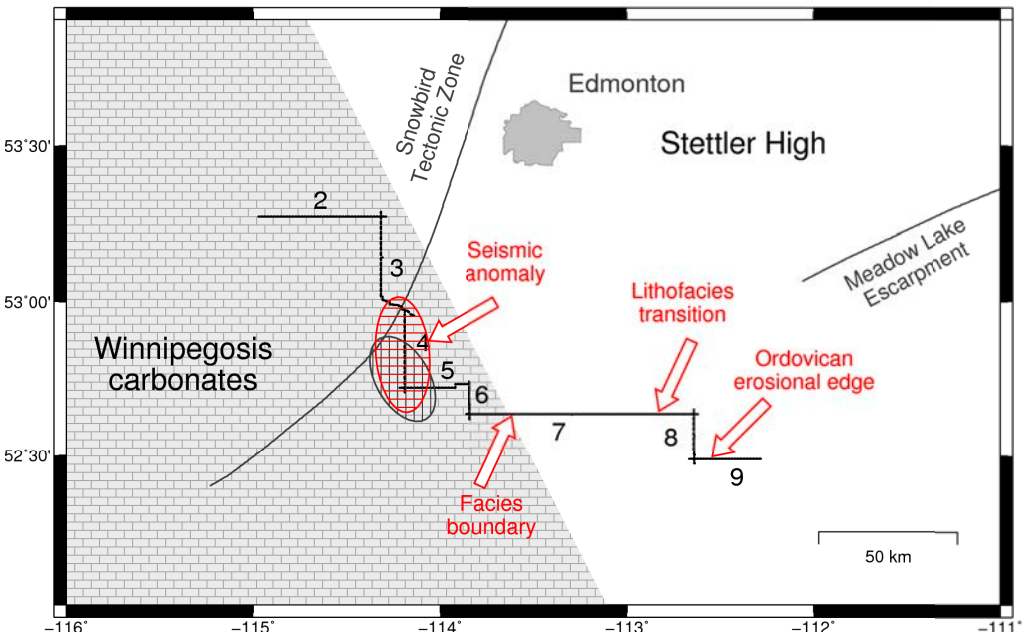


**Figure 6.3:** The lower Paleozoic structural features identified from seismic experiment. The lithological elements indicated by red arrows are described later in the text

As mentioned in Section 4.6, the attribute was calculated for each trace over the 200 ms window length located above the basement horizon. Although the CAT profile presented here consists of seven separate lines, however the individual intersection between lines formed a smooth transition of the attribute values from neighboring elements. The obtained data shows slightly scattering effect but still may disclose a number of potentially significant features. Figure 6.4a shows composite section of the RMS amplitude attribute calculated for both the CMP and the CRS stacked data.

In general, attribute values calculated along the CMP stacked lines do not differ significantly from that obtained by the CRS processing. Their spatial characteristics are similar in respect to the form like peak/trough location but the most visible difference concerns acquired values in particular segments along transects lines, thus making the comparison more clear. Four major segments can be distinguished along the profile that coincides with structural units identified on Figure 4.1. Borders between adjacent segments are characterized by a sharp decline in the RMS amplitudes which is significantly more evident in the CRS-based results. Such an effect is clearly visible at the end of line 3, close to the connection with line 4 and at the beginning of line 7. Further drops in the RMS amplitude, although not as much extensive, were recorded at the end of line 7 and in the middle of line 9.

The attribute values of RMS amplitude acquired along a composite section falls between 0.3 and 1.5, while its average does not exceed 1.0. The highest observed values were recorded in the form of maximum anomaly and traced along longer distance between line 4 and 5 reaching a maximum of 1.5 close to the lines intersection. An additional maximum anomaly was identified at the beginning of line 4 where the highest value of 1.4 was obtained. That tendency of higher amplitude disappears slowly along the rest of profile reaching the average value below 1.0 and containing a few local minimal anomalies observed on line 7. The RMS amplitude values calculated for line 9 show an increase at the end of the profile suggesting the presence of an additional geostructural element. The intensive variations of RMS values along line 3 to 5 probably reflect the presence of unconsolidated low–grade volcanic and sedimentary rocks (Hope *et al.*, 1999) due to strong velocity anisotropy usually observed within slate type of rock formation (Christensen & Mooney, 1995). The basement influence caused that these RMS amplitude variations are approximately twice the average.

The attribute of instantaneous frequency calculated for the same composite profile of NMO and the CRS stack is presented in Figure 6.4b. As can be seen, the profile is

dominated by an average frequency of 30 Hz showing anomaly peaks ranging from 20 to almost 40 Hz. Although considerable diversity in the frequency distribution make the detailed observation hardly visible, especially the differentiation between NMO and the CRS method, nevertheless it shows close correlation with the RMS amplitude distribution. There are two types of the frequency response that can correlate with even small RMS amplitude anomalies. The wide zones of minimum anomaly identified on RMS amplitude correlates with the minimum anomaly obtained for frequency attribute. This effect is visible especially at the end of line 3, 7 and line 9, where significant anomalies were observed. On the other side, there are high frequency anomalies recorded through out the profile which are correlated with decreased RMS amplitude anomalies. Such an effect can be observed on line 6 and 8 where high frequency anomalies are accompanied by a decreased RMS values.

As mentioned, the data processed with NMO and the CRS show some conformity based on location criteria along the CAT profiles, however their values differ substantially. In order to make the differentiation within attribute subset and between CMP and CRS stacked datasets more visible I used the crossplot method. The technique was introduced by White (1991) to indicate similarity within a group of attributes. Adequate selection of attributes may indicate the location of fluid bearing zones or similar lithologies as they merge into common groups, thus providing possible exploration parameters to the interpretation. The tentative insight into the crossplotting technique suggest that the trends between independently derived attributes should reveal additional structure which can be correlated with the unique features of particular horizons (Chopra & Marfurt, 2009; Michelena *et al.*, 2011). Such an indication was later used in AVO analysis based on the aggregations of attributes which did not belong into a specific cluster (Verm & Hilterman, 1995).

Figure 6.5 presents the crossplots image and the accompanying histograms obtained for RMS amplitude and instantaneous frequency attribute, derived for a better interpretation of anomaly identified on Figure 6.4. Histograms of both attributes obtained from the CMP stacked data (see Fig. 6.5a-b) show the arrangement of presented data in the form of normal distribution. A closer look, although not evident, shows slightly tendency to split calculated values into two clusters. Within the CRS subset such a division is obvious, and what is more important, the location of anomalies within the two attributes distribution match each others along the transect. These two well defined clusters show that the CRS may offer the solution related to the issues of lithological

differentiation more than CMP stack. Additional extension of the crossplots method to the three dimensional space or even use more recent methods i.e. SOM (Bauer *et al.*, 2012) may increase the readability of resulting images and improve the interpretation substantially.

As the supplement to the composite profile, attribute analysis was extended by additional crossplots of previously selected attributes acquired along three different horizons. Figure 6.6 shows signal attributes of the Second White, Pika and Precambrian horizons which were calculated within 40 ms window length. Although the Pika horizon does not reflect the interest in geothermal exploration, however is traceable through almost all transect lines, thus can be used as a reference horizon, while the others horizons may verify the heterogeneity of lithology at the intersection between basement and sedimentary layers along the composite profile. Since both images clearly differentiate three clusters, the attribute interpretation and their distribution can be performed rather in terms of quality. As one can see, more compact structure of the attribute distribution that comes from the CRS stack versus NMO counterpart may suggest easier lithological differentiation not only between particular horizons but also within one individual horizon. As illustrated on Figure 6.6, all clusters acquired from CMP stack are shown to be diffuse and widely scattered in comparison to their CRS counterpart. Moreover, the cloud of CRS obtained attribute allows to perform clustering in a wider range, by the differentiation within a single cluster and correlation of particular clusters with lithological features. Such an improved lithological response can also be correlated with AVO response, that are used to detect fluid anomalies (Waters & Kemper, 2014) or combine with prestack attributes for fracture characterization (Chen *et al.*, 2014) or adapt for more lithology oriented SOM analysis (Bauer *et al.*, 2012).

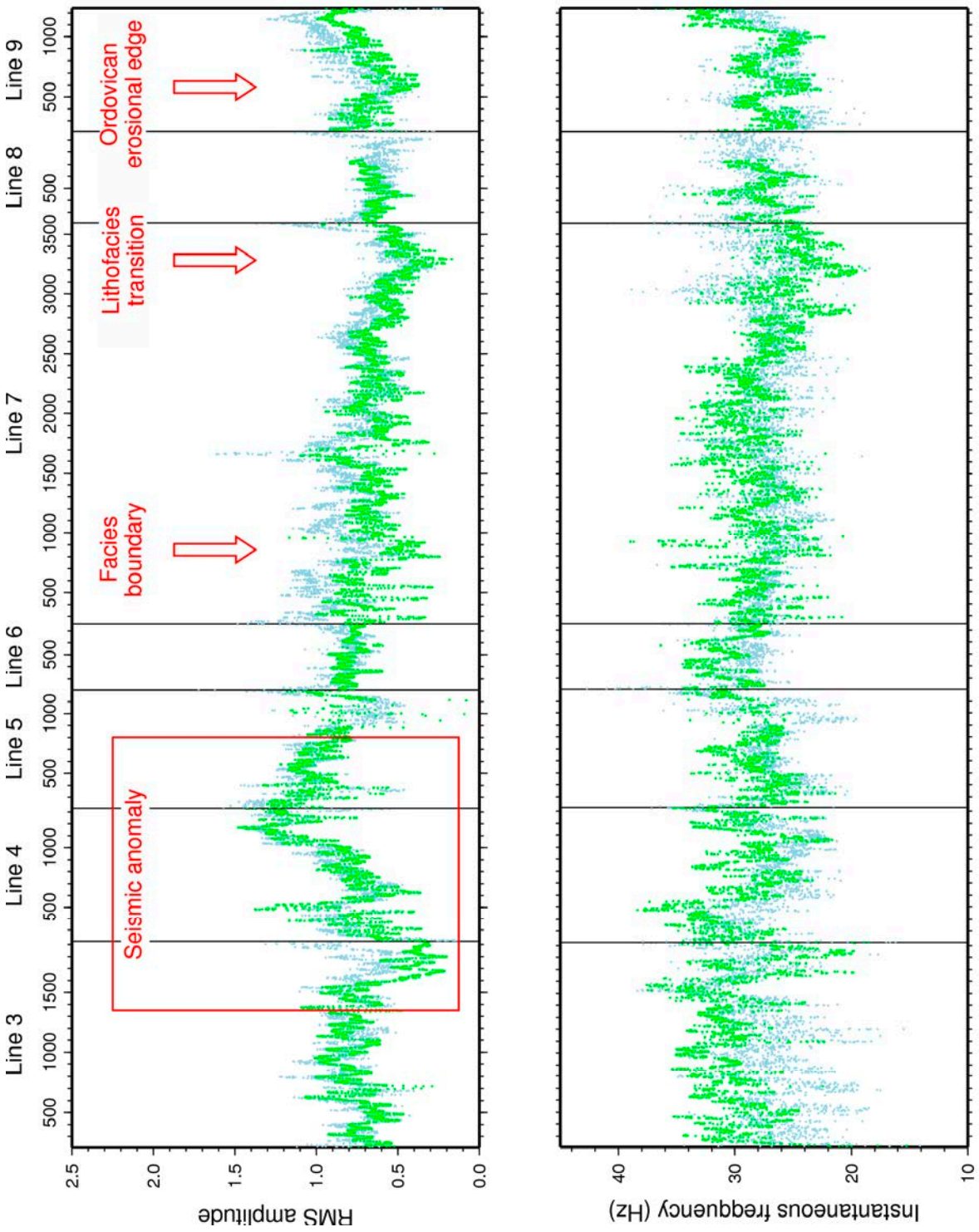


**Figure 6.4:** Selected profiles were processed with NMO (blue) and CRS (green) method. Afterwards, the RMS amplitude (a) and instantaneous frequency (b) were calculated within 200 ms window above the basement reflection event. The prominent events (marked with red color) correspond to the.

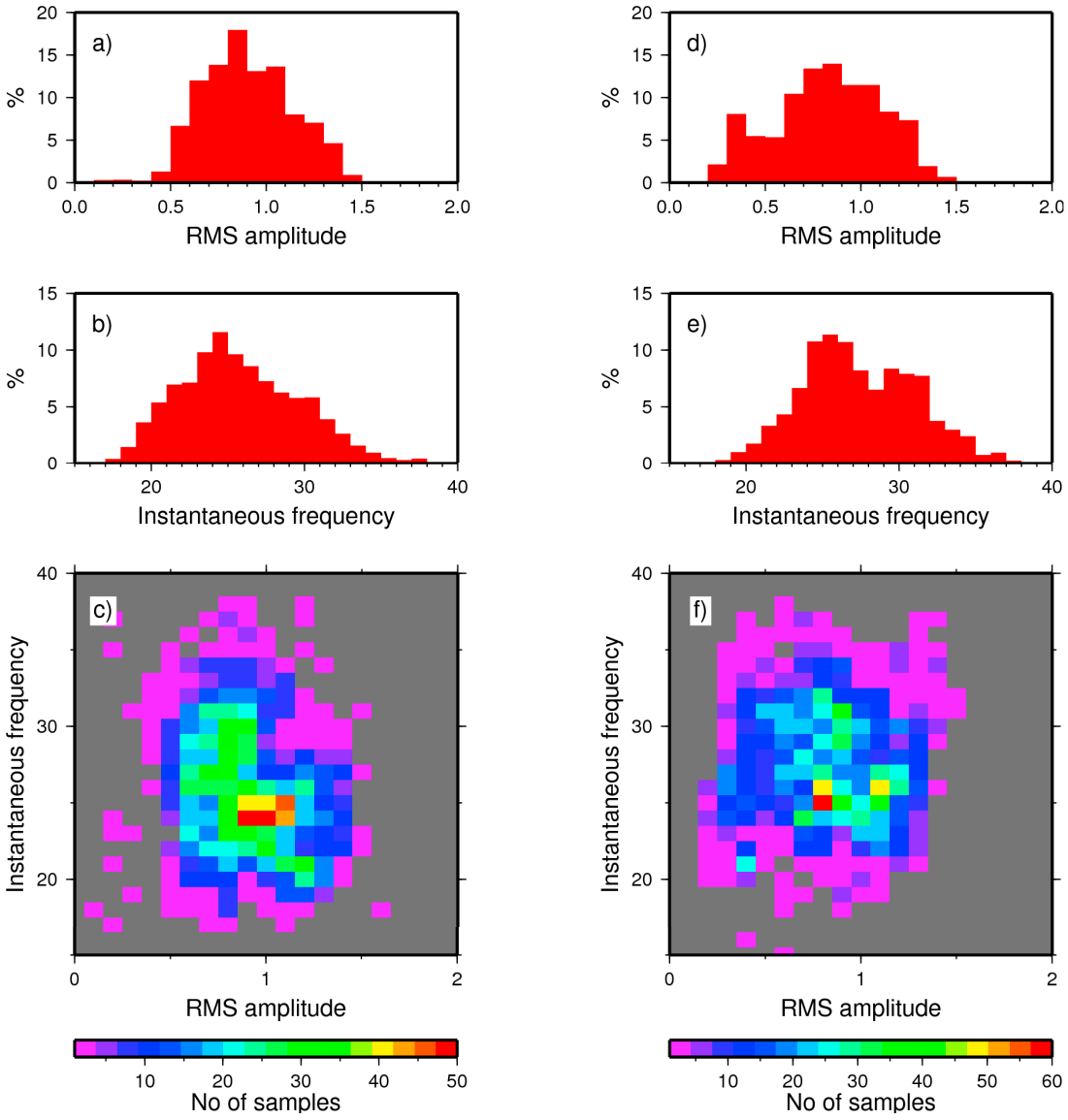


**Figure 6.5:** Histograms of RMS amplitude, instantaneous frequency attribute and their crossplot were calculated for NMO (a-c) and the CRS (d-f) processed data within 200 ms window length above the Precambrian horizon. The CRS images show two clusters instead of one presented on NMO. This can indicate more accurate lithological differentiation within event reflection from Stephen sandstone and Cathedral carbonate.

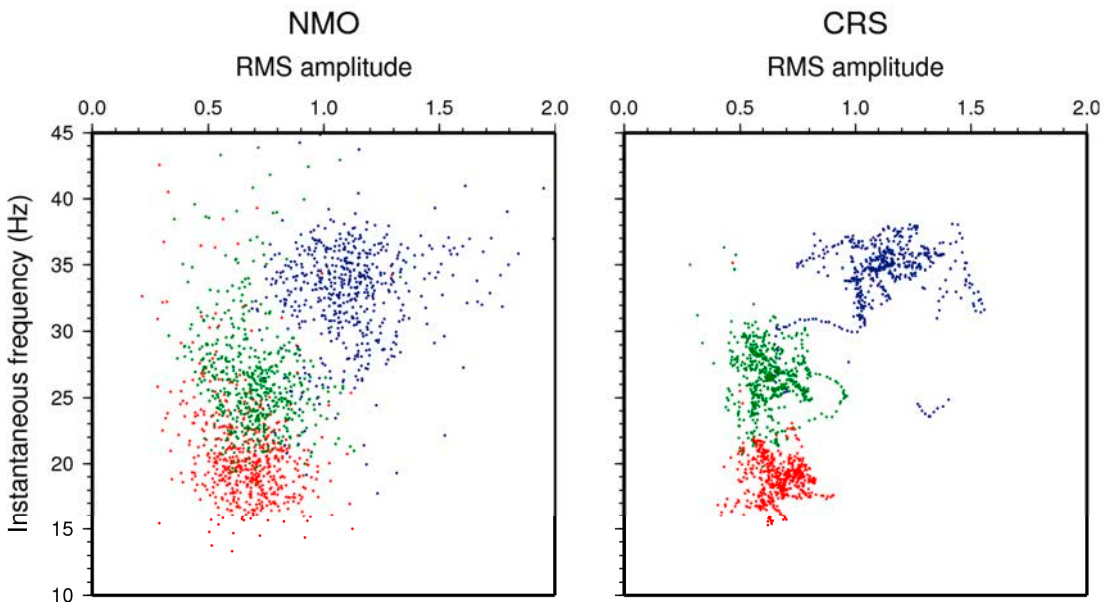


**Figure 6.6:** Crossplot of the RMS amplitude and instantaneous frequency attribute calculated for three selected horizon acquired from the NMO (left) and CRS (right) stack. The attribute were obtained from Second White (blue), Pika (green) and Precambrian basement (red) horizons within a 40 ms window length. Visible improvements in the attribute samples distribution from the CRS stack versus NMO stack show the CRS potential in differentiation of attribute characteristic that can be correlated with lithological features.

**Polish basin**

The seismic trace attributes were acquired from Ja1 horizon determined within 20 ms window length from both CMP and CRS stacked volumes. As indicated in Section 5.5 (see Fig. 5.13, 5.14) the attribute of RMS amplitude and instantaneous frequency obtained from CRS volume show higher quality when compared to the CMP counterpart. In addition, the attribute image of the CRS volume allows to indicate preferable zones that are of particular interest in accordance to the geothermal exploration. Identification of structural elements concentrated to the close vicinity of fault structures and their correlation with lithological information acquired from borehole may significantly minimize the drilling risk in geothermal projects.

I use the CRS stacked volume to show the spatial distribution of seismic trace attributes and their correlation to the lithological features based on information extracted from borehole Kompina-2. Image 6.7a presents the attributes of RMS amplitude and instantaneous frequency in the form of cross–plot showing clearly visible clusters marked with colored ellipses. Instead of self organizing maps (SOM) method used in Pussak *et al.* (2014)), that have shown its high potential in lithological differentiation I used simple cluster analysis based upon occurrence criteria (see Fig. 6.7b). Such a simple form of the clustering that is based on two input parameters only, nevertheless the good results are similar to the results obtained from SOM technique, however, causes that not every data are illustrated.

Generally, the occurrence of the largest number of attribute pairs allowed to distinguish four clusters. The correlation of borehole data with signal attributes may indicate a direct link between the highest RMS amplitude values of Class 1 with the presence of oil/gas because the rock samples for from Kompina-2 contained traces of hydrocarbons (Bujakowski *et al.*, 2010). Depicted in blue, Class 4 cluster is characterized by low RMS values (see Fig. 6.7c) and uniformly covering the entire spectrum of frequency (see Fig. 6.7d), that allows the fault zone to be easily correlated, moreover, the width of its close vicinity may suggest the extent of the corresponding deformation zones (Chopra & Marfurt, 2009). In addition, such a structural distortion when coupled with stratigraphic information forms the qualitative background for further facies analysis, as suggested by Chopra & Marfurt (2008).

An interesting conclusion can be raised for the Class 3 cluster that coincidences with Kompina-2 borehole location. Its rather low values of RMS amplitude and slightly higher frequency attribute values can be seen as the potential zone of geothermal

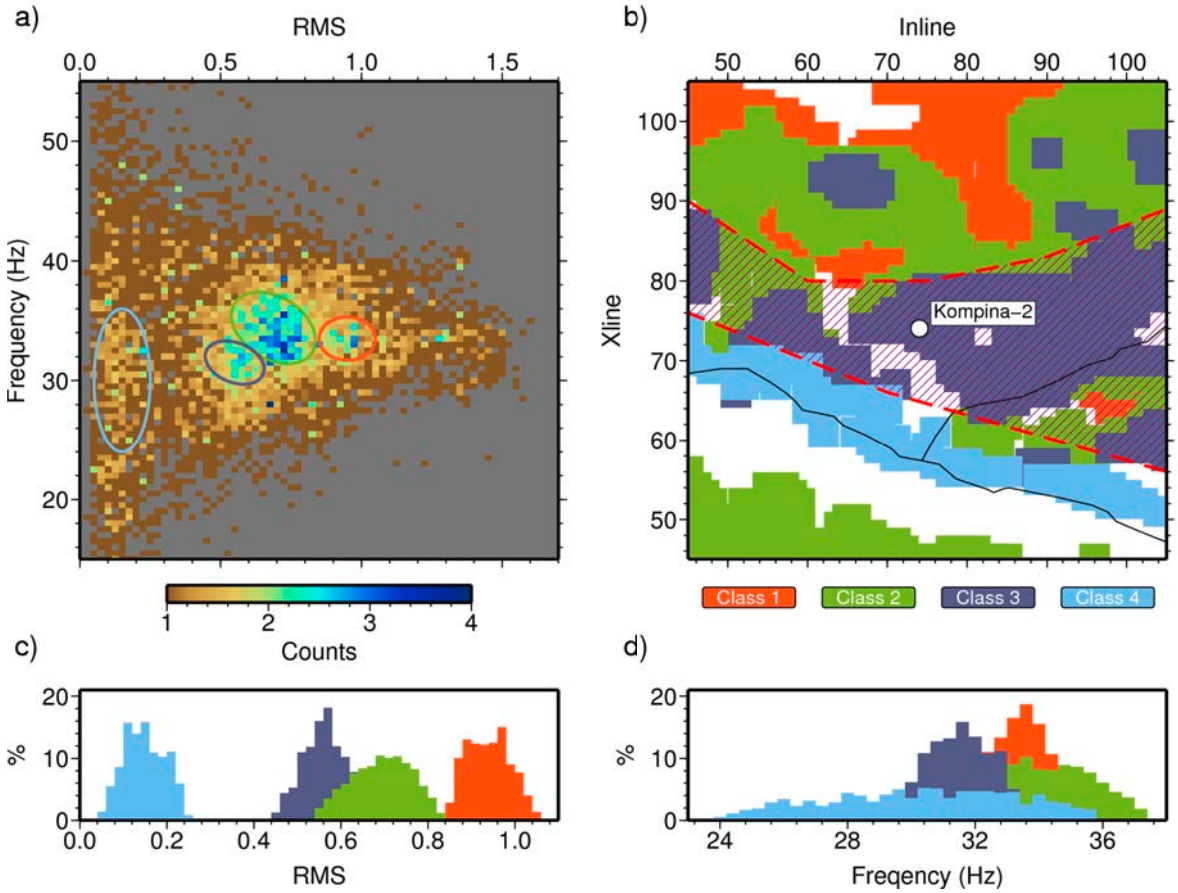


**Figure 6.7:** Simplified cluster analysis obtained from cross correlation of seismic attributes determined along Ja1 horizon. Four classes were distinguished on a cross correlation image (a) consisting of RMS and instantaneous frequency attributes calculated from CRS stacked section. These classes were plotted back on geometry backgorund (b) to perform a structural differentiation. Corresponding histograms of RMS amplitude (b) and instantaneous frequency (d) show the distribution of classes among the relevant variables of the attributes.

exploitation as the sandstone rocks of the Lower Jurassic found in Kompina-2 well shows its favorable reservoir parameters. The higher flow rate recorded in the borehole and its relationship to the seismic properties that were imaged by low value of frequency attributes may suggest high saturation of surrounding rocks due to damping effect at higher frequencies. Moreover, the higher saturation may suggest the presence of sinkholes located NE from the borehole and visible in the form of rounded anomalies The low RMS values and close location of Class 3 cluster in the vicinity of faults are

interpreted here as the effect of fracture porosity produced by tectonic activities (Lohr *et al.*, 2008) that affected the hanging wall east of the main fault line.

This fact makes the Class 3 cluster the most promising exploitation compartment (depicted by red grid) for future drilling using the geothermal doublet technology. Similar observations concerning geothermal exploitation and further productivity parameters determination within the same compartment were discussed by Cacace *et al.* (2013) and Cherubini *et al.* (2013a). Although the assumed higher values of fracture porosity in the surrounded rocks of the fault system hanging wall represents a promising geothermal reservoir model, nevertheless more advance modeling studies that can determine the permeability of faults system itself are necessary to construct fully operational hydrogeological model (Cherubini *et al.*, 2013b) and verify its production parameters (Blöcher *et al.*, 2009).

## 6.3 Outlook

The presented thesis shown the improvement of seismic trace attributes with the CRS stacking method. The CRS stack method implies the careful selection of stacking apertures, both in midpoint and offset direction in order to provide accurate ZO approximation of the reflection response. Based on that improved ZO stacking section/volume the seismic trace attribute analysis provides more detailed and valuable information that can be transferred to the geological domain and used in reservoir rock modeling. Although the method has proved its usability in geothermal exploration, however, further research and application of the CRS method coupled with the seismic trace attribute analysis could be carried out.

The research extension could be addressed in the multivariate form, creating space for a wider field of development. In the first step, the seismic section/volume, may be improved by the use of different approaches in order to obtain final CRS counterpart. In the original form, the CRS stack method (Mann *et al.*, 1999; Müller, 2007)) is based on single parameter search techniques. Although, it represents a pragmatic solution, more advanced techniques appeared that allow to solve global non-linear minimization problem and derive the CRS kinematic attributes with higher accuracy (Bonomi *et al.*, 2009; Garabito *et al.*, 2012). Recent implementations of the simultaneous parameters optimization for FPGA architecture may increase the speedup of calculation by a factor of 200 (Marchetti *et al.*, 2010) that allows to not only shorten the processing time but also to test more scenarios what is especially important on 3D datasets.

Other acquisition layouts that meet the budget criteria of geothermal projects could also be tested in order to ensure the appropriate balance between obtained data quality and incurred expenses. The geometry of the 3D layout (Bujakowski *et al.*, 2010) presented in this thesis was rather homogeneous thus testing other acquisition geometries and its dependencies on fold (Buness *et al.*, 2014) could also be a task for future developments. In addition to the modification of the CRS processing, the application of other methods such as NIP-wave tomography (Duveneck, 2004) could supplement the geothermal exploration campaign as the velocity estimation within the reservoir may provide additional information for the hydrogeological modeling. Moreover, the application of CRS diffraction imaging (Dell, 2012; Dell & Gajewski, 2011) could improve significantly the structural image of the subsurface.

Another possible extension is the involvement of further seismic attributes. Nowadays, the attribute oriented processing includes more sophisticated solutions, where

multiattribute and 3D attributes dominate (Farzadi, 2006). High imaging capabilities of the CRS stack results can also be used in conjunction with texture attributes (Yenugu *et al.*, 2010), an also coherence and spectral decomposition may be applied in order to better visualize lithological variations, thus simulate flow pathways for geothermal media. An interesting solution of using clustering of seismic attributes was presented by (Hustoft *et al.*, 2007) to indicate relationships between lithology and fluid flow. Is worth to mention high potential of the self organizing map (SOM) technique, used for pattern recognition within geothermal environment based on continuous wavefield records (Bauer *et al.*, 2012; Köhler *et al.*, 2010). This methodology can contains more seismic attributes than those presented in this thesis.

Beside the conjunction of the CRS method with the signal attribute analysis, which provided a sufficient platform for the structural and horizon interpretation, there are other geophysical methods which can be with the seismic results in order to establish an optimal geothermal exploration program. Some initial steps of such an application were performed with electromagnetic methods (Bujakowski *et al.*, 2010; Muñoz *et al.*, 2010b), stress field analysis (Reiter *et al.*, 2013) or geological modeling (Weides *et al.*, 2013) providing closer insight into geothermal environments.

# References


Al-Chalabi, M. (1973). Series approximation in velocity and traveltime computations. *Geophysical Prospecting*, **21**, 783–795.

Albarello, D., Mantovani, E., Babbucci, D. & Tamburelli, C. (1995). Africa-Eurasia kinematics: main constraints and uncertainties. *Tectonophysics*, **243**, 25–36.

Árnason, K., Eysteinsson, H. & Hersir, G. (2010). Joint 1D inversion of TEM and MT data and 3D inversion of MT data in the Hengill area, SW Iceland. *Geothermics*, **39**, 13–34.

Arthaud, F. & Matte, P. (1977). Late Paleozoic strike-slip faulting in southern Europe and northern Africa: Result of a right-lateral shear zone between the Appalachians and the Urals. *Geological Society of America Bulletin*, **88**, 1305–1320.

Bachu, S. (1993). Basement heat flow in the Western Canada Sedimentary Basin. *Tectonophysics*, **222**, 119–133.

Bachu, S. & Bennion, B. (2008). Effects of in-situ conditions on relative permeability characteristics of CO2-brine systems. *Environmental Geology*, **54**, 1707–1722.

Bahorich, M. & Farmer, S. (1995). 3-D seismic discontinuity for faults and stratigraphic features; the coherence cube. *The Leading Edge*, **14**, 1053–1058.

Bally, A.W., Gordy, P.L. & Stewart, G.A. (1966). Structure, seismic data, and orogenic evolution of southern Canadian Rocky Mountains. *Bulletin of Canadian Petroleum Geology*, **14**, 337–381.

Barbier, E. (1997). Nature and technology of geothermal energy: A review. *Renewable and Sustainable Energy Reviews*, **1**, 1–69.

Barbier, E. (2002). Geothermal energy technology and current status: An overview. *Renewable and Sustainable Energy Reviews*, **6**, 3–65.

## REFERENCES


Barnes, A. (2001). Seismic attributes in your facies. *CSEG Recorder*, **26**, 41–47.

Barnes, A. (2007). Redundant and useless seismic attributes. *Geophysics*, **72**, 33–38.

Barnes, A.E. (1991). Instantaneous frequency and amplitude at the envelope peak of a constant-phase wavelet. *Geophysics*, **56**, 1058–1060.

Barry, K.M., Cavers, D.A. & Kneale, C.W. (1975). Recommended standards for digital tape formats. *Geophysics*, **40**, 344–352.

Batini, F. & Nicolich, R. (1985). P and S reflection seismic profiling and well logging in the Travale geothermal field. *Geothermics*, **14**, 731–747.

Bauer, K., Schulze, A., Weber, M. & Moeck, I. (2006). Combining refraction seismic tomography and analysis of wide-angle reflections in geothermal exploration. In *AGU Fall Meeting Abstracts*.

Bauer, K., Moeck, I., Norden, B., Schulze, A., Weber, M. & Wirth, H. (2010). Tomographic P wave velocity and vertical velocity gradient structure across the geothermal site Groß Schönebeck (NE German Basin): Relationship to lithology, salt tectonics, and thermal regime. *Journal of Geophysical Research*, **115**, B08312.

Bauer, K., Muñoz, G. & Moeck, I. (2012). Pattern recognition and lithological interpretation of collocated seismic and magnetotelluric models using self-organizing maps. *Geophysical Journal International*, **189**, 984–998.

Bayer, U., Grad, M., Pharaoh, T., Thybo, H., Guterch, A., Banka, D., Lamarche, J., Lassen, A., Lewerenz, B., Scheck, M. & Marotta, A.M. (2002). The southern margin of the East European Craton: new results from seismic sounding and potential fields between the North Sea and Poland. *Tectonophysics*, **360**, 301–314.

Baykulov, M. & Gajewski, D. (2009). Prestack seismic data enhancement with partial common-reflection-surface (CRS) stack. *Geophysics*, **74**, 49–58.

Baykulov, M., Brink, H.J., Gajewski, D. & Yoon, M.K. (2009). Revisiting the structural setting of the Glueckstadt Graben salt stock family, North German Basin. *Tectonophysics*, **470**, 162–172.

Berkovitch, A., Belfer, I. & Landa, E. (2008). Multifocusing as a method of improving subsurface imaging. *The Leading Edge*, **27**, 250–256.

Berryman, J., Berge, P. & Bonner, B. (2000). Transformation of seismic velocity data to extract porosity and saturation values for rocks. *Journal of the Acoustical Society of America*, **107**, 3018–3027.

Bertrand, E., Caldwell, T., Hill, G., Wallin, E., Bennie, S., Cozens, N., Onacha, S., Ryan, G., Walter, C., Zaino, A. & Wameyo, P. (2012). Magnetotelluric imaging of upper-crustal convection plumes beneath the Taupo Volcanic Zone, New Zealand. *Geophysical Research Letters*, **39**, L02304.

Blöcher, G., Zimmermann, G. & Milsch, H. (2009). Impact of poroelastic response of sandstones on geothermal power production. *Pure and Applied Geophysics*, **166**, 1107–1123.

Boelsen, T. & Mann, J. (2005). 2D CO CRS Stack for OBS and VSP data and arbitrary top-surface topography. In *67th EAGE Conference and Exhibition*, European Association of Exploration Geophysicists.

Bojarski, L. & Sadurski, A. (2000). Deep connate groundwater of the Polish Lowlands. *Geological Review*, **48**, 587–595.

Bojarski, L., Płochniewski, Z. & Stachowiak, J. (1979). Mineral and thermal waters of the Warsaw Marginal Basin. *Geological Quarterly*, **23**, 435–446.

Bonomi, E., Cristini, A., Theis, D. & Marchetti, P. (2009). 3D CRS analysis: a data-driven optimization for the simultaneous estimate of the eight parameters. In *Proceedings of 79th Annual Meeting and International Exposition of the Society of Exploration Geophysics*, SEG.

Borowska, L. (2006). Report on the 2D seismic survey (reprocessing and reinterpretation) at the Kompina Site, Skierniewice-Łowicz area. Tech. rep., Mineral and Energy Economy Research Institute of the Polish Academy of Sciences, Krakow, Poland.

Brogi, A. (2004). Seismic reflection and borehole logs as tools for tectonic and stratigraphical investigations: New geological data for the Tuscan Nappe exposed in the northeastern Mt. Amiata area (Northern Apennines, Italy). *Bollettino della Societa Geologica Italiana*, **123**, 189–199.

Brogi, A., Lazzarotto, A., Liotta, D. & Ranalli, G. (2003). Extensional shear zones as imaged by reflection seismic lines: The Lardello geothermal field (central Italy). *Tectonophysics*, **363**, 127–139.

Bruhn, D., Manzella, A., Vuataz, F., Faulds, J., Moeck, I. & Erbas, K. (2010). Exploration methods. In E. Huenges, ed., *Geothermal Energy Systems: Exploration, Development, and Utilization*, 37–112, Wiley-VCH Verlag GmbH & Co. KGaA, Weinheim.

Buchholtz, H. (1972). A note on signal distortion due to dynamic (NMO) corrections. *Geophysical Prospecting*, **20**, 395–402.

## REFERENCES


Bujakowski, W. (2003). *Termiczna charakterystyka górotworu w rejonie wysadów solnych*. Wydawnictwo IGSMiE PAN, Kraków.

Bujakowski, W., Barbacki, A., Czerwińska, B., Pajak, L., Pussak, M., Stefaniuk, M. & Trześniowski, Z. (2010). Integrated seismic and magnetotelluric exploration of the Skierniewice, Poland, geothermal test site. *Geothermics*, **39**, 78–93.

Buness, H.A., von Hartmann, H., Rumpel, H.M., Krawczyk, C.M. & Schulz, R. (2014). Fault imaging in sparsely sampled 3D seismic data using common-reflection-surface processing and attribute analysis - a study in the Upper Rhine Graben. *Geophysical Prospecting*, **62**, 443–452.

Buntebarth, G. (1984). *Geothermics: An introduction*. Springer, Berlin.

Burliga, S. (1996). Implications for early basin dynamics of the Mid-Polish Trough from deformational structures within salt deposits in central Poland. *Geological Quarterly*, **40**, 185–202.

Cacace, M., Blöcher, G., Watanabe, N., Möck, I., Börsing, N., Scheck-Wenderoth, M., Kolditz, O. & Huenges, E. (2013). Modelling of fractured carbonate reservoirs: outline of a novel technique via a case study from the Molasse Basin, southern Bavaria, Germany. *Environmental Earth Sciences*, **70**, 3585–3602.

Cagniard, L. (1953). Basic theory of the magnetotelluric method of geophysical prospecting. *Geophysics*, **18**, 605–645.

Cameron, A. & Smith, G. (1991). Coals of Canada: Distribution and compositional characteristics. *International Journal of Coal Geology*, **19**, 9–20.

Casini, M., Ciuffi, S., Fiordelisi, A., Mazzotti, A. & Stucchi, E. (2010). Results of a 3D seismic survey at the Travale (Italy) test site. *Geothermics*, **39**, 4–12.

Castle, R. (1994). A theory of normal moveout. *Geophysics*, **59**, 983–999.

Chapman, D.S. & Rybach, L. (1985). Heat flow anomalies and their interpretation. *Journal of Geodynamics*, **4**, 3–37.

Charléty, J., Cuenot, N., Dorbath, C. & Dorbath, L. (2006). Tomographic study of the seismic velocity at the Soultz-sous-Forêts EGS/HDR site. *Geothermics*, **35**, 532–543.

Chen, Q. & Sidney, S. (1997). Seismic attribute technology for reservoir forecasting and monitoring. *The Leading Edge*, **16**, 445–448.

Chen, S., Huang, X. & Zhang, H. (2014). Fracture estimation using attenuation attributes – a case study. In *76th EAGE Conference and Exhibition 2014*, European Association of Exploration Geophysicists.

Chernyak, V. & Gritsenko, S. (1979). Interpretation of the effective common-depth-point parameters for a three-dimensional system of homogeneous layers with curvilinear boundaries. *Geologiya i Geofizika*, **20**, 112–120.

Cherubini, Y., Cacace, M., Blöcher, G. & Scheck-Wenderoth, M. (2013a). Impact of single inclined faults on the fluid flow and heat transport: results from 3-D finite element simulations. *Environmental Earth Sciences*, **70**, 3603–3618.

Cherubini, Y., Cacace, M., Scheck-Wenderoth, M., Möck, I. & Lewerenz, B. (2013b). Controls on the deep thermal field: implications from 3-D numerical simulations for the geothermal research site Großschönebeck. *Environmental Earth Sciences*, **70**, 3619–3642.

Chopra, S. & Marfurt, K.J. (2005). Seismic attributes - A historical perspective. *Geophysics*, **70**, 3–28.

Chopra, S. & Marfurt, K.J. (2007). *Seismic attributes for prospect identification and reservoir characterization*. Society of Exploration Geophysicists, Tulsa, OK.

Chopra, S. & Marfurt, K.J. (2008). Emerging and future trends in seismic attributes. *The Leading Edge*, **27**, 298–318.

Chopra, S. & Marfurt, K.J. (2009). Detecting stratigraphic features via cross-plotting of seismic discontinuity attributes and their volume visualization. *The Leading Edge*, **28**, 1422–1426.

Chopra, S. & Marfurt, K.J. (2011). Interesting pursuits in seismic curvature attribute analysis. *CSEG Recorder*, **36**, 40–51.

Christensen, N.I. & Mooney, W.D. (1995). Seismic velocity structure and composition of the continental crust: A global view. *Journal of Geophysical Research: Solid Earth*, **100**, 9761–9788.

Cianciara, K. (1975). Opracowanie badań sejsmicznych z rejonu Skierniewice-Sochaczew. Tech. rep., Geofizyka Kraków Sp. z o.o., Kraków, Poland.

Cianciara, K. & Piech, K. (1977). Opracowanie badań sejsmicznych z rejonu Brzeziny-Łowicz-Skierniewice. Tech. rep., Geofizyka Kraków Sp. z o.o., Kraków, Poland.

## REFERENCES


Corsi, R. (1986). Scaling and corrosion in geothermal equipment: problems and preventive measures. *Geothermics*, **15**, 839–856.

Criaud, A. & Fouillac, C. (1989). Sulfide scaling in low enthalpy geothermal environments: A survey. *Geothermics*, **18**, 73–81.

Cuenot, N., Charléty, J., Dorbath, L. & Haessler, H. (2006). Faulting mechanisms and stress regime at the european HDR site of Soultz-sous-Forêts, France. *Geothermics*, **35**, 561–575.

Cumming, W. & Bruhn, D. (2010). Preface. *Geothermics*, **39**, 1–3, The European I-GET Project: Integrated Geophysical Exploration Technologies for Deep Geothermal Reservoirs.

Dadlez, R. (2003). Mesozoic thickness pattern in the Mid-Polish Trough. *Geological Quarterly*, **47**, 223–240.

Dadlez, R., Narkiewicz, M., Stephenson, R., Visser, M. & van Wees, J.D. (1995). Tectonic evolution of the Mid-Polish Trough: modelling implications and significance for central European geology. *Tectonophysics*, **252**, 179–195.

Dadlez, R., Marek, S. & Pokorski, J. (1998). *Palaeogeographical atlas of the epicontinental Permian and Mesozoic in Poland*. Państwowy Instytut Geologiczny, Warszawa.

Danis, C., O'Neill, C., Lackie, M., Twigg, L. & Danis, A. (2011). Deep 3D structure of the Sydney basin using gravity modelling. *Australian Journal of Earth Sciences*, **58**, 517–542.

Davidson, J. & Elsner, W. (2005). Alberta's ultimate potential for conventional natural gas. Tech. rep., Alberta Energy and Utilities Board (EUB) and National Energy Board, Alberta, Canada.

De Matteis, R., Vanorio, T., Zollo, A., Ciuffi, S., Fiordelisi, A. & Spinelli, E. (2008). Three-dimensional tomography and rock properties of the Larderello-Travale geothermal area, Italy. *Physics of the Earth and Planetary Interiors*, **168**, 37–48.

Dell, S. (2012). *Seismic processing and imaging with diffractions*. Ph.D. thesis, University of Hamburg.

Dell, S. & Gajewski, D. (2011). Common-reflection-surface-based workflow for diffraction imaging. *Geophysics*, **76**, 187–195.

Deregowski, S. (1986). What is DMO? *First break*, **4**, 535–545.

Dietrich, J. (1999). Seismic stratigraphy and structure of the Lower Paleozoic, Central Alberta Lithoprobe Transect. *Bulletin of Canadian Petroleum Geology*, **47**, 362–374.

Dümmong, S., Meier, K., Hübscher, C. & Gajewski, D. (2007). Velocity model building: A comparison between prestack stereotomography and NIP-wave tomography. In *SEG Technical Program Expanded Abstracts 2007*, vol. 26, 3034–3038, SEG.

Duncan, P. & Eisner, L. (2010). Reservoir characterization using surface microseismic monitoring. *Geophysics*, **75**, 139–146.

Duveneck, E. (2004). 3D tomographic velocity model estimation with kinematic wavefield attributes. *Geophysical Prospecting*, **52**, 535–545.

Eaton, D.W., Milkereit, B., Ross, G.M., Kanasewich, F.R., Geis, W., Edwards, D.J., Kelsch, L. & Varsek, J. (1995). Lithoprobe abasin-scale seismic profiling in centreal Alberta: influence of basement on the sedimentary cover. *Bulletin of Canadian Petroleum Geology*, **43**, 65–77.

Eaton, D.W., Ross, G.M. & Hope, J. (1999). The rise and fall of a Cratonic Arch: A regional seismic perspective on the Peace River Arch, Alberta. *Bulletin of Canadian Petroleum Geology*, **47**, 346–361.

Echols, J., Benoit, D., Ohren, M., Oppliger, G. & Van Gundy, T. (2011). Integration of a 3D-3C reflection seismic survey over a known geothermal resource: Soda Lake, Churchill County, Nevada. *Geothermal Resources Council Transactions*, **35**, 1633–1641.

Edwards, D. & Brown, R. (1999). Understanding the influence of Precambrian crystalline basement on Upper Devonian carbonates in central Alberta from a geophysical perspective. *Bulletin of Canadian Petroleum Geology*, **47**, 412–438.

Eisenberg-Klein, G., Pruessmann, J., Gierse, G. & Trappe, H. (2008). Noise reduction in 2D and 3D seismic imaging by the CRS method. *The Leading Edge*, **27**, 258–265.

Farzadi, P. (2006). Seismic facies analysis based on 3D multi-attribute volume classification, Dariyan Formation, SE Persian Gulf. *Journal of Petroleum Geology*, **29**, 159–173.

Foulger, G. (1982). Geothermal exploration and reservoir monitoring using earthquakes and the passive seismic method. *Geothermics*, **11**, 259–268.

Gallup, D. (1998). Aluminum silicate scale formation and inhibitor (2): Scale solubilities and laboratory and field inhibition tests. *Geothermics*, **27**, 485–501.

## REFERENCES


Garabito, G., Stoffa, P.L., Lucena, L.S. & Cruz, J.C. (2012). Part I - CRS stack: Global optimization of the 2D CRS-attributes. *Journal of Applied Geophysics*, **85**, 92–101.

Garg, S., Pritchett, J., Wannamaker, P. & Combs, J. (2007). Characterization of geothermal reservoirs with electrical surveys: Beowawe geothermal field. *Geothermics*, **36**, 487–517.

Gasperikova, E., Newman, G., Feucht, D. & Arnason, K. (2011). 3D MT characterization of two geothermal fields in Iceland. *Geothermal Resources Council Transactions*, **35**, 1667–1671.

Geiermann, J. & Schill, E. (2010). 2-D magnetotellurics at the geothermal site at Soultz-sous-Forêts: Resistivity distribution to about 3000 m depth. *Comptes Rendus - Geoscience*, **342**, 587–599.

Gelchinsky, B. (1988). The Common Reflecting Element (CRE) method (non-uniform asymmetric multifold system). *Exploration Geophysics*, **19**, 71–75.

Gelchinsky, B., Berkovitch, A. & Keydar, S. (1999). Multifocusing homeomorphic imaging: Part 1. Basic concepts and formulas. *Journal of Applied Geophysics*, **42**, 229–242.

Górecki, W., ed. (1995). *Atlas of geothermal energy resources in the Polish Lowlands. 1. Mesozoic formations. 2. Palaeozoic formations.*. Geosynoptics Society GEOS, Kraków.

Górecki, W., ed. (2006). *Atlas of geothermal resources of Mesosoic formations in the Polish Lowlands*. AGH University of Science and Technology, Kraków.

Górecki, W., Kozdra, T., Kuźniak, T., Myśko, A. & Strzetelski, W. (2003). Geothermal-energy resources in the Polish Lowlands and the possibility of their industrial utilization. *Applied Energy*, **74**, 53–64.

Gosk, E. (1982). Geothermal resources assessment. In V. Cermák & R. Haenel, eds., *Geothermics and geothermal energy*, 257–263, Schweitzerbartsche Verlagsbuchhandlung, Stuttgart.

Grabowska, T. & Bojdys, G. (2001). The border of the East-European Craton in south-eastern Poland based on gravity and magnetic data. *Terra Nova*, **13**, 92–98.

Grabowska, T., Bojdys, G. & Dolnicki, J. (1998). Three-dimensional density model of the Earth's crust and the upper mantle for the area of Poland. *Journal of Geodynamics*, **25**, 5–34.

Grad, M., Keller, G., Thybo, H. & Guterch, A. (2002). Lower lithospheric structure beneath the Trans-European Suture Zone from POLONAISE'97 seismic profiles. *Tectonophysics*, **360**, 153–168.

Guterch, A. & Grad, M. (2006). Lithospheric structure of the TESZ in Poland based on modern seismic experiments. *Geological Quarterly*, **50**, 23–32.

Guterch, A., Grad, M., Materzok, R. & Perchuć, E. (1986). Deep structure of the Earth's crust in the contact zone of the Palaeozoic and Precambrian Platforms in Poland (Tornquist-Teisseyre zone). *Tectonophysics*, **128**, 251–279.

Haites, T.B. (1960). Transcurrent faults in Western Canada. *Alberta Society of Petroleum Geologists Journal*, **8**, 33–77.

Hale, D. (1984). Dipmoveout by Fourier transform. *Geophysics*, **49**, 741–757.

Hammond, A.L. (1974). Bright Spot: Better seismological indicators of gas and oil. *Science*, **185**, 515–517.

Hardage, B. (2000). *Vertical Seismic Profiling: Principles*. Pergamon, New York, 3rd edn.

Häring, M.O., Schanz, U., Ladner, F. & Dyer, B.C. (2008). Characterisation of the Basel 1 enhanced geothermal system. *Geothermics*, **37**, 469–495.

Heilmann, Z., Mann, J. & Koglin, I. (2006). CRS-stack-based seismic imaging considering top-surface topography. *Geophysical Prospecting*, **54**, 681–695.

Hein, F.J. & Nowlan, G.S. (1998). Regional sedimentology, conodont biostratigraphy and correlation of Middle Cambrian-Lower Ordovician (?) strata of the 'Finnegan' and Deadwood formations, Alberta subsurface, Western Canada Sedimentary Basin. *Bulletin of Canadian Petroleum Geology*, **46**, 166–188.

Henrys, S. & Hochstein, M. (1990). Geophysical structure of the Broadlandsohaaki geothermal field (New Zealand). *Geothermics*, **19**, 129–150.

Hirowatari, K. (1996). Scale prevention method by brine acidification with biochemical reactors. *Geothermics*, **25**, 259–270.

Höcht, G. (2002). *Traveltime approximations for 2D and 3D media and kinematic wavefield attributes*. Ph.D. thesis, University of Karlsruhe.

Höcht, G., de Bazelaire, E., Majer, P. & Hubral, P. (1999). Seismics and optics: hyperbolae and curvatures. *Journal of Applied Geophysics*, **42**, 261–281.

Hope, J., Eaton, D.W. & Ross, G.M. (1999). Lithoprobe seismic transect of the Alberta Basin: Compliation and overview. *Bulletin of Canadian petroleum geology*, **47**, 331–345.

Houseman, G. & McKenzie, D.P. (1982). Numerical experiments on the onset of convective instability in the Earth's mantle. *Geophysical Journal of the Royal Astronomical Society*, **68**, 133–164.

Hubral, P. (1983). Computing true amplitude reflections in a laterally inhomogeneous Earth. *Geophysics*, **48**, 1051–1062.

Hubral, P. & Krey, T. (1980). *Interval Velocities from Seismic Reflection Time Measurements*. Society of Exploration Geophysicists, Tulusa, OK.

Huenges, E. (2010). *Geothermal Energy Systems: Exploration, Development, and Utilization*. Wiley-VCH Verlag GmbH & Co. KGaA, Weinheim.

Hustoft, S., Mienert, J., Bünz, S. & Nouzé, H. (2007). High-resolution 3D-seismic data indicate focussed fluid migration pathways above polygonal fault systems of the mid-Norwegian margin. *Marine Geology*, **245**, 89–106.

Jäger, C. (2005). *Minimum-aperture Kirchhoff migration with CRS stack attributes*. Ph.D. thesis, University of Karlsruhe, Berlin.

Jäger, R., Mann, J., Höcht, G. & Hubral, P. (2001). Common-reflection-surface stack: Image and attributes. *Geophysics*, **66**, 97–109.

Jaupart, C. (1981). *On the mechanisms of heat loss beneath continents and oceans*. Ph.D. thesis, Massachusetts Institute of Technology, Cambridge, MA.

Jaupart, C. & Parsons, B. (1985). Convective instabilities in a variable viscosity fluid cooled from above. *Physics of the Earth and Planetary Interiors*, **39**, 14–32.

Jones, F.W., Lam, H.L. & Majorowicz, J.A. (1985). Temperature distributions at the Paleozoic and Precambrian surfaces and their implications for geothermal and energy recovery in Alberta. *Canadian Journal of Earth Sciences*, **22**, 1774–1780.

Jousset, P., Haberland, C., Bauer, K. & Arnason, K. (2011). Hengill geothermal volcanic complex (Iceland) characterized by integrated geophysical observations. *Geothermics*, **40**, 1–24.

Karnkowski, P.H. (1999). Origin and evolution of the Polish Rotliegend Basin. *Polish Geological Institute Special Papers*, **3**, 1–93.

Kent, D.M. (1994). Paleogeographic evolution of the cratonic platform - Cambrian to Triassic. In: Geological atlas of the Western Canada Sedimentary Basin G.D. Mossop and I. Shetsen (comps.). Online; accessed 9-November-2012.

Kepińska, B. (2003). Current geothermal activities and prospects in Poland – an overview. *Geothermics*, **32**, 397–407.

Kepińska, B. (2010). Geothermal energy country update report from Poland, 2005-2009. In *Proceedings of the World Geothermal Congress, Bali (Indonesia)*.

Klein, P., Richard, L. & James, H. (2008). 3D curvature attributes: a new approach for seismic interpretation. *First Break*, **26**, 105–111.

Koglin, I. (2005). *Estimation of residual static time shifts by means of the CRS-based residual static correction approach*. Ph.D. thesis, University of Karlsruhe, Berlin.

Köhler, A., Ohrnberger, M. & Scherbaum, F. (2010). Unsupervised pattern recognition in continuous seismic wavefield records using Self-Organizing Maps. *Geophysical Journal International*, **182**, 1619–1630.

Krey, T. (1952). The significance of diffraction in the investigation of faults. *Geophysics*, **17**, 843–858.

Krzywiec, P. (2004). Triassic evolution of the Kłodawa salt structure: basement-controlled salt tectonics within the Mid-Polish Trough (Central Poland). *Geological Quarterly*, **48**, 123–134.

Kunz, B.F.J. (1960). Diffraction problems in fault interpretation. *Geophysical Prospecting*, **8**, 381–388.

Kutek, J. & Głazek, J. (1972). The Holy Cross area, Central Poland, in the Alpine cycle. *Acta Geologica Polonica*, **4**.

Lamarche, G. (1992). Seismic reflection survey in the geothermal field of the Rotorua Caldera, New Zealand. *Geothermics*, **21**, 109–119.

Landa, E., Shtivelman, V. & Gelchinsky, B. (1987). A method for detection of diffracted waves on common-offset sections. *Geophysical Prospecting*, **35**, 359–373.

Landa, E., Gurevich, B., Keydar, S. & Trachtman, P. (1999). Application of multifocusing method for subsurface imaging. *Journal of Applied Geophysics*, **42**, 283–300.

Landa, E., Keydar, S. & Jan Moser, T. (2010). Multifocusing revisited-inhomogeneous media and curved interfaces. *Geophysical Prospecting*, **58**, 925–938.

Lees, J. (2004). Scattering from a fault interface in the Coso geothermal field. *Journal of Volcanology and Geothermal Research*, **130**, 61–75.

Legarth, B. (2008). Drilling deep wells - Key challenges and cost implications. *VDI Berichte*, **2026**, 45–53.

Legaz, A., Revil, A., Roux, P., Vandemeulebrouck, J., Gouédard, P., Hurst, T. & Bolève, A. (2009). Self-potential and passive seismic monitoring of hydrothermal activity: A case study at Iodine Pool, Waimangu geothermal valley, New Zealand. *Journal of Volcanology and Geothermal Research*, **179**, 11–18.

Leszczyński, K. (2012). The internal geometry and lithofacies pattern of the Upper Cretaceous-Danian sequence in the Polish Lowlands. *Geological Quarterly*, **56**, 363–386.

Levin, S.A. (1989). Surface-consistent deconvolution. *Geophysics*, **54**, 1123–1133.

Liberty, L. (1998). Seismic reflection imaging of a geothermal aquifer in an urban setting. *Geophysics*, **63**, 1285–1294.

Lohr, T., Krawczyk, C.M., Tanner, D.C., Samiee, R., Endres, H., Thierer, P.O., Oncken, O., Trappe, H., Bachmann, R. & Kukla, P.A. (2008). Prediction of subseismic faults and fractures: Integration of three-dimensional seismic data, three-dimensional retrodeformation, and well data on an example of deformation around an inverted fault. *AAPG Bulletin*, **92**, 473–485.

Lüschen, E., Dussel, M., Thomas, R. & Schulz, R. (2011). 3D seismic survey for geothermal exploration at Unterhaching, Munich, Germany. *First Break*, **29**, 45–54.

Lüschen, E., Wolfgramm, M., Fritzer, T., Dussel, M., Thomas, R. & Schulz, R. (2014). 3D seismic survey explores geothermal targets for reservoir characterization at Unterhaching, Munich, Germany. *Geothermics*, **50**, 167–179.

Majer, E. (2003). 3-D seismic methods for geothermal reservoir exploration and assessment – summary. Tech. Rep. LBNL-49881, Lawrence Berkeley National Laboratory, Berkeley, CA.

Majorowicz, J., Čermak, V., Šafanda, J., Krzywiec, P., Wróblewska, M., Guterch, A. & Grad, M. (2003). Heat flow models across the Trans-European Suture Zone in the area of the POLONAISE97 seismic experiment. *Physics and Chemistry of the Earth, Parts A/B/C*, **28**, 375–391.

Majorowicz, J.A. (2004). Thermal lithosphere across the Trans-European suture zone in Poland. *Geological Quarterly*, **48**, 1–14.

Majorowicz, J.A. & Jessop, A.M. (1981). Regional heat flow patterns in the Western Canada Sedimentary Basin. *Tectonophysics*, **74**, 209–238.

Majorowicz, J.A., Jones, F., Lam, H. & Jessop, A.M. (1985). Regional variations of heat flow differences with depth in Alberta, Canada. *Geophysical Journal of The Royal Astronomical Society*, **81**, 479–487.

Mamczur, S. & Radecki, S. (1998). Złoże ropy naftowej BMB (Barnówko-Mostno-Buszewo). *Nafta-Gaz*, **54**, 105–109.

Mann, J. (2002). *Extensions and Applications of the Common-Reflection-Surface Stack Method*. Ph.D. thesis, University of Karlsruhe.

Mann, J., Jäger, R., Müller, T., Höcht, G. & Hubral, P. (1999). Common-reflection-surface stack – a real data example. *Journal of Applied Geophysics*, **42**, 301–318.

Mann, J., Duveneck, E., Hertweck, T. & Jäger, C. (2003). A seismic reflection imaging workflow based on the Common-Reflection-Surface stack. *Journal of Seismic Exploration*, **12**, 283–295.

Marchetti, P., Oriato, D., Pell, O., Cristini, A. & Theis, D. (2010). Fast 3D ZO CRS stack - An FPGA implementation for an optimization based on simultaneous estimate of eight parameters. In *72nd European Association of Geoscientists and Engineers Conference and Exhibition*, 2915–2519.

Marek, S. (1988a). Paleothickness, lithofacies and paleotectonics of the epicontinental Lower Cretaceous in Poland. *Geological Quarterly*, **32**, 157–174.

Marek, S. (1988b). Paleothickness, lithofacies and paleotectonics of the epicontinental Permian and Mesozoic in Poland. *Geological Quarterly*, **32**, 1–14.

Marek, S. & Pajchlowa, M. (1997). *The epicontinental Permian and Mesozoic in Poland*. Prace Państwowego Instytutu Geologicznego, Państwowy Instytut Geologiczny, Warszawa.

Marek, S. & Znosko, J. (1972). Tectonics of the Kujawy region. *Geological Quarterly*, **16**, 1–18.

Marfurt, K.J., Sudhaker, V., Gersztenkorn, A., Crawford, K.D. & Nissen, S.E. (1999). Coherency calculations in the presence of structural dip. *Geophysics*, **64**, 104–111.

Matsushima, J., Okubo, Y., Rokugawa, S., Yokota, T., Tanaka, K., Tsuchiya, T. & Narita, N. (2003). Seismic reflector imaging by prestack time migration in the Kakkonda geothermal field, Japan. *Geothermics*, **32**, 79–99.

May, B. & Straley, D. (1979). Higher-order moveout spectra. *Geophysics*, **44**, 1193–1207.

Mayne, W.H. (1962). Common reflection point horizontal data stacking techniques. *Geophysics*, **27**, 927–938.

Mayr, S., Stanchits, S., Langenbruch, C., Dresen, G. & Shapiro, S. (2011). Acoustic emission induced by pore-pressure changes in sandstone samples. *Geophysics*, **76**, 21–32.

Michelena, R.J., Godbey, K.S. & Rodrigues, P.E. (2011). Facies probabilities from multidimensional crossplots of seismic attributes: Application to tight gas Mamm Creek Field, Piceance Basin, Colorado. *The Leading Edge*, **30**, 62–69.

Moeck, I., Hinz, N., Faulds, J., Bell, J., Kell-Hills, A. & Louie, J. (2010). 3D geological mapping as a new method in geothermal exploration: A case study from central Nevada. *Geothermal Resources Council Transactions*, **34**, 742–746.

Moeck, I.S. (2014). Catalog of geothermal play types based on geologic controls. *Renewable and Sustainable Energy Reviews*, **37**, 867–882.

Monger, J.W.H. & Price, R.A. (1979). Geodynamic evolution of the Canadian Cordillera – progress and problems. *Canadian Journal of Earth Sciences*, **16**, 770–791.

Mossop, G. & Shetsen, I. (1994). *Geological atlas of the Western Canada Sedimentary Basin*. Canadian Society of Petroleum Geologists and Alberta Research Council, online; accessed 9-November-2012.

Muksin, U., Bauer, K. & Haberland, C. (2013). Seismic Vp and Vp/Vs structure of the geothermal area around Tarutung (North Sumatra, Indonesia) derived from local earthquake tomography. *Journal of Volcanology and Geothermal Research*, **260**, 27–42.

Müller, N.A. (2007). *Determination of interval velocities by inversion of kinematic 3D wavefield attributes*. Ph.D. thesis, University of Karlsruhe.

Müller, T. (1999). *The Common Reflection Surface Stack Method – Seismic imaging without explicit knowledge of the velocity model*. Ph.D. thesis, University of Karlsruhe.

Muñoz, G., Bauer, K., Moeck, I., Schulze, A. & Ritter, O. (2010a). Exploring the Groß Schönebeck (Germany) geothermal site using a statistical joint interpretation of magnetotelluric and seismic tomography models. *Geothermics*, **39**, 35–45.

Muñoz, G., Ritter, O. & Moeck, I. (2010b). A target-oriented magnetotelluric inversion approach for characterizing the low enthalpy Groß Schönebeck geothermal reservoir. *Geophysical Journal International*, **183**, 1199–1215.

Nakagome, O., Uchida, T. & Horikoshi, T. (1998). Seismic reflection and VSP in the Kakkonda geothermal field, Japan: Fractured reservoir characterization. *Geothermics*, **27**, 535–552.

Nawrocki, J., Wagner, R. & Grabowski, J. (2013). The permian/triassic boundary in the Polish basin in the light of paleomagnetic data. *Geological Quarterly*, **37**.

Neidell, N. & Taner, M. (1971). Semblance and other coherency measures for multichannel data. *Geophysics*, **36**, 482–497.

Newman, G., Gasperikova, E., Hoversten, G. & Wannamaker, P. (2008). Three-dimensional magnetotelluric characterization of the Coso geothermal field. *Geothermics*, **37**, 369–399.

Niitsuma, H., Fehler, M., Jones, R., Wilson, S., Albright, J., Green, A., Baria, R., Hayashi, K., Kaieda, H., Tezuka, K., Jupe, A., Wallroth, T., Cornet, F., Asanuma, H., Moriya, H., Nagano, K., Phillips, W., Rutledge, J., House, L., Beauce, A., Alde, D. & Aster, R. (1999). Current status of seismic and borehole measurements for HDR/HWR development. *Geothermics*, **28**, 475–490.

Notfors, C. & Godfrey, R. (1987). Dip moveout in the frequency-wavenumber domain. *Geophysics*, **52**, 1718–1721.

Papiernik, B., Machowski, G., Słupczyński, K. & Semyrka, R. (2009). Geologiczny model rejonu akumulacji ropno-gazowej Lubiatów-Miedzychód-Grotów (LMG). *Geologia*, **35**, 175–182.

Pellerin, L., Johnston, J. & Hohmann, G. (1996). A numerical evaluation of electromagnetic methods in geothermal exploration. *Geophysics*, **61**, 121–130.

Pichon, X.L., Bergerat, F. & Roulet, M.J. (1988). Plate kinematics and tectonics leading to the Alpine belt formation: a new analysis. *Special paper - Geological Society of America*, **218**, 111–131.

Place, J., Diraison, M., Naville, C., Géraud, Y., Schaming, M. & Dezayes, C. (2010). Decoupling of deformation in the Upper Rhine Graben sediments. Seismic reflection and diffraction on 3-component Vertical Seismic Profiling (Soultz-sous-Forêts area). *Comptes Rendus - Geoscience*, **342**, 575–586.

Porter, J.W., Price, R.A. & McCrossan, R.G. (1982). The Western Canada Sedimentary Basin. *Philosophical Transactions of the Royal Society of London*, **305**, 169–182.

Price, R.A. & Mountjoy, E.W. (1970). Geologic structure of the Canadian Rocky Mountains between Bow and Athabasca Rivers - a progress report. In : Structure of the southern Canadian Cordillera, J. O. Wheeler, ed. *Geological Association of Canada Special Paper*, **6**, 7–25.

Pussak, M., Bauer, K., Stiller, M. & Bujakowski, W. (2014). Improved 3D seismic attribute mapping by CRS stacking instead of NMO stacking: Application to a geothermal reservoir in the Polish Basin. *Journal of Applied Geophysics*, **103**, 186–198.

Rabbel, W. & Lüschen, E. (1996). Shear wave anisotropy of laminated lower crust at the Urach geothermal anomaly. *Tectonophysics*, **264**, 219–233.

Reiter, K., Heidbach, O. & Moeck, I. (2013). Stress field modelling in the Alberta Basin, Canada. In *International Workshop on Geomechanics and Energy: The Ground as Energy Source and Storage*, Lausanne, Switzerland.

Represas, P., Monteiro Santos, F., Ribeiro, J., Ribeiro, J., Almeida, E., Gonalves, R., Moreira, M. & Mendes-Victor, L. (2013). Interpretation of gravity data to delineate structural features connected to low-temperature geothermal resources at Northeastern Portugal. *Journal of Applied Geophysics*, **92**, 30–38.

Resak, M., Narkiewicz, M. & Littke, R. (2008). New basin modelling results from the Polish part of the Central European Basin system: implications for the late Cretaceous-Early Paleogene structural inversion. *International Journal of Earth Sciences*, **97**, 955–972.

Rial, J.A., Elkibbi, M. & Yang, M. (2005). Shear-wave splitting as a tool for the characterization of geothermal fractured reservoirs: Lessons learned. *Geothermics*, **34**, 365–385.

Ronen, J. & Claerbout, J.F. (1985). Surface-consistent residual statics estimation by stack-power maximization. *Geophysics*, **50**, 2759–2767.

Ross, G.M. & Eaton, D.W. (1999). Basement reactivation in the Alberta Basin: Observational constraints and mechanical rationale. *Bulletin of Canadian petroleum geology*, **47**, 391–411.

Ross, G.M., Parrish, R.R., Villeneuve, M. & Bowring, S.A. (1991). Geophysics and geochronology of the crystalline basement of the Alberta Basin, western Canada. *Canadian Journal of Earthh Sciences*, **28**, 512–552.

Ross, G.M., Milkereit, B., Eaton, D., White, D., Kanasewich, E.R. & Burianyk, M.J.A. (1995). Paleoproterozoic collisional orogen beneath the western Canada sedimentary basin imaged by Lithoprobe crustal seismic-reflection data. *Geology*, **23**, 195–199.

Sanyal, S. (2007). Ensuring resource adequacy for a commercial geothermal project. *Geothermal Resources Council Transactions*, **31**, 93–97.

Sausse, J., Dezayes, C., Dorbath, L., Genter, A. & Place, J. (2010). 3D model of fracture zones at Soultz-sous-Forêts based on geological data, image logs, induced microseismicity and vertical seismic profiles. *Comptes Rendus - Geoscience*, **342**, 531–545.

Schleicher, J., Tygel, M. & Hubral, P. (1993). Parabolic and hyperbolic paraxial two-point traveltimes in 3D media. *Geophysical Prospecting*, **41**, 495–513.

SEG (1995). Shell processing support format for land 3-D surveys. *Geophysics*, **60**, 596–596.

Shah, P. (1973). Use of wavefront curvature to relate seismic data with subsurface parameters. *Geophysics*, **38**, 812–825.

Shapiro, S., Krüger, O., Dinske, C. & Langenbruch, C. (2011). Magnitudes of induced earthquakes and geometric scales of fluid-stimulated rock volumes. *Geophysics*, **76**, 55–63.

Sharpton, V.L., Grieve, R.A.F., Thomas, M.D. & Halpenny, J.F. (1987). Horizontal gravity gradient: An aid to the definition of crustal structure in North America. *Geophysical Research Letters*, **14**, 808–811.

Shoffner, J., Li, Y., Hinz, N., Sabin, A., Lazaro, M. & Alm, S. (2010). Understanding fault characteristics and sediment depth for geothermal exploration using 3D gravity inversion in Walker Valley, Nevada. *Geothermal Resources Council Transactions*, **34**, 586–589.

Sigfusson, T. (2012). Geothermal energy. In A. Sayigh, ed., *Comprehensive Renewable Energy*, Elsevier, Oxford.

Simmons, N., Forte, A. & Grand, S. (2006). Constraining mantle flow with seismic and geodynamic data: A joint approach. *Earth and Planetary Science Letters*, **246**, 109–124.

Simpson, F. & Bahr., K. (2005). *Practical Magnetotellurics*. Cambridge University Press, Cambridge.

Slind, O., Andrews, G., Murray, D., Norford, B., Paterson, D., Salas, C. & Tawadros, E. (1994). *Middle Cambrian to Lower Ordovician strata of the Western Canada Sedimentary Basin. In: Geological atlas of the Western Canada Sedimentary Basin G.D. Mossop and I. Shetsen (comps.)*. Canadian Society of Petroleum Geologists and Alberta Research Council, online; accessed 9-November-2012.

Sokolowski, J. (1993). Geothermal resources in Poland and possibility of their utilization in environmental protection. *Exploration Geology, Geosynoptics and Geothermal Energy*, **5-6**, 67–80.

Soma, N. & Niitsuma, H. (1997). Identification of structures within the deep geothermal reservoir of the Kakkonda field, Japan, by a reflection method using acoustic emission as a wave source. *Geothermics*, **26**, 43–64.

Spichak, V., Zakharova, O. & Rybin, A. (2011). Methodology of the indirect temperature estimation basing on magnetotelluric data: Northern Tien Shan case study. *Journal of Applied Geophysics*, **73**, 164–173.

Spinner, M. & Mann, J. (2005). True-amplitude CRS-based Kirchhoff time migration for AVO analysis. In *SEG Technical Program Expanded Abstracts 2005*.

Spinner, M.E.T. (2007). *CRS-based minimum-aperture Kirchhoff migration in the time domain*. Ph.D. thesis, University of Karlsruhe.

Stephenson, R.A., Narkiewicz, M., Dadlez, R., van Wees, J.D. & Andriessen, P. (2003). Tectonic subsidence modelling of the Polish Basin in the light of new data on crustal structure and magnitude of inversion. *Sedimentary Geology*, **156**, 59–70.

Stoakes, F. (1987). Evolution of the Upper Devonian of Western Canada. In G. Bloy & M. Charest, eds., *Principles and Concepts for Exploration and Exploitation of Reefs in the Western Canada Basin, Short Course Notes*, Canadian Society of Petroleum Geologists, Calgary.

Stoakes, F.A. (1980). Nature and control of shale basin fill and its effect on reef growth and termination; Upper Devonian Duvernay and Ireton formations of Alberta, Canada. *Bulletin of Canadian Petroleum Geology*, **28**, 345–410.

Stott, D. & Aitken, J. (1993). *Sedimentary Cover of the Craton in Canada*, vol. 5 of *Geology of North America*. Geological Survey of Canada, Toronto.

Stringham, G. (2012). Energy Developments in Canada's Oil Sands. In K.E. Percy, ed., *Alberta Oil Sands*, vol. 11, chap. 2, 19–34, Elsevier.

Sugama, T. & Gawlik, K. (2002). Anti-silica fouling coatings in geothermal environments. *Materials Letters*, **57**, 666–673.

Sugihara, M. & Ishido, T. (2008). Geothermal reservoir monitoring with a combination of absolute and relative gravimetry. *Geophysics*, **73**, 37–47.

Szewczyk, J. & Gientka, D. (2009). Terrestrial heat flow density in Poland – a new approach. *Geological Quarterly*, **53**, 125–125.

Szuflicki, M., Malon, A. & Tyńminski, M. (2013). *Bilans zasobów złóż kopalin w Polsce wg stanu na 31 XII 2012 r.*. Państwowy Instytut Geologiczny–Państwowy Instytut Badawczy, Warszawa, online; accessed 23-June-2013.

Tan, H., Yu, Q., Booker, J. & Wei, W. (2003). Three-dimensional rapid relaxation inversion for the magnetotelluric method. *Acta Geophysica Sinica*, **46**, 850–854.

Taner, M. (2001). Seismic attributes. *CSEG Recorder*, **26**.

Taner, M. & Koehler, F. (1969). Velocity spectra - digital computer derivation applications of velocity functions. *Geophysics*, **34**, 859–881.

Taner, M., Koehler, F. & Sheriff, R. (1979). Complex seismic trace analysis. *Geophysics*, **44**, 1041–1063.

Tang, C., Rial, J. & Lees, J. (2008). Seismic imaging of the geothermal field at Krafla, Iceland using shear-wave splitting. *Journal of Volcanology and Geothermal Research*, **176**, 315–324.

Tikhonov, A. (1950). On determining electrical characteristics of the deep layers of the Earth's crust. *Doklady*, **73**, 295–297.

Trappe, H., Coman, R., Gierse, G., Robinson, S., Owens, M. & Nielsen, E.M. (2005). Combining CRS technology and sparse 3D seismic surveys - a new approach to acquisition design. In *67th EAGE Conference & Exhibition*.

Turcotte, D.L. & Schubert, G. (2002). *Geodynamics*. Cambridge University Press.

Unruh, J., Monastero, F. & Pullammanappallil, S. (2008). The nascent Coso metamorphic core complex, east-central California: Brittle upper plate structure revealed by reflection seismic data. *International Geology Review*, **50**, 245–269.

van Wees, J.D., Stephenson, R.A., Ziegler, P.A., Bayer, U., McCann, T., Dadlez, R., Gaupp, R., Narkiewicz, M., Bitzer, F. & Scheck, M. (2000). On the origin of the Southern Permian Basin, Central Europe. *Marine and Petroleum Geology*, **17**, 43–59.

Vanorio, T., De Matteis, R., Zollo, A., Batini, F., Fiordelisi, A. & Ciulli, B. (2004). The deep structure of the Larderello-Travale geothermal field from 3D microearthquake traveltime tomography. *Geophysical Research Letters*, **31**, L07613.

## REFERENCES


Verm, R. & Hilterman, F. (1995). Lithology, color-coded seismic sections; the calibration of AVO crossplotting to rock properties. *The Leading Edge*, **14**, 847–853.

Villeneuve, M., Ross, G.M., Theriault, R.J., Miles, M., Parrish, R.R. & Broome, J. (1993). Tectonic subdivisions and U-Pb geochronology of the crystalline basement of the Alberta Basin, Western Canada. *Bulletin – Geological Survey of Canada*, **447**.

Volpi, G., Manzella, A. & Fiordelisi, A. (2003). Investigation of geothermal structures by magnetotellurics (MT): An example from the Mt. Amiata area, Italy. *Geothermics*, **32**, 131–145.

von Hartmann, H., Buness, H., Krawczyk, C. & Schulz, R. (2012). 3-D seismic analysis of a carbonate platform in the Molasse Basin - reef distribution and internal separation with seismic attributes. *Tectonophysics*, **572-573**, 16–25.

Ward, P. (1972). Microearthquakes: Prospecting tool and possible hazard in the development of geothermal resources. *Geothermics*, **1**, 3–12.

Waters, K. & Kemper, M. (2014). Find the rocks and the fluids will follow – AVO as a tool for lithology classification. *Interpretation*, **2**, 77–91.

Watts, N. (1987). Carbonate sedimentology and depositional history of the Nisku Formation (within the Western Canada Sedimentary Basin) in south central Alberta. In F. Krause & O. Burrows, eds., *Devonian lithofacies and reservoir styles in Alberta*, 286, Canadian Society of Petroleum Geologists, Toronto.

Weber, M., Zetsche, F., Ryberg, T., Schulze, A., Spangenberg, E. & Huenges, E. (2005). Seismic detection limits of small, deep, man-made reflectors: A test at a geothermal site in northern Germany. *Bulletin of the Seismological Society of America*, **95**, 1567–1573.

Weides, S., Moeck, I., Majorowicz, J., Palombi, D. & Grobe, M. (2013). Geothermal exploration of Paleozoic formations in Central Alberta. *Canadian Journal of Earth Sciences*, **50**, 519–534.

White, R. (1991). Properties of instantaneous seismic attributes. *The Leading Edge*, **10**, 26–32.

Winchester, J., Pharaoh, T. & Verniers, J. (2002). *Palaeozoic amalgamation of Central Europe*. Special publication, Geological Society, London.

Wuestefeld, A., Al-Harrasi, O., Verdon, J., Wookey, J. & Kendall, J. (2010). A strategy for automated analysis of passive microseismic data to image seismic anisotropy and fracture characteristics. *Geophysical Prospecting*, **58**, 755–773.

Yahara, T. & Tokita, H. (2010). Sustainability of the Hatchobaru geothermal field, Japan. *Geothermics*, **39**, 382–390.

Yenugu, M., Marfurt, K. & Matson, S. (2010). Seismic texture analysis for reservoir prediction and characterization. *The Leading Edge*, **29**, 1116–1121.

Yilmaz, Ö. (2001). *Seismic Data Analysis*. Investigations in geophysics, Society Of Exploration Geophysicists, Tulsa, OK.

Yilmaz, Ö. & Clearbout, J. (1980). Prestack partial migration. *Geophysics*, **45**, 1753–1779.

Yuen, D. & Fleitout, L. (1984). Stability of the oceanic lithosphere with variable viscosity: an initial-value approach. *Physics of the Earth and Planetary Interiors*, **334**, 173–185.

Zeng, H. (1991). Geologic significance of anomalous instantaneous frequency. *Geophysics*, **75**, 23–30.

Zhang, B., Wang, T. & Marfurt, K.J. (2011). Revisiting NMO stretch and velocity analysis. In *SEG Technical Program Expanded Abstracts 2011*, chap. 795, 4040–4044.

Zhang, Q. & McMechan, G. (2011). Direct vector-field method to obtain angle-domain common-image gathers from isotropic acoustic and elastic reverse time migration. *Geophysics*, **76**, 135–149.

Zhang, Y. (2003). *Common-Reflection-Surface Stack and the Handling of Top Surface Topography*. Logos Verlag, Berlin.

Ziegler, P. (1990). *Geological Atlas of Western and Central Europe*. Shell International Petroleum Maatschoppij B.V, Den Haag, 2nd edn.

# Acknowledgements

I am grateful to Dr. Klaus Bauer for his patient supervision of this work and for giving me a lot of freedom in planning of my research. His door was always open for me when questions about my current working topics occurred. He gave me the opportunity to produce this work and allowed me to participate in many geophysical events and projects.

I am also grateful to Prof. Dr. Michael Weber for the co-supervision of my thesis and also for giving me a possibility to extend my theoretical background, although my project was more practically oriented.

I would also like to say thank you to Dr. Wieslaw Bujakowski from MEERI PAS for introducing me the wonderful idea of geothermal energy and other reneweables. I also enjoyed the times at MEERI PAS.

I am grateful to Manfred Stiller for deepen my knowledge of seismic data processing and for proof reading of my texts. I am as well grateful to Dr. Mikhail Baykulov, Dr. Sergius Dell for the CRS driven discussions and good advices in the preliminary processing.

I am also grateful to Christian Feld for his companionship and for sharing an office during my stay at the GFZ. I also like to say thank you to Christof Lendl and Mathias Wanjek for solving most of my computer issues. My thanks also goes to Anke Lerch, who always helped me with administration issues and organized social activities.

I also like to thank Prof. Dr. Dirk Gajewski, Prof. Dr. Thomas Bohlen for accepting my request for being part of the disputation council.

I gratefully acknowledge the Mineral and Energy Economy Research Institute of the Polish Academy of Sciences (MEERI PAS) and Natural Resources Canada (NRCan) for access to datasets which represent the basis for the work I presented in this thesis. I gratefully acknowledge the Helmholtz-Zentrum Potsdam - Deutsches GeoForschungsZentrum and the Helmholtz

Alberta Initiative (HAI) for funding of my position and the conference attendance. I also acknowledge the Wave Inversion Technology (WIT) consortium for the code provided by the consortium represents the basis for the work presented in this thesis.

Last but not least, I would like to thank my family and especially my sons, you were boys still smiling at me every time I was a doubt.

# Declaration

I herewith declare that I have produced this paper without the prohibited assistance of third parties and without making use of aids other than those specified; notions taken over directly or indirectly from other sources have been identified as such. This paper has not previously been presented in identical or similar form to any other German or foreign examination board.

Potsdam, May 2014